Experimental and Numerical Validation of Three-Dimensional Tsunami Wave Pressures and Forces on an Elevated Structure

Cassidy Jane Gills

A thesis
submitted in partial fulfillment of the
requirements for the degree of

Master of Science in Civil Engineering

University of Washington

2018

Reading Committee:

Michael Motley, Chair

Marc Eberhard, Chair

Pedro Arduino

Program Authorized to Offer Degree:
Department of Civil and Environmental Engineering

University of Washington

Abstract

Experimental and Numerical Validation of Three-Dimensional Tsunami Wave Pressures and Forces on an Elevated Structure

Cassidy Jane Gills

Co-Chairs of the Supervisory Committee:
Professor Michael Motley
Department of Civil and Environmental Engineering

Professor Marc Eberhard
Department of Civil and Environmental Engineering

The implementation of evacuation structures was proven to be an effective means of tsunami evacuation during the 2011 tsunami in Japan. However, there is currently a lack of experimental and numerical work concerning the three-dimensional interaction of tsunamis and elevated structures. To date experimental work has focused on structures on grade while the numerical work has primary focused on model validation by way of simplistic force comparison. The focus of this work is to examine three-dimensional tsunami-like wave pressure distributions on an elevated structure, and numerically validate the localized pressure results and corresponding loading time histories. This was accomplished through large scale experimental tests and an accompanying numerical model in which an elevated structure was inundated by a tsunami-like wave at two different states: an unbroken wave and a broken bore. Results showed trends in the unbroken and broken wave pressure distributions. The unbroken wave resembled a linear distribution, comparable to hydrostatic loading at points of inundation. The impulsive broken turbulent bore was best represented by a quadratic curve. Using a computational fluid dynamics software package, the experimental tests were validated numerically. A locally validated numerical model will allow future researchers the flexibility to perform studies not feasible by experimentation.

TABLE OF CONTENTS

LIST OF FIGURES

LIST OF TABLES

ACKNOWLEDGMENTS

I would first like to thank my advisors, Professor Michael Motley and Professor Marc Eberhard for their support and guidance throughout my masters degree. I am extremely grateful for the opportunity to work and learn from them. They have set an example of excellence as researches and mentors. Each provided me with their unique expertise that encouraged my growth as an engineer. I am grateful for their consideration of my time and professional goals throughout my masters degree. I would additionally like to thank Professor Pedro Arduino for serving on my reading committee.

I would like to express my gratitude to the entire collaborative research team from the University of Washington and Oregon State University that conducted the experimental work presented in this thesis. I would like to thank Andrew Winter and Shariq Alam, who lead the experimental tests at OSU as well as Professor Andre Barbosa. As I did not participate in the experimental work, their efforts and willingness to answer all questions was greatly appreciated. I would like to express my additional gratitude to Andrew Winter. His guidance and assistance throughout my research project was invaluable.

Furthermore, I would like to thank the Valle Scholarship and Scandinavian Exchange Program for giving me to opportunity to participate in graduate studies and research at the University of Washington. I greatly appreciate the experience and education it has provided while at UW.

Additionally, I would like to thank Xinsheng (Shawn) Qin and Molly Greer. Shawn's knowledge of high performance computing and OpenFOAM contributed to the timeliness of this thesis. I would like to thank my friend and office-mate Molly, my graduate school experience would not have been the same without her. As well as all of my fellow graduate

students and friends, Sara Ibarra, Sarah Wichman, and Ingimar Johannsson. Their friendships enriched my time in graduate school. Finally I would like to thank my family for their love and support throughout this process.

Chapter 1

INTRODUCTION

1.1 Background on Tsunamis

The Cascadia Subduction Zone (CSZ) stretches 1,000 km, from Vancouver Island to Cape Mendocino, California. Every 400 to 600 years, the CSZ produces a Magnitude 8 or greater earthquake [32]. A subduction zone occurs at the convergence of two tectonic plates; for the CSZ these are the Juan de Fuca Plate and the North American Plate. This collision causes the Juan de Fuca Plate (the subducting plate) to slide beneath the North American Plate. The Juan De Fuca plate is forced to descend down into earth's mantle creating friction between the plates. As the Juan de Fuca plate moves, the overriding North American plate is forced to distort and buckle due to the resisting friction. This will continue until the frictional force between the plates is not adequate to restrain the North American Plate.

The energy between the plates will be released in the form of a fault rupture as the North American plate returns to its undistorted position. This plate movement would suddenly thrust the North American plate forward lowering its inland area. This sudden movement would displace a large amount of water, resulting in a tsunami [20].

The recent magnitude 7.9 earthquakes in the Gulf of Alaska resulted in tsunami warnings along the Alaskan and Canadian Pacific coasts. Tsunami watches were also issued for Washington, Oregon, and California. Although this earthquake was not caused by a subduction zone, and only small tsunami surges inundated part of the Alaskan coast, these warnings are a clear reminder that the west coast of North America is susceptible to a CSZ fault rupture. This could result in intense ground shaking followed by a tsunami that would impact coastal buildings and infrastructure in Washington, Oregon, and northern California, as well as Alaska.

Recent examples of the devastating effects of tsunamis include Japan in 2011, Chile in 2010 and the Indian Ocean Tsunami in 2004. These three events caused an enormous amount of loss. The Indian Ocean earthquake and accompanying tsunami results is over 300,000 lives lost and an estimated 1.5 million homeless. The magnitude 9.3 earthquake affected 19 countries and causing death and destruction in 12. The tsunami triggered by the 2011 Tohoku Earthquake in Japan results in more than 400,000 buildings damaged or destroyed [12].

1.2 Elevated Structures

Tsunamis are short-term, high-risk events for which, unlike an earthquake, forewarning is sometimes possible. The time delay of the earthquake and tsunami inundation allows coastal communities time to evacuate in some cases. Tsunami evacuation is preferably by means of horizontal relocation in which the affected populations evacuate to high ground outside of the inundation zone. However many low-lying or near source coastal communities will not likely have adequate time to get to high ground. In this case vertical evacuation to upper levels of structures is the best alternative. To prevent loss of life, tsunami evacuation structures should be utilized in areas of risk. The tsunami warning period allows a unique and concentrated design approach to coastal vertical evacuation infrastructure. Therefore, the highest priority for tsunami-resistant design should be evacuation structures. The Federal Emergency Management Agency (FEMA) recommended that parking structures, community or commercial facilities, and schools be considered to serve as tsunami vertical evacuation refuge structures [10]. For example, the first tsunami evacuation structure along the Washington coast is part of a new elementary school in Westport, Washigton [13].

During the 2011 tsunami in Japan, many structures that were designed for vertical evacuation failed because of unanticipated inundation heights and runup [31]. Following this tsunami, field investigations were conducted to better understand the infrastructure failures throughout the affected regions in Japan. It was found that all overturned buildings had an open area of less than 10% below inundation level [4].

FEMA defines an elevated building in at-risk tsunami regions as a structure that has its lowest elevated floor raised above ground level by foundation walls, shear walls, posts, piers, pilings, or columns such as the office building seen in Figure 1.1. However solid perimeter walls are not an accepted means of elevation in these areas [1]. As illustrated by the field evidence of overturned buildings following the 2011 Tsunami in Japan, elevated structures are an ideal choice for tsunami vertical evacuation refuge structures to prevent structural overturning.

Figure 1.1: Elevated Office Building in Concepcion, Chile [33]

With the increased development in regions around the highly seismic Pacific rim, it is becoming more important to prepare at-risk communities for a tsunami event [8]. As shown in the 2011 Japan Tsunami, the proper design of tsunami evacuation structures, such as elevated structures, is critical to prevent loss of life. The complexity and high variability associated with tsunami waves make the structural loading challenging to understand. Therefore it is critical to understand the three-dimensional interaction between an elevated structure and various type of tsunami waves.

1.3 Importance of Numerical Validation

Computational fluid dynamics simulation is a powerful tool for studying the interaction of tsunami-like waves and infrastructure. However, due to the current state of available experimental data, validation of such models is often a difficult task. The majority current experimental data is in terms of force measurements which are highly influence by variables such as structural flexibility or the presence and properties of experimental support structures. Numerical models are concerned with the fluid quantities such as pressure and velocity, and matching such influenced experimental results can be difficult. To date, experimental tests have been unable to accurately correlate experimentally measured pressure and forces. As numerical models extrapolate such forces from pressure surfaces, there is often a reluctance to accept numerical prediction from validated models.

The quality of results obtained from numerical simulation in computational fluid dynamics (CFD) are dependent upon many variables such as the mesh quality and the numerical scheme. Therefore, model validation is a prerequisite to any numerical parametric study as it is a means of assessing the accuracy of the numerical assumptions.

1.4 Previous Experimental Work

Many experiments have been conducted to study the interactions between tsunami-generated waves and coastal infrastructure. Different structures, such as vertical walls, structural models in a variety of shapes on grade, and elevated structures have been studied. For instance, Roberton et al. [27] and Hamzah et al. [14] conducted experimental test programs relating to the interaction of a tsunami bore with a vertical wall. Hamzah et al. also conducted a numerical validation of their experiment. Hamzah et al. found a uniform pressure distribution on the wall; however the studies conducted by Roberton et al., showed linear vertical pressure distributions.

A variety of structural shapes and configurations have been subjected to tsunami loading. Shafiei et al. [30] studied the interaction of a tsunami bore on a square prism structure with

varying orientation with respect to the incoming flow. The vertical distribution of pressure on the front wall was measured throughout the experiment. It was found that as orientation angle increased the pressure on the structure decreased. Also at 0 degree orientation, the initial bore impact vertical pressure distribution resembled that for a parabolic distribution and which quickly became linear following the impulsive impact of the wave.

Chinnarasri et al [7] experimentally investigated the variance of bore impact on a variety of structural shapes. Square, rectangular and octagonal structures were tested. A bi-linear pressure distribution was proposed, where the pressure is uniform up to a critical height at which point it become linear.

Tomiczek et al. [34] conducted an experiment on non-impulsive waves on an elevated structure. Their tests also found a bi-linear pressure distribution. However the experimental wave was not categorized as a tsunami bore. Nine pressure gauges were used to instrument the front face of the the test structure used in this experiment. The force estimated from integrated pressures exceeded load cell results.

Palermo et al. [24] experimentally tested the vertical pressure distributions on the upstream face of a square structure. Three phases of tsunami-bore interactions were observed: impulse, run-up and quasi-steady hydrodynamic. It was concluded that the pressure distributions on the front face can be well approximated with a hydrostatic assumption. However, Nouri et al, [22] conducted experiments on cylindrical and square structures. They concluded that tsunami waves created nonlinear pressure distribution which were greater than the hydrostatic distribution.

The experimental work presented illustrates the high variability associated with tsunami-structure interaction. It is important to note that no previous experimental work in the literature was found that instrumented the three-dimensional pressure field.

1.5 Previous Numerical Work

Numerical modeling of fluid-structure interactions allows the opportunity for a deeper understanding of flow fields over a surface that would be unrealistic to instrument. However,

fluid structure interaction is highly non-linear and variance in the turbulence near boundaries and fluid surfaces can be difficult to model accurately model. With recent computational advancements, modeling complex non-linearity is possible. Many numerical packages are available to simulate fluid-structure interaction. However, numerical model validation has had good success with using OpenFOAM in both two-dimensional and three-dimensional models ([36], [19], [28], [16], [25], [26]).

Experimental tests investigating the tsunami forces on bridge superstructures were validated with both 2D and 3D OpenFOAM models [36], [19], [25]. Motley et al. [19] found that both two- and three-dimensional models did an adequate job predicting the total force on the bridge. However, the force was over estimated in both models with improvement shown in the three-dimensional model.

Qin et al. ([25], [26]) simulated tsunami inundation within a model scale construction environment. The three-dimension Reynolds Averaged Navier Stokes (RANS) OpenFOAM model demonstrated good agreement with the free surface elevation, velocity and moment flux of the experimental results. The same experiment was also validated with GeoClaw with a two-dimensional model based on the nonlinear shallow water equations (NSWE). Qin et al. (and others) have found that the RANS equations provide more accurate solutions to modeling tsunami-like waves due to transient and turbulent nature of the flows.

Jiang et al. numerically modeled an experiment that studies the interactions of tsunami waves and vertical seawalls using OpenFOAM [16]. The results of the validation showed agreement of the wave dynamics around the seawall including the free surface, velocity, and dynamic pressure.

Free standing structures with a variety of shapes were experimentally subjected to tsunami bores. These tests were then modeled and numerically validated by Sarjammee et al. ([28]). The results from the OpenFOAM model showed good agreement between the numerical model results and the experimental results for the base shear and total pressure. However, there is a discrepancy at the moment of initial impact of the tsunami bore of the pressure measurement.

It has been shown that previous numerical models have had success with modeling experiment through OpenFOAM. However, all previous numerical modeling validation has focused primarily on the tsunami wave characteristic or resultant forces. Validation at a localized level will allow researchers to begin to better understand the three-dimensional effects of tsunami loading. The focus of most numerical simulations and experimental tests have been on grade structures, which are not completely representative of coastal infrastructure.

1.6 Objectives

The primary focus of this work is to extend the understanding of tsunami structure interaction and to further validate numerical models by evaluating the three-dimensional pressure field on an elevated structure. This will be accomplished using the experimental results of a large scale experimental test program conducted at Oregon State University's (OSU) O.H. Hinsdale Wave Research Laboratory in which an elevated structure was subjected to a variety of tsunami-like wave conditions. Pressure distributions will then be validated through numerical modeling of the experimental tests using the software package OpenFOAM. Characterizing the imposed pressure distributions of a tsunami-like force on an elevated structure is a step to create tsunami resilient elevated infrastructure. After understanding the experimentally measured horizontal pressures and forces, the experimental pressures will be numerically validated. After illustrating pressure measurements are an acceptable means of model validation, this work hopes to encourage the collaboration between experimental and numerical work, so that model validation is achieved in the best way possible.

The organization of this thesis is as follows. A detailed description of the experimental test set up will be presented in Chapter 2, followed by experimental results and analysis in Chapters 3 and 4. Chapters 5 and 6 will discuss the numerical model description and results respectively. A concluding discussion is presented in Chapter 7

Chapter 2

EXPERIMENTAL PROGRAM

The experiential work was conducted by a collaborative team from the University of Washington and Oregon State University lead by Ph.D. students Andrew O. Winter and Mohamman Shafiqual Alam in the Large Wave Flume at Oregon State University's O.H. Hinsdale Wave Research Laboratory. This chapter describes the experimental setup, instrumentation and test conditions.

2.1 Experimental Set-Up

2.1.1 Testing Facility

The Large Wave Flume, shown in Figure, 2.1 is 104m (342 ft) long, 3.7m (12 ft) wide, and 4.6m (15 ft) in height. Waves are generated by a piston-type wavemaker on the upstream side of the flume. This wavemaker is capable of producing regular, irregular, and tsunami-like waves. Its maximum stroke is 4m (13.1 ft) at a speed of 4m/s (13.1 ft/s). The maximum water depth for a tsunami wave is 2m (6.5 ft). The flume has a movable and adjustable bathymetry allowing varying assemblies to change the wave propagation.

2.1.2 Large Wave Flume Configuration

For the experimental test program discussed here, the flume profile consisted of 6 sections. The first was a flat offshore section, 14.3m (46.9 ft) long, followed by the first of the adjustable concrete slabs: 3.66m (12.0 ft) in length and 0.15m off the flume floor. Two sloped sections followed. The first section, the steeper of the two, was 11.0m (36.1 ft) long with a slope of 1:12. The second sloped section was 14.6m (48.0 ft) with a slope of 1:24. A horizontal slab,

36.75m long, elevated at 1.75m followed the sloped slabs. The last section was a 1:12 sloped slab that was 7.52m long.

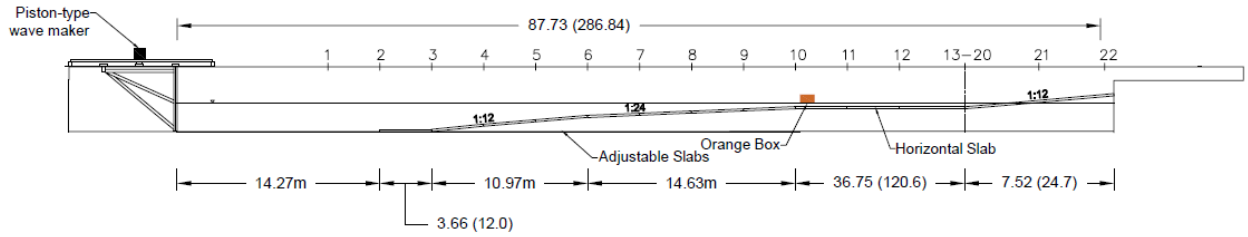

Figure 2.1: Large Wave Flume Configuration

2.1.3 Test Structure and Frame

The test specimen, shown in Figure 2.2, for this experimental program was a rectangular box made out of steel plates with internal square steel tubes. The test specimen was 1.01m wide and deep and 0.61m tall. It was placed 0.24m from the end of the 1:24 sloped slab.

(a) Front (b) Side (c) Back

Figure 2.2: Test Specimen [2]

Longitudinal and transverse frames, attached to the top of the test structure, were used to secure it in the Large Wave Flume. The frames were connected to another frame on the sides of the flume by threaded rods and longitudinal bracing. The details of the experimental set up are shown in Figure 2.3.

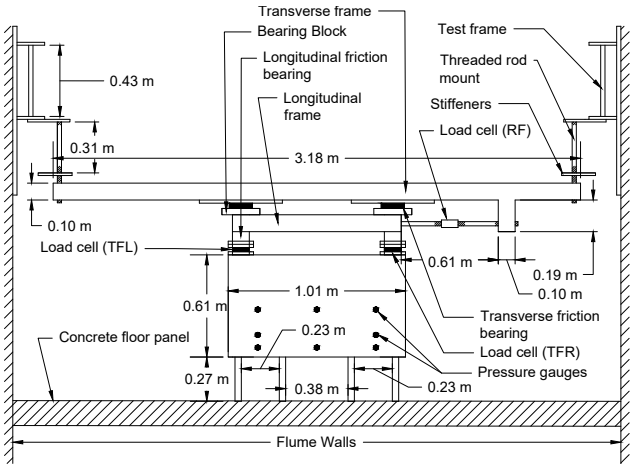

(a) Front View

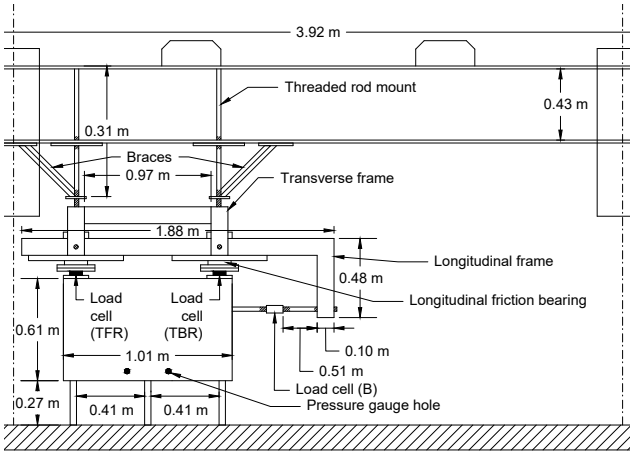

(b) Side View

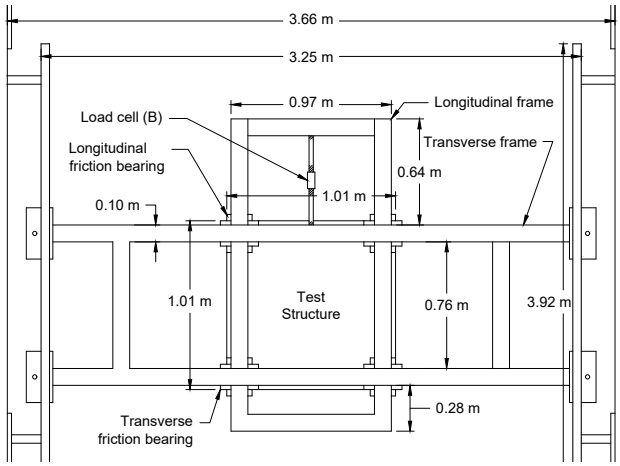

(c) Top View

Figure 2.3: Experimental Set Up [35]

Twelve steel columns, or legs, were attached to the bottom of the test specimen, to replicate the stilts commonly seen in elevated coastal infrastructure. However, these columns did not support the test specimen or come in contact with the bottom of the flume. The test frame, seen in Figure 2.4 , elevated the test specimen slightly off the flume floor, which left a small gap between the columns and the concrete slab.

Figure 2.4: Test Specimen and Frame [2]

Frictionless bearings were installed between the longitudinal and transverse frames to minimize the force resisted by the test frame.

2.1.4 Flume Coordinate System and Nomenclature

The flume's longitudinal direction (104m) defined the x axis, the y axis was defined as the flume's transverse direction (3.7m) and the z direction was taken as the vertical direction (4.6m). The flume coordinate system origin was located at the wavemaker paddle's mid stroke (x axis), at the transverse center line (y axis) and on the flume floor (z axis). This work will often reference the right and left side of the flume or of the test specimen. This is in reference to the transverse direction of the flume when facing downstream. The right side is the positive y axis direction and the left side is the negative y direction. The faces of

the test specimen will be referred to as the front (upstream face), back (downstream face), bottom (normal to flume floor), top (normal to atmosphere), right (normal to right flume wall), and left (normal to left flume wall).

2.2 Instrumentation

2.2.1 Wave Measurements

Wave gauges and velocimeters were installed throughout the Large Wave Flume to measure the wave propagation. The layout of the wave gauges in seen in Figure 2.5. Three wire resistance wave gauges were placed between the wavemaker and the test specimen to track the propagation of the wave. An additional wire resistance wave gauge was installed on the piston-type wave generator. To track the wave as it interacted with the test specimen, six ultrasonic wave gauges were installed. The six gauges surround the test specimen. Two typical wave instruments are shown in Figure 2.6.

The wave gauge naming convention is two or four letters followed by a number, excluding the wire resistance gauge on the wavemaker. The letters reference the type of instrument, wg for wire resistance wave gauge and uswg for ultrasonic wave gauge. The gauges were numbered from upstream to downstream and right to left ($+y$ to $-y$). The number restarts at the ultrasonic wave gauges. The wire resistance wave gauge on the wavemaker was named wmwg.

Seven Acoustic Doppler Velocimeters (ADV) were placed around the test specimen to measure the local velocity fluctuations as the wave interacted with the test structure. Similar to the wave gauges, the ADVs were numbered according to their position in the flume, from upstream to downstream and right to left as seen in Figure 2.7.

The last wave measurement device recorded the piston wavemaker displacement for each trial. This instrument was named wmdisp. The full wave measurement instrumentation locations are documented in Table 2.1.

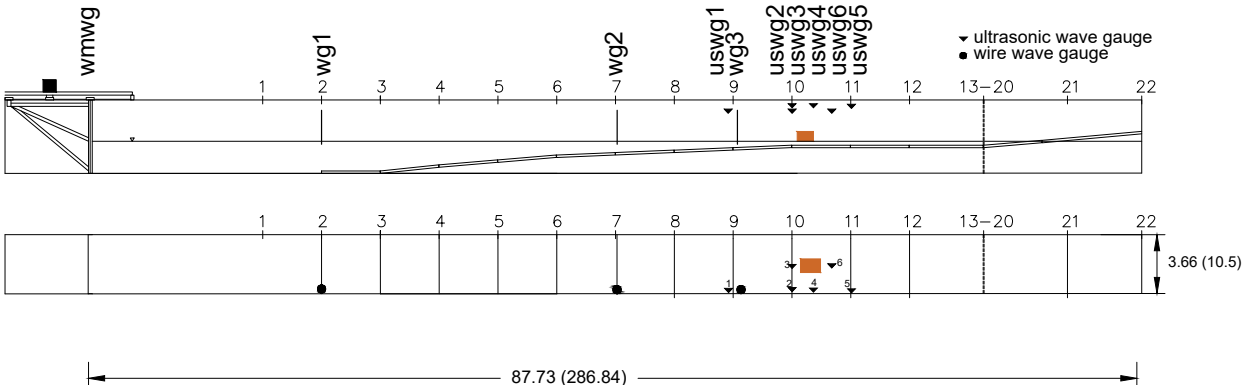

Figure 2.5: Elevation (top) and Plan (bottom) View of Wave Gauge Positions [2]

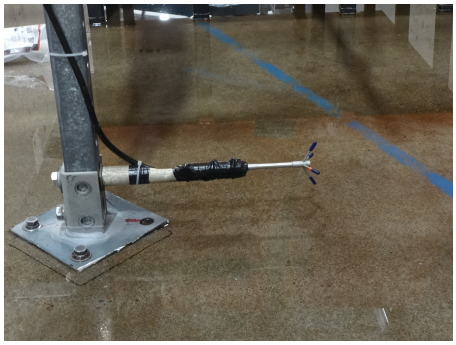

(a) Acoustic Doppler Velocimeter

(b) Ultrasonic Wave Gauge

Figure 2.6: Typical Wave Instrumentation [2]

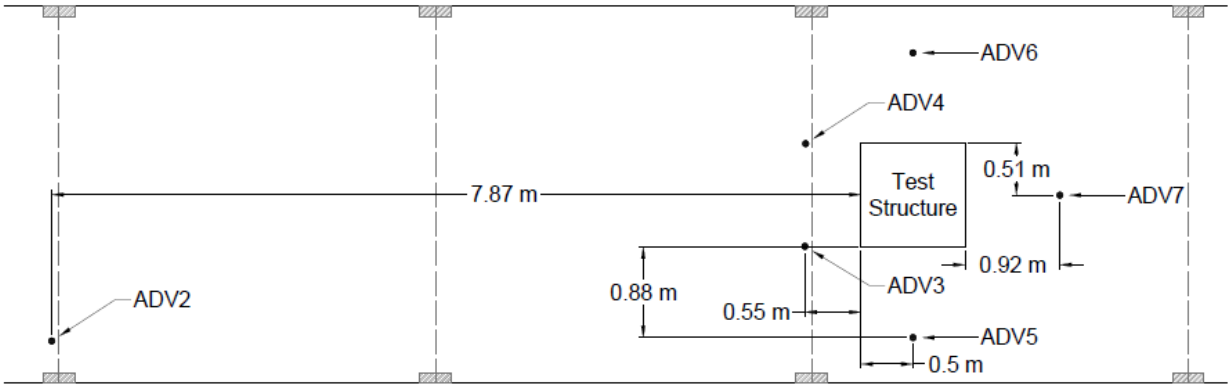

Figure 2.7: Plan View of Acoustic Doppler Velocimeter (ADV) Layout [35]

Table 2.1: Wave Instrumentation

Instrument Name	Instrument Description	x (m)	y (m)	z (m)
wmdisp	Wave Maker Displacement	-	0	-
wmwg	Resistance Wave Gauge	-	0	-
wg1	Resistance Wave Gauge	14.17	-1.39	-
wg2	Resistance Wave Gauge	32.44	-1.38	-
wg3	Resistance Wave Gauge	36.1	-1.37	-
uswg1	Ultrasonic Wave Gauge	39.7	-1.38	3.65
uswg2	Ultrasonic Wave Gauge	43.21	-1.38	3.35
uswg3	Ultrasonic Wave Gauge	43.21	0	3.32
uswg4	Ultrasonic Wave Gauge	44.29	-1.31	3.41
uswg5	Ultrasonic Wave Gauge	45.69	-1.38	3.31
uswg6	Ultrasonic Wave Gauge	45.68	0	3.37
adv1	Acoustic Doppler Velocimeters	13.97	-1.43	0.63
adv2	Acoustic Doppler Velocimeters	35.9	-1.42	1.54
adv3	Acoustic Doppler Velocimeters	43.21	-0.5	1.75
adv4	Acoustic Doppler Velocimeters	43.22	0.49	1.75
adv5	Acoustic Doppler Velocimeters	44.27	-1.39	1.76
adv6	Acoustic Doppler Velocimeters	44.26	1.38	1.76
adv7	Acoustic Doppler Velocimeters	45.69	0	1.82

2.2.2 Pressure Measurements

To measure the impact of the waves on the test specimen, pressure gauges and load cells were used in each experimental trial. The test specimen was instrumented with 14 pressure gauges for each trial placed in three configurations. A typical installation of a pressure gauge layout is shown in Figure 2.8. To record a detailed center line pressure distribution, pressure gauge Layout 1, shown in Figure 2.9, positioned all pressure gauges along the center line of the test specimen. This layout included 9 pressure gauges placed 4 cm apart on the front face of the box, 4 pressure gauges placed 25 cm apart on the bottom face and a gauge placed 2 cm from the bottom of the box on the back face.

Layout 2 focused the pressure gauges on the outside thirds of the test specimen. Shown

Figure 2.8: Typical Pressure Gauges Installation [2]

in Figure 2.10, Layout 2 had 9 pressure gauges placed in a 'U' pattern on the front face, two pressure gauges on the left and right faces and one pressure gauge on both the bottom and back. To record a three-dimensional pressure profile, Layout 3, shown in Figure 2.11, placed pressure gauges on the center line, outside thirds and left, right and bottom sides of the test specimen.

The pressure gauges were identified by their positions on the box. Each pressure gauge had a 1 to 3 character name. The first character denotes the face the pressure gauge was on: front face (F), right face (R), left face (L), back face (B), bottom face (X). The next character denotes the horizontal location (transverse for the bottom face) on the face in question: middle (M), right side (R) and left side (L). If there is no second character, there was only one gauge on that face. The third character references the vertical position (longitudinal for the bottom face) of the gauge, with the numbering increasing with vertical height (upstream to downstream for the bottom face). If two or more gauges on the same face have the same number, they were located at the same vertical (or longitudinal for the bottom face) location. If the gauge does not have a third character, there was one gauge in that horizontal location. Table 2.2 provides the coordinate positions of each pressure gauge.

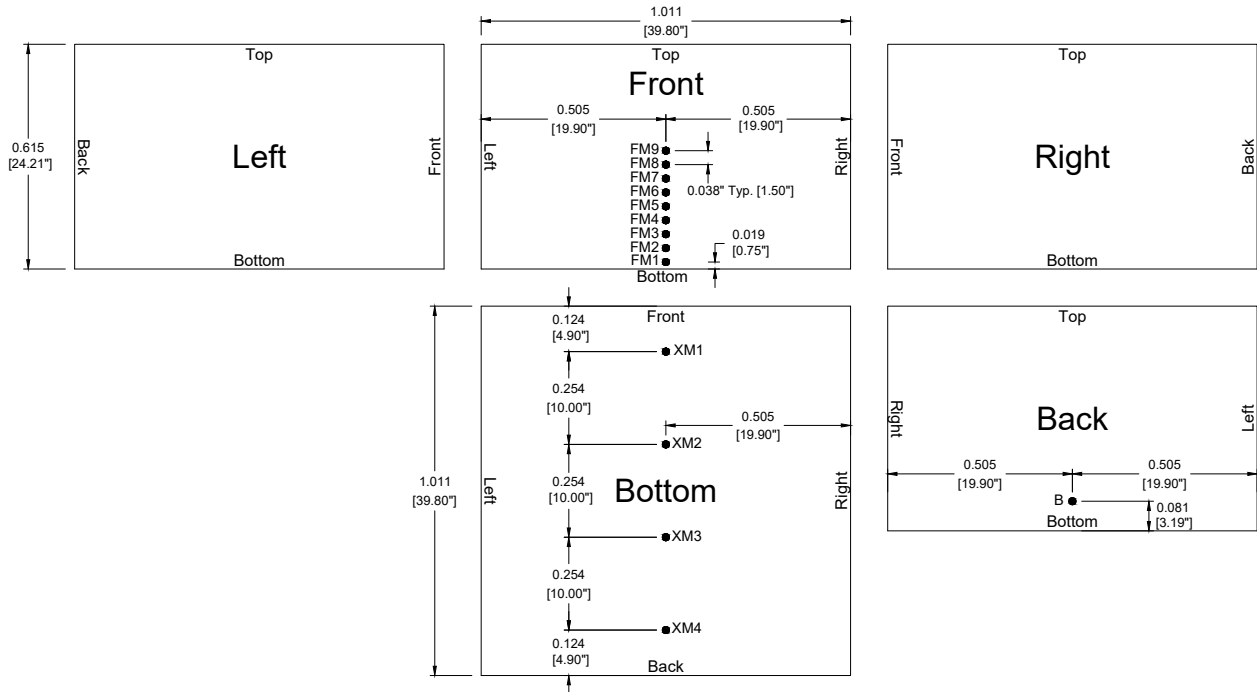

Figure 2.9: Pressure Gauge Layout 1 [35]

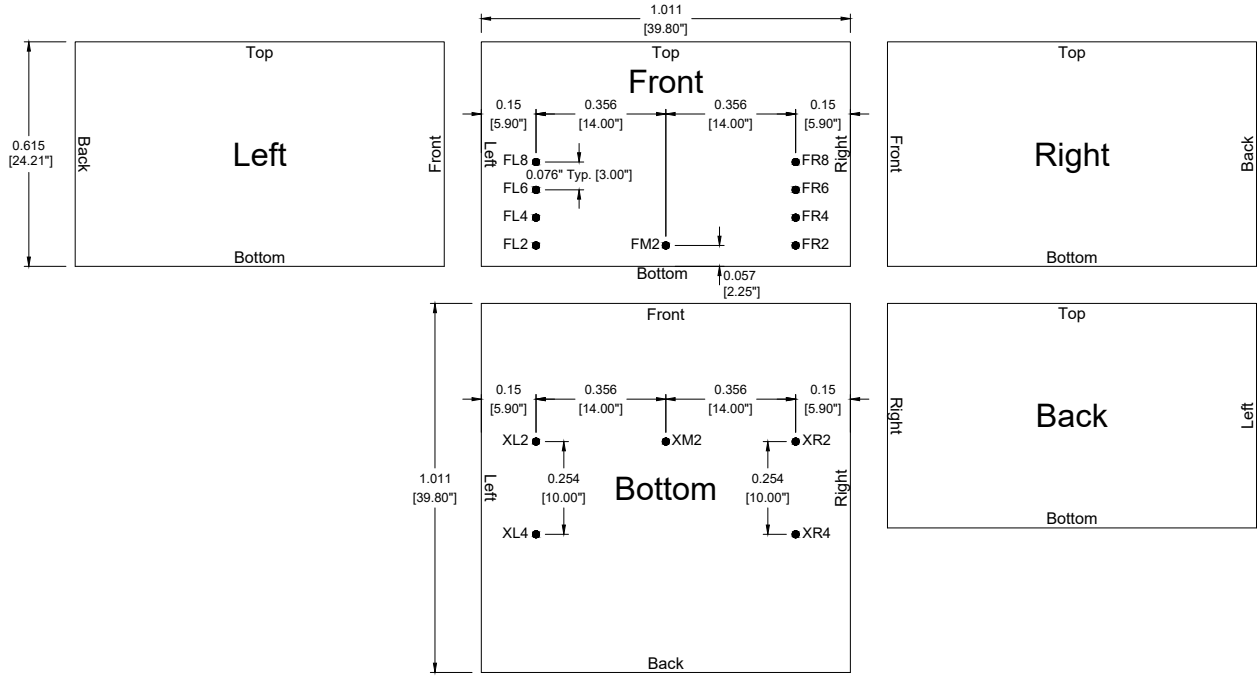

Figure 2.10: Pressure Gauge Layout 2 [35]

Table 2.2: Pressure Gauge Locations

Gauge Name	Test Specimen Face	x (m)	y (m)	z (m)	Layout 1	Layout 2	Layout 3
FL2	front	43.76	0.35	2.06		✓	✓
FL4	front	43.76	0.35	2.14		✓	✓
FL6	front	43.76	0.35	2.21		✓	
FL8	front	43.76	0.35	2.29		✓	✓
FM1	front	43.76	0	2.02	✓		
FM2	front	43.76	0	2.06	✓	✓	✓
FM3	front	43.76	0	2.1	✓		
FM4	front	43.76	0	2.14	✓		
FM5	front	43.76	0	2.17	✓		
FM6	front	43.76	0	2.21	✓		
FM7	front	43.76	0	2.25	✓		✓
FM8	front	43.76	0	2.29	✓		
FM9	front	43.76	0	2.33	✓		
FR2	front	43.76	0.36	2.06		✓	✓
FR4	front	43.76	0.36	2.14		✓	✓
FR6	front	43.76	0.36	2.21		✓	
FR8	front	43.76	0.36	2.29		✓	✓
XM1	bottom	43.88	0.01	2	✓		
RL	right	44.14	0.5	2.06			✓
XL2	bottom	44.14	0.35	2		✓	
XM2	bottom	44.14	0	2	✓	✓	✓
XR2	bottom	44.14	0.36	2		✓	
LR	left	44.14	0.5	2.06			✓
RR	right	44.39	0.51	2.06			✓
RL3	bottom	44.39	0.35	2		✓	
XM3	bottom	44.39	0.01	2	✓		
XR3	bottom	44.39	0.36	2		✓	
LL	left	44.39	0.51	2.06			✓
XM4	bottom	44.65	0	2	✓		
B	back	44.77	0	2.08	✓		✓

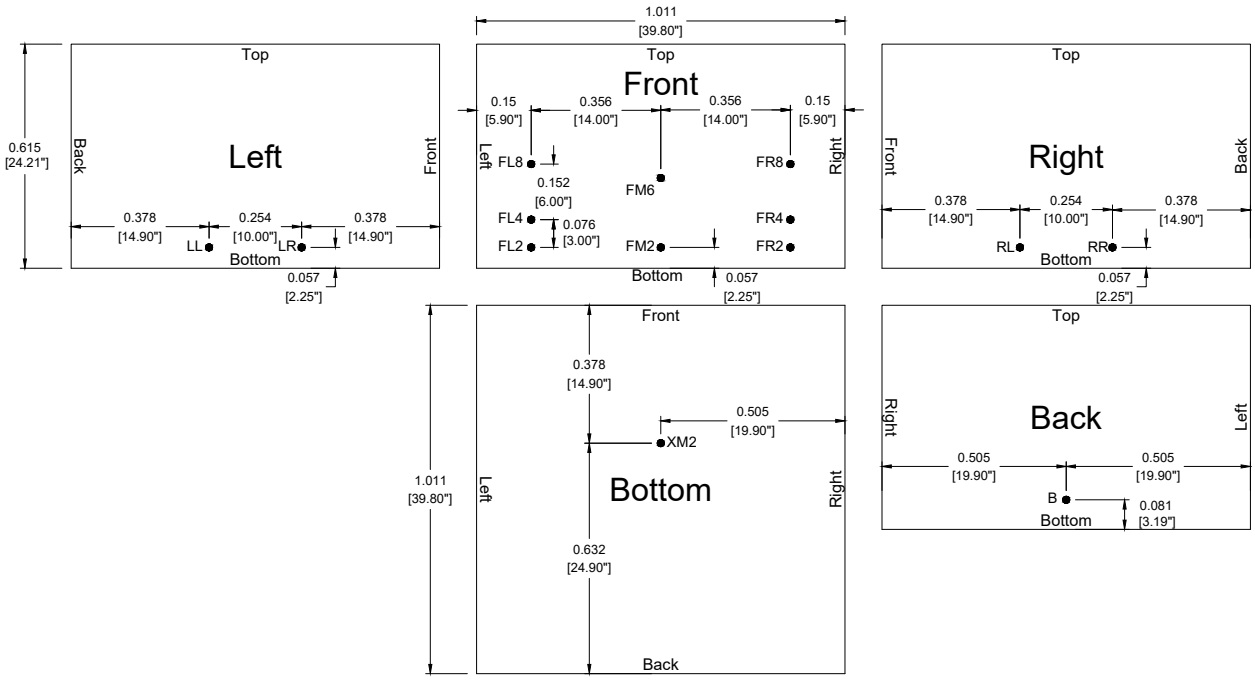

Figure 2.11: Pressure Gauge Layout 3 [35]

2.2.3 Load Measurements

The load cell layout, shown in Figure 2.12, consisted of 6 sandwich and 3 threaded load cells to measure the stream-wise, transverse and vertical wave reaction forces. The load cell naming system followed a similar pattern as the pressure gauges. The first letter denotes the face where the load cell is located. The following character denotes the horizontal location on the respective face, front (F) or upstream side and back (B) or downstream side of the box. The last letter denotes the transverse direction: right (R) and left (L).

The stream-wise horizontal reaction was measured by a load cell connected to the back face (B) of the test structure. Load cell B was a threaded rod load cell installed between the test specimen and the transverse frame. Four sandwich load cells TFL (Top Front Left), TFR (Top Front Right), TBR (Top Back Right), and TBL (Top Back Left) were on the top of the test specimen to measure the vertical reactions. The transverse reaction forces was

measured by two threaded load cells RB (Right Back) and RF (Right Front). The transverse load cells were connected to the longitudinal support frame.

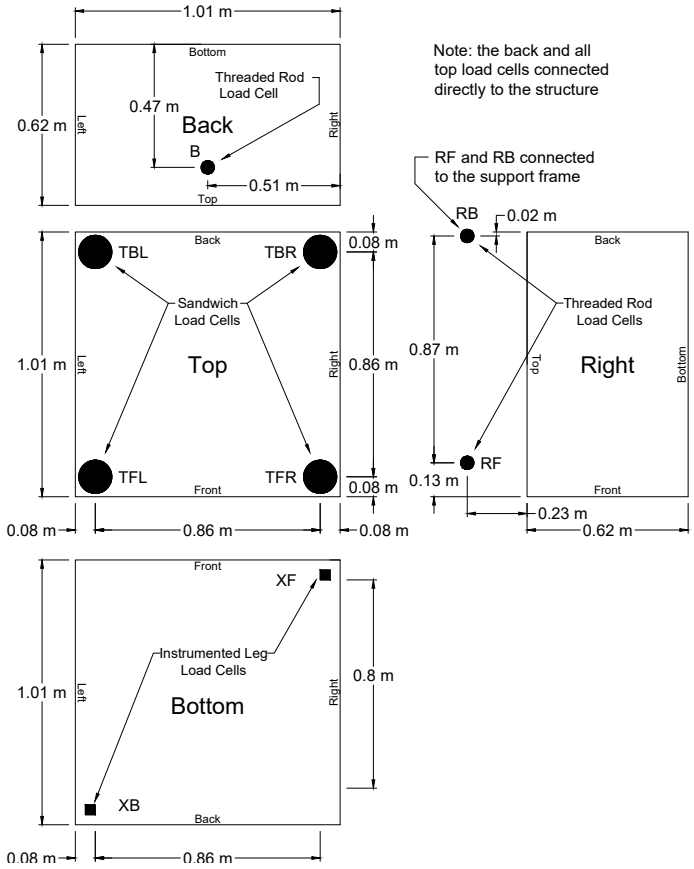

Figure 2.12: Load Cell Layout [35]

Load cells, XF and XB were sandwich type load cell placed on two columns of the test specimen. They were positioned to measure the stream-wise directional loading on the columns. The installation of the cells is shown in Figure 2.13. The positions of each load cells is given in Table 2.3.

It is important to note that load cells XB, TRF, TFL, and TBL were added during the experiment as described in Section 2.3.2

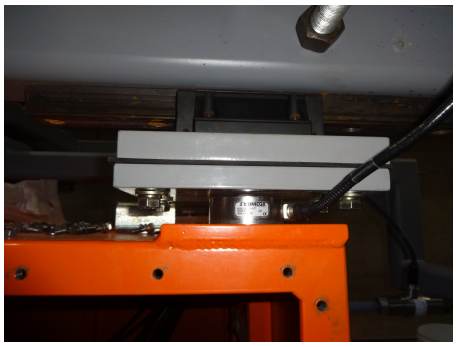

(a) Vertical Sandwich Load Cell

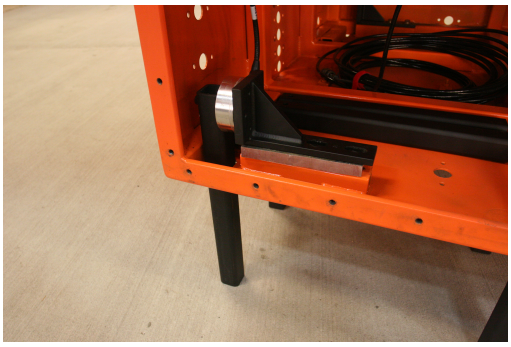

(b) Column Sandwich Load Cell

(c) Horizontal Threaded Load Cell

(d) Transverse Threaded Load Cell

Figure 2.13: Load Cells [2]

Table 2.3: Load Cell Locations

Instrument Name		Instrument Description	x (m)	y (m)	z (m)
XR	(Bottom Front)	Horizontal Load Cell	43.86	-0.45	2.05
XB	(Bottom Back)	Horizontal Load Cell	44.67	0.45	2.05
RF	(Right Front)	Transverse Load Cell	43.89	-0.77	2.85
RB	(Right Back)	Transverse Load Cell	44.76	-0.77	2.84
B	(Back)	Horizontal Load Cell	44.7	0	2.47
TFR	(Top Front Right)	Vertical Load Cell	43.84	-0.43	2.66
TFL	(Top Front Left)	Vertical Load Cell	43.84	0.43	2.66
TBR	(Top Back Right)	Vertical Load Cell	44.71	-0.43	2.66
TBL	(Top Back Left)	Vertical Load Cell	41.71	0.43	2.66

2.3 Test Conditions

2.3.1 Wave Generation

The hydraulic piston in the Hinsdale Wave Research Lab's Large Wave Flume was used to generate the waves. Two waves will be discussed in this work, the unbroken and broken waves. The wave nomenclature is a reference to their state when they inundated the box.

The hydraulic piston was operated under displacement control, which requires time history inputs. The time histories for the two waves are shown in Figure 2.14. The broken wave's time history was derived from solitary wave theory. The unbroken wave was calculated as an error function. The still water height differed for the waves: 2.0m for the unbroken wave and 1.85m for the broken wave. Depth is reported from the base of the flume floor.

2.3.2 Test Cases

Cases relevant to this work are listed in Table 2.4. All three gauge layouts were used for both the unbroken and broken waves. It is important to note that after the completion of gauge layouts 1 and 2, four load cells were added to the configuration. One horizontal column leg load cell (XB), and three vertical sandwich load cells (TRF, TFL, TBL). The horizontal threaded load cell (B) also malfunctioned during gauge layouts 1 and 2 and was replaced when the new load cells were added. A list of trials for each wave instrumentation and the load cells is presented in Table 2.5. The number of experimental trials for each pressure gauge is listed in Table 2.6.

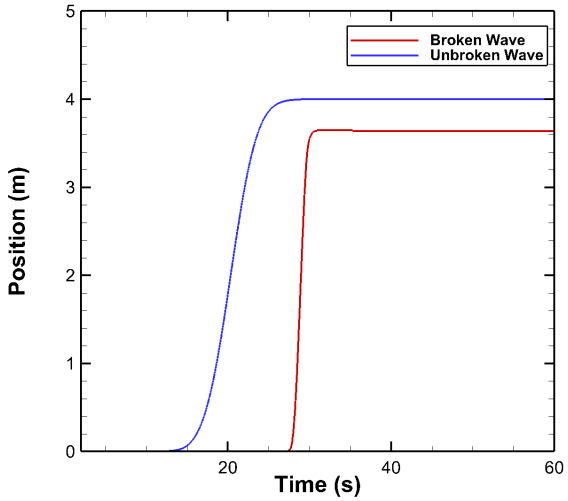

Figure 2.14: Wave Maker Displacements Time History

Table 2.4: Test Cases

Gauge Layout	Wave Type	Stillwater Depth (m)	Number of Trials
Layout 1	Unbroken	2	15
Layout 1	Broken	1.85	15
Layout 2	Unbroken	2	5
Layout 2	Broken	1.85	6
Layout 3	Unbroken	2	10
Layout 3	Broken	1.85	10

Table 2.5: Number of Test Trials for Wave Instrumentation and Load Cells

Wave Measurements			
Instrument Type	Instrument Name	Unbroken Wave Trials	Broken Wave Trials
Resistance Wave Gauge	wmdisp	30	31
	wmwg	30	31
	wg1	30	31
	wg2	30	31
	wg3	30	31
Ultrasonic Wave Gauge	uswg1	30	31
	uswg2	30	31
	uswg3	30	31
	uswg4	30	31
	uswg5	30	31
	uswg6	30	31
Acoustic Doppler Velocimeters	adv1	30	31
	adv2	30	31
	adv3	30	31
	adv4	30	31
	adv5	29	31
	adv6	30	31
	adv7	30	31
Horizontal Load Cell	XR	30	31
	XB	10	10
	B	10	10
Orthogonal Load Cell	RF	30	31
	RB	30	31
Vertical Load Cell	TRF	10	10
	TFL	10	10
	TBR	30	31
	TBL	10	10

Table 2.6: Number of Test Trials for Pressure Gauges

Load Measurements		
Instrument Name	Unbroken Trials	Broken Trials
FL2	15	16
FL4	15	16
FL6	5	6
FL8	15	16
FM1	15	15
FM2	30	31
FM3	15	15
FM4	15	15
FM5	15	15
FM6	15	15
FM7	25	26
FM8	15	15
FM9	15	15
FR2	15	16
FR4	15	16
FR6	5	6
FR8	15	16
BM1	15	15
RL	10	10
BL2	5	6
BM2	30	31
BR2	5	5
LR	10	10
RR	10	10
RL3	5	6
BM3	15	15
BR3	5	6
LL	5	10
BM4	15	15
B	25	25

Chapter 3
EXPERIMENTAL RESULTS

This chapter presents experimental observations and discusses the consistency of measurements of the wave propagation, pressures, forces and velocities. Observations regarding differences in wave form and their effects on structural loading, specifically focusing on force distribution and duration will be discussed.

Repeatability of experimental results is a very important aspect of the interpretation of experimental data. The variable and turbulent nature of a tsunami wave, particularly a turbulent bore, provides a difficult challenge to reproduce in experiments. This chapter evaluates the consistency of the wave generation and the accuracy of the measurements of the tests conducted in the Large Wave Flume. Repeatability in both the wave propagation and structural response will be quantified with a broad range of measurements. Consistency in a large data set allows for confidence in the results extrapolated from a validated numerical model.

3.1 Free Surface Elevation

The distinction between the unbroken and broken waves, shown in Figures 3.1 and Figure 3.2 respectively, is the point at which the turbulent bore forms in the flume. The bore formation for the unbroken wave occurred after the test specimen, whereas the broken wave formed into a bore upstream of the test specimen.

3.1.1 Observations

The manipulation of the bore formation is related to the initial height and velocity of the wave. The two wave initial condition are shown in Figure 3.3. The unbroken wave was

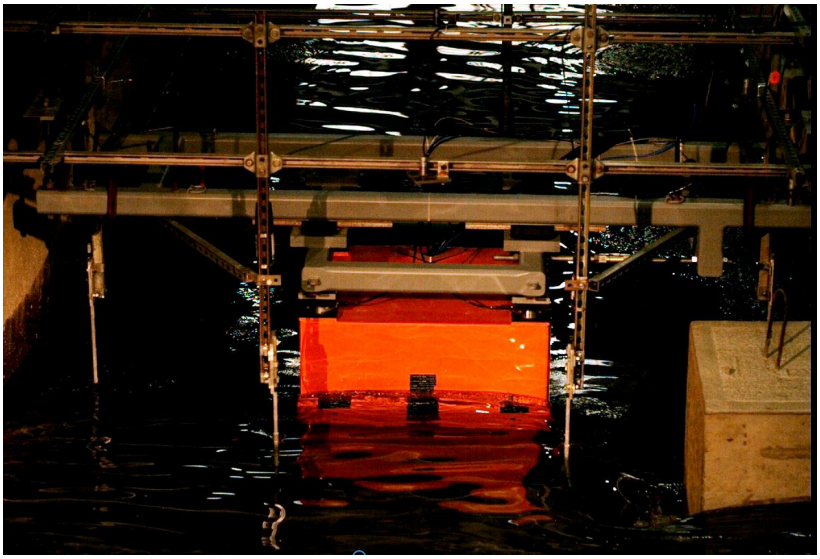

Figure 3.1: Unbroken Wave [2]

generated over 10 seconds with a maximum initial wave height of 0.3m. The unbroken wave was smooth while it inundated the test specimen and broken downstream. The broken wave was generated over 6s with a maximum wave height of 1.5m, which resulted in an earlier breaking bore. Figures 3.2 illustrates the turbulent nature of the broken bore. The whitewash of the broken bore introduced turbulence and variability into the flow. The initial impact of the broken bore on the test specimen created splashing.

3.1.2 Consistency in Results

The chaotic and complex flow of tsunami-like waves creates a challenge to consistently model experimentally. Wave repeatability can be evaluated with the wave gauge data. The wire resistance and ultrasonic wave gauges (layout shown in Figure 2.5) were used to track the wave height through the Large Wave Flume. In order to evaluate the consistency of the two wave forms, the maximum wave height for each trial were compared. The statistics of the measured wave heights are reported in Table 3.1. The maximum measured heights had a coefficient of variation of less or equal to 7.1%. The largest variability of this wave was at

Figure 3.2: Broken Wave Propagation [2]

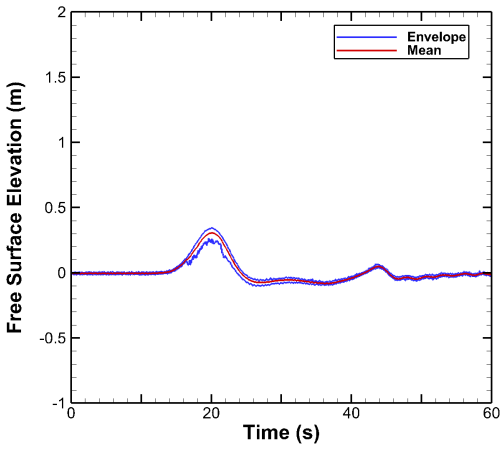

(a) Unbroken Wave

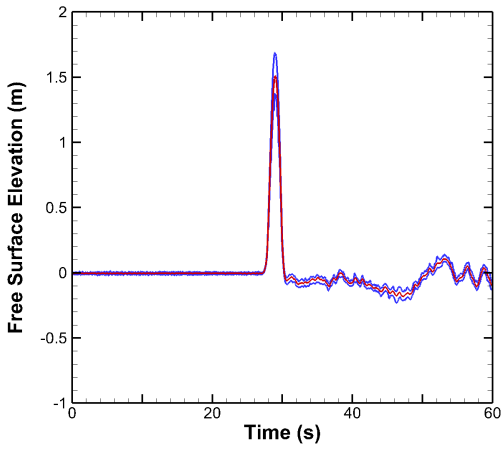

(b) Broken Wave

Figure 3.3: Free Surface Elevation Time History at the Wave Maker

initialization (wmwg). The unbroken free surface elevation envelopes are shown in Figure 3.4. The repeatability of the wave form is seen in the unnoticeable difference between the minimum and maximum wave-height values.

Table 3.1: Statistic of Wave Height Maximum Values

	Unbroken Wave				Broken Wave			
	Trials	μ (m)	σ (m)	COV %	Trials	μ (m)	σ (m)	COV %
wmwg	n = 30	0.32	0.02	7.1	n = 31	1.52	0.11	7.4
wg1	n = 30	0.27	0.01	4.1	n = 31	1.25	0.02	1.8
wg2	n = 30	0.3	0.01	1.8	n = 31	0.85	0.02	2.7
wg3	n = 30	0.31	0	1.3	n = 31	0.57	0.07	11.7
uswg1	n = 30	0.34	0.01	1.7	n = 31	0.65	0.06	9.2
uswg2	n = 30	0.42	0.02	5.3	n = 31	1.05	0.56	-
uswg3	n = 30	0.54	0.02	3.9	n = 31	1.12	1.02	-
uswg4	n = 30	0.41	0	0.9	n = 31	0.64	0.54	-
uswg5	n = 30	0.32	0	1.1	n = 31	0.52	0.05	9.6
uswg6	n = 30	0.37	0	0.8	n = 31	0.64	0.06	9.0

The measurements of the broken bore varied more because of the wave's turbulence and splashing. The ultrasonic wave gauges, uswg, used to track the wave around the test specimen were sensitive. If a gauge was splashed, the accuracy of the measurement was affected. Therefore as the broken wave created splashing around the box, most of the data collected by the three ultrasonic wave gauges closest to the structure (uswg2, uswg3, and uswg4) were unreliable and not presented here.

As the differentiator between the two wave forms is the point at which they become a bore, the wave height variability should be comparable when both waves were in the unbroken state. The broken wave begins to form into a bore after wg2. The wave height variability before the broken wave breaks was similar or less than the unbroken wave, as seen in Table

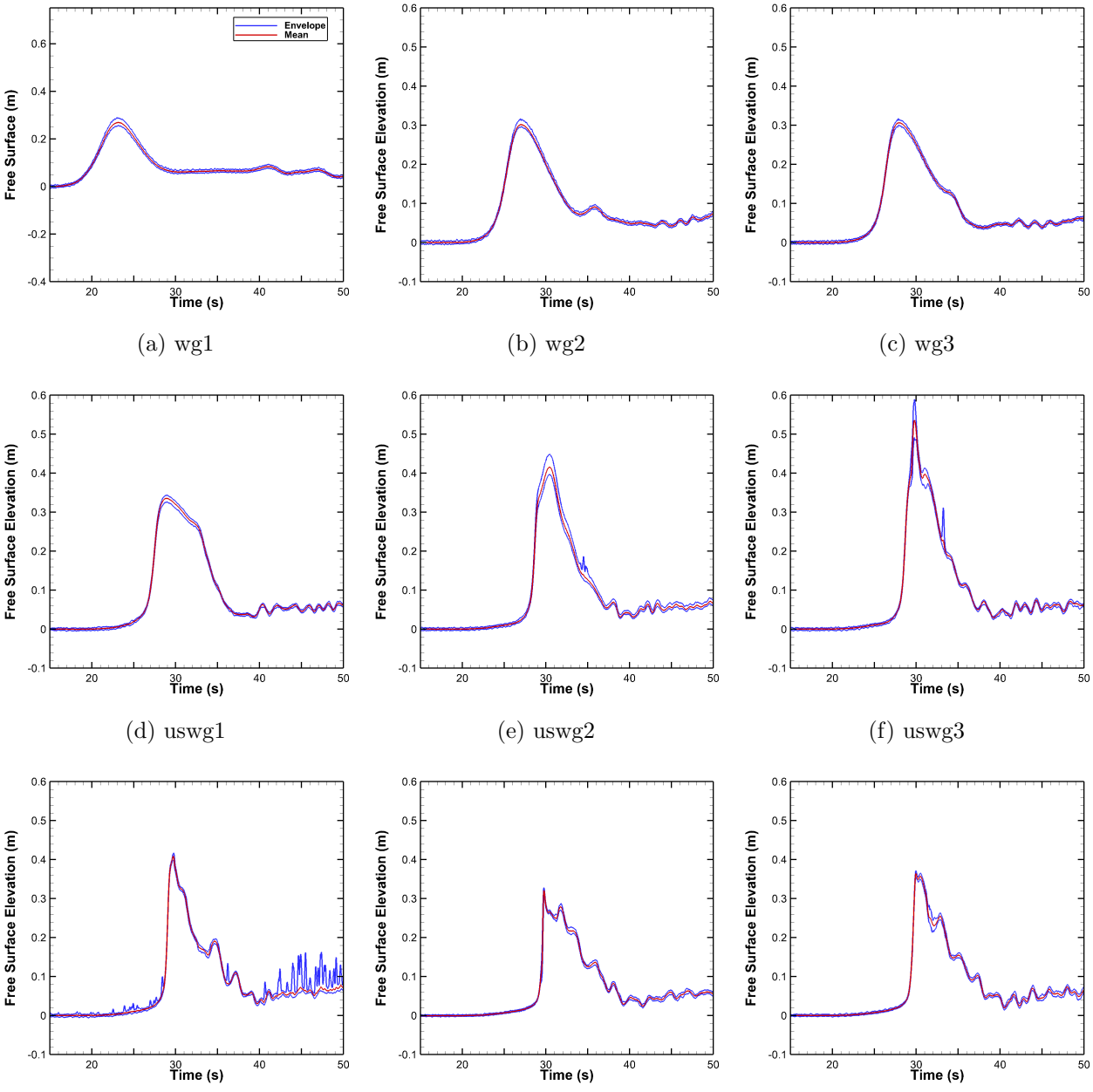

(a) wg1 (b) wg2 (c) wg3

(d) uswg1 (e) uswg2 (f) uswg3

(g) uswg4 (h) uswg5 (i) uswg6

Figure 3.4: Wave Height Histories: Unbroken Wave

3.1. For all gauges located after the breaking point of the broken wave, the coefficient of variation of the maximum wave height was larger for the broken wave than the unbroken wave

The broken wave gauge envelopes are shown in Figure 3.5. The time histories for uswg2, uswg3 and uswg4, while not reliable, are included in Appendix A for completeness.

Although instrumentation malfunctioning failed to report the repeatable nature of the broken wave around the test specimen, confidence in the unbroken wave at these gauges and in the other measurements allows reliability in the broken wave generation. The confidence in a repeated waveform allows data analysis with an assumption of a consistent wave throughout the experiments.

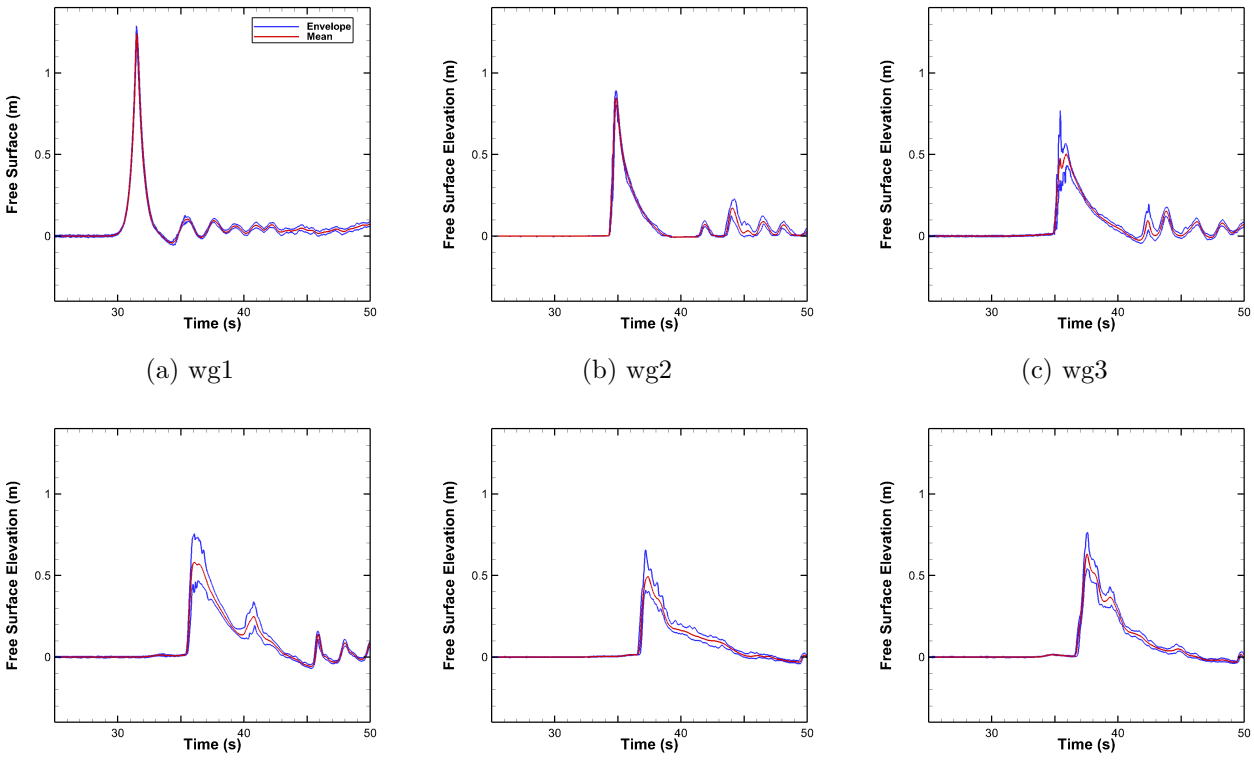

(a) wg1 (b) wg2 (c) wg3

(d) uswg1 (e) uswg5 (f) uswg6

Figure 3.5: Wave Height Histories: Broken Wave

3.2 Force Measurements

The stream-wise, transverse, and vertical load cells were used throughout the experiments to measure the reaction of the structure to the waves. The load cells measured the reaction forces of the structure. The load cell experimental configuration is shown in Figure 2.12.

3.2.1 Observations

The load cell measurements have been normalized by the maximum mean of all load cell data sets (Figure 3.6a. The load cell envelopes for the unbroken wave are shown in Figure 3.6 and for the broken wave in Figure 3.7. The difference in magnitude of the reactions is due to the wave generation as discussed in the previous section. The total stream-wise reaction force was measured by load cell B. Four load cells measured the vertical reaction force of the structure (TFR, TFL, TBR, TBL), and two load cells (RF and RB) measured the transverse force. Two load cells (XR and XB) measured the amount of stream-wise force subjected to the attached columns.

A notable difference exists in the distribution of forces from the two wave conditions. The total vertical, stream-wise and transverse reaction forces, determined by summing load cells acting in the same direction, is seen in Figure 3.8. The unbroken wave vertical reaction force was larger than the stream-wise force. This is explained by the large reaction forces measured by the top load cells. Specifically load cell TBR and TBL had peak forces similar to load cell B, as seen in Figure 3.6. As opposed to the unbroken wave, the impulsive broken bore resulted in large stream-wise force. As seen in Figure 3.8b, the majority of the force generated by the broken bore is concentrated in the horizontal direction.

The load cells placed on the attached columns (XR and XB) were added to the structure to specifically measure the contribution of the lateral force absorbed by the columns. These columns were added to the test structure to mimic a typical coastal elevated structure. As seen in the load cell force envelopes for both waves, the registered reaction forces were negligible.

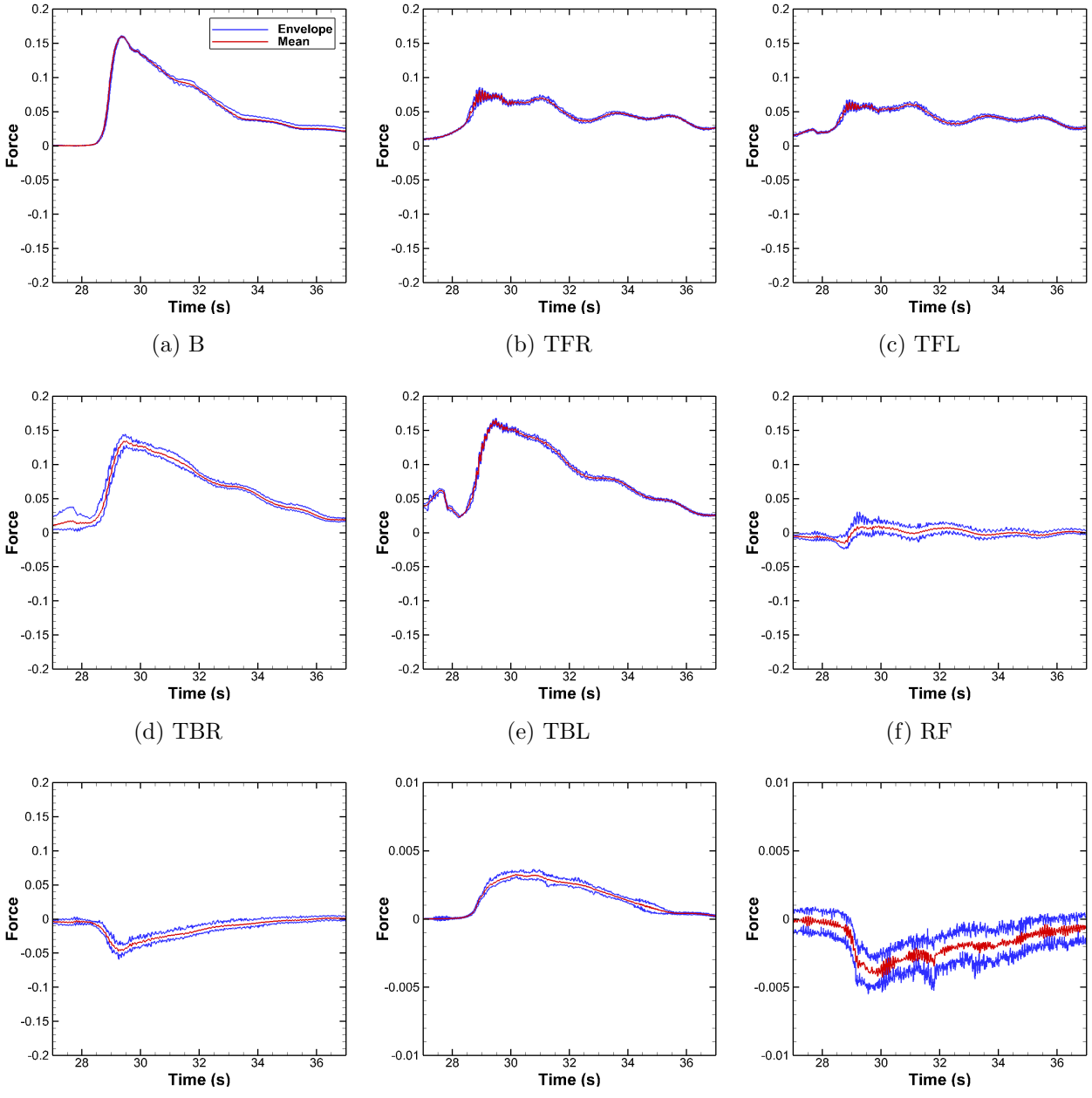

(a) B (b) TFR (c) TFL

(d) TBR (e) TBL (f) RF

(g) RB (h) XR (i) XB

Figure 3.6: Force Envelopes: Unbroken Wave

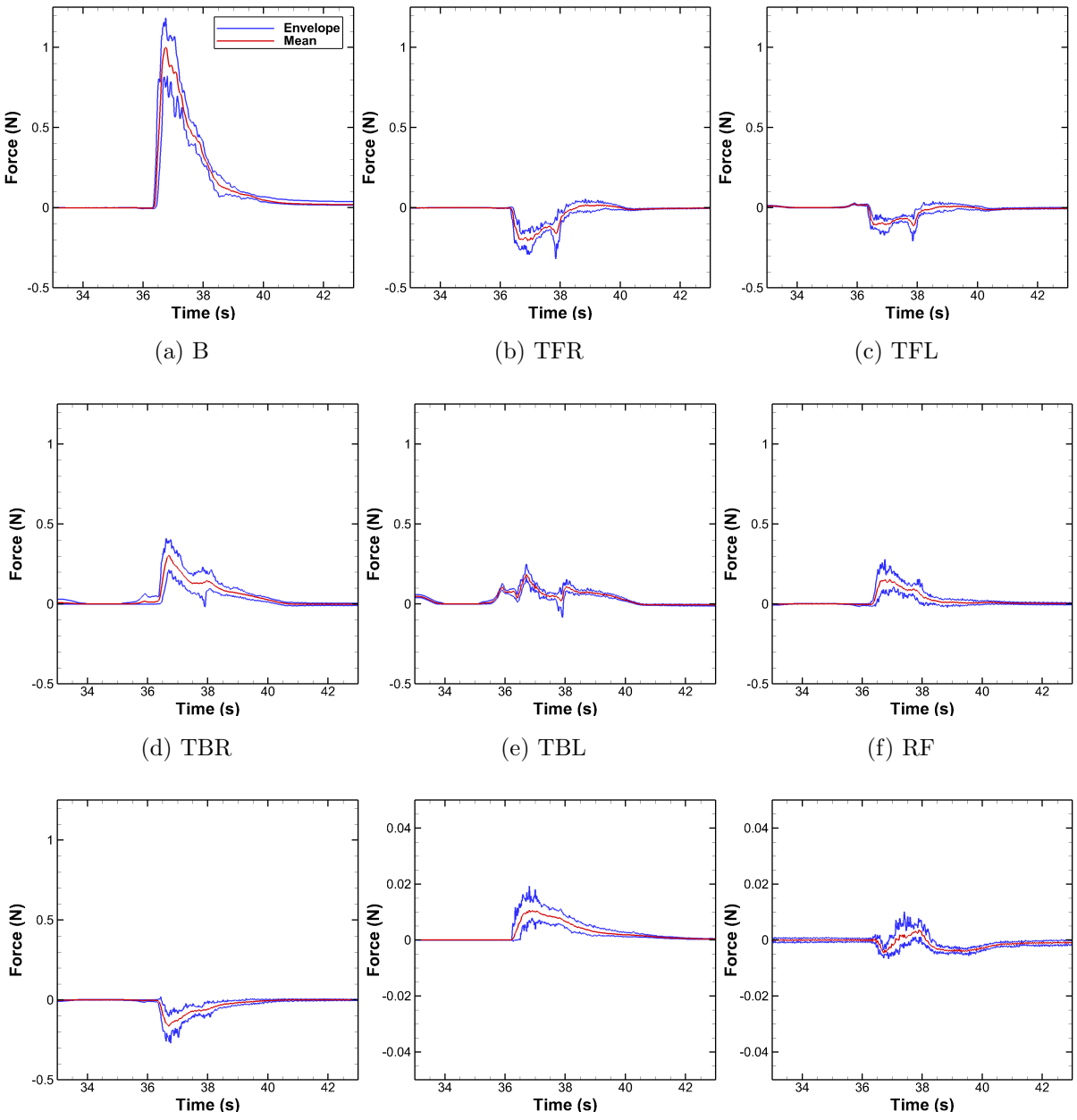

(a) B (b) TFR (c) TFL

(d) TBR (e) TBL (f) RF

(g) RB (h) XR (i) XB

Figure 3.7: Force Envelopes: Broken Wave

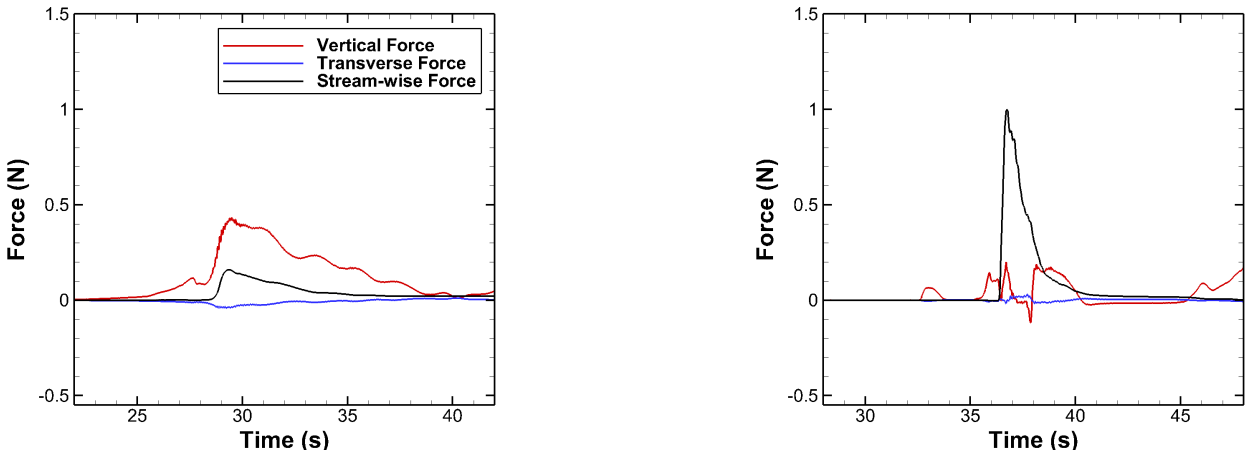

(a) Unbroken

(b) Broken

Figure 3.8: Force Summations

3.2.2 Consistency in Results

Statistics of the force measurements are shown in Table 3.2.2. The unbroken load cells had less than a 7% variation through out the experiment. The broken wave was expected to show more variability (COV <23%), due to its turbulent nature. The stream-wise force measurement (B), has the lowest COV for both the unbroken and broken wave data sets. This measurement is particularly important as it was used to validate the test specimen's front face pressure measurements as well as numerical data.

3.3 Pressure Measurements

Pressure gauges measure local fluid-induced pressures on the test specimen. In contrast to load cells which measure the response of the structure, pressure gauges measure input into the structural system. This measurement allows a better understanding of the interaction of the loading and structural behavior.

Table 3.2: Statistic of Maximum Force Values

	Unbroken				Broken			
Load Cell	Trials	μ (N)	σ (N)	COV %	Trials	μ (N)	σ (N)	COV %
XR	n = 30	16.9	0.61	3.6	n = 31	68.7	9.99	14.5
XB	n = 10	25.6	0.75	2.9	n = 10	33.4	7.38	22.1
RF	n = 30	167	6.25	3.7	n = 31	1020	127	12.4
RB	n = 30	253	15.7	6.2	n = 31	1040	136	13.1
B	n = 10	785	3.93	0.5	n = 10	5290	332	6.3
TFR	n = 10	474	3.26	0.7	n = 10	1260	147	11.7
TFL	n = 10	439	3.7	0.8	n = 10	754	117	15.5
TBR	n = 30	675	22.8	3.4	n = 31	1650	242	14.6
TBL	n = 10	814	6.92	0.9	n = 10	968	118	12.2

3.3.1 Observations

The front face pressure gauges time history variability for the unbroken wave are shown in Figures 3.9 and 3.10, for the middle and side gauges respectively. The pressure varied little along the traverse direction of the front face. This is best shown in Figure 3.10 where the front left and front right pressure gauges are presented together. Pressure gauges located at the same vertical elevation had nearly identical pressure time histories. As seen in all gauges, the pressure was uniformly distributed around the structure as all pressure gauges had a similar magnitude, including the pressure gauges on the bottom shown in Figure 3.12.

The complexity of the broken bore is best shown through the pressure gauge data. The short duration of the wave impact is seen through the front pressure gauges in Figures 3.13 and 3.14. The impulsive wave of the fully broken bore resulted in the pressure concentrated on the front face of the test structure. The front face experienced three times the amount of pressure as the side and bottom faces as seen in Figures 3.15 and 3.16.

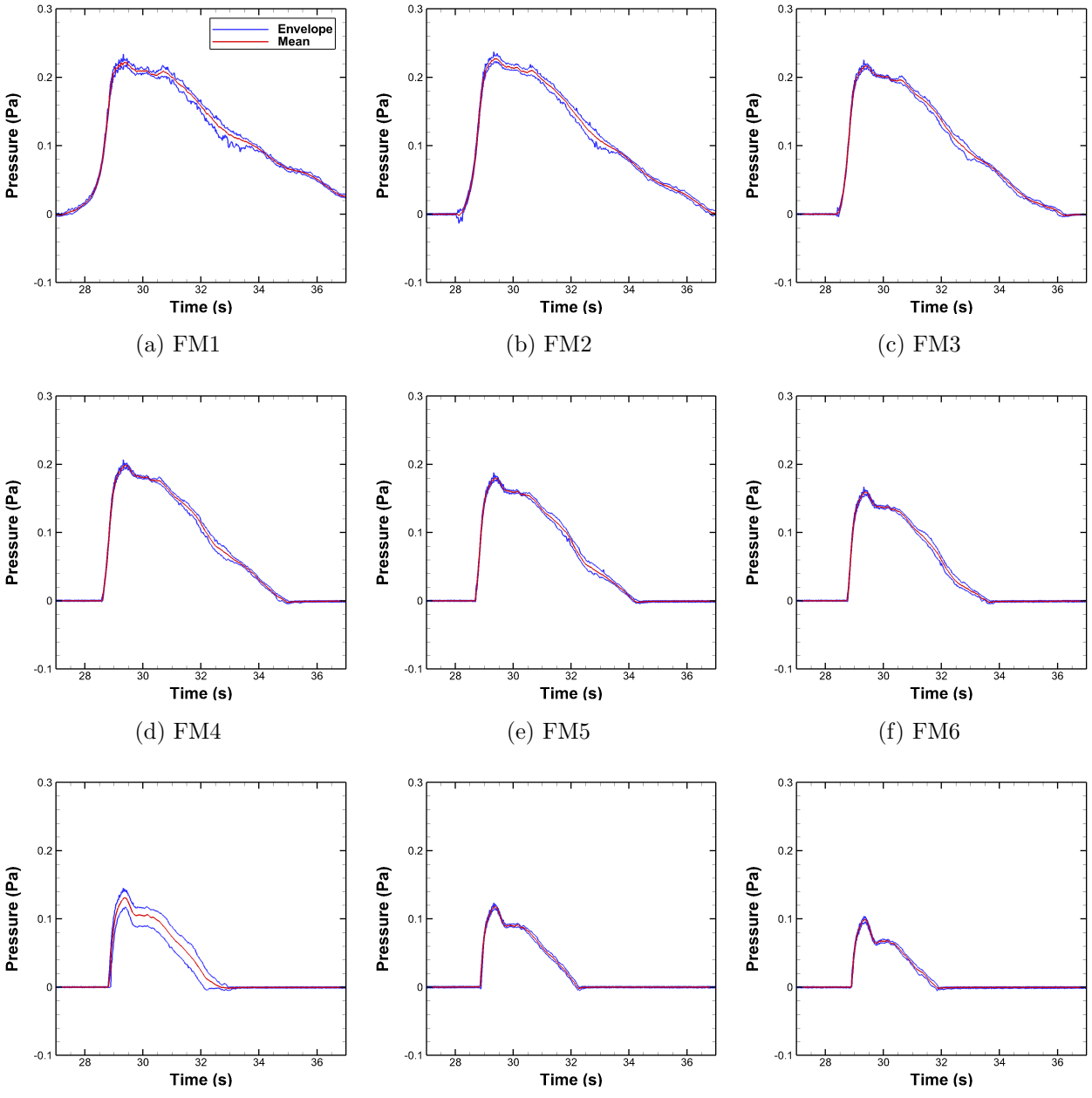

(a) FM1 (b) FM2 (c) FM3

(d) FM4 (e) FM5 (f) FM6

(g) FM7 (h) FM8 (i) FM9

Figure 3.9: Front Face Middle Pressure Envelopes: Unbroken Wave

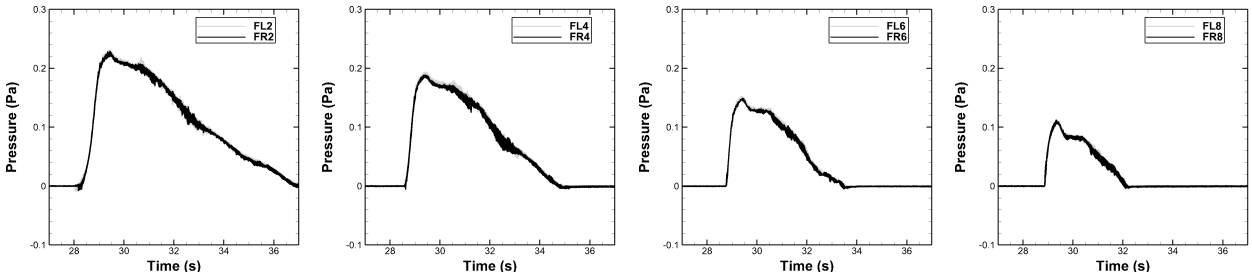

(a) FR2 and FL2 (b) FR4 and FL4 (c) FR6 and FL6 (d) FR8 and FL8

Figure 3.10: Front Face Right and Left Pressure Envelopes: Unbroken Wave

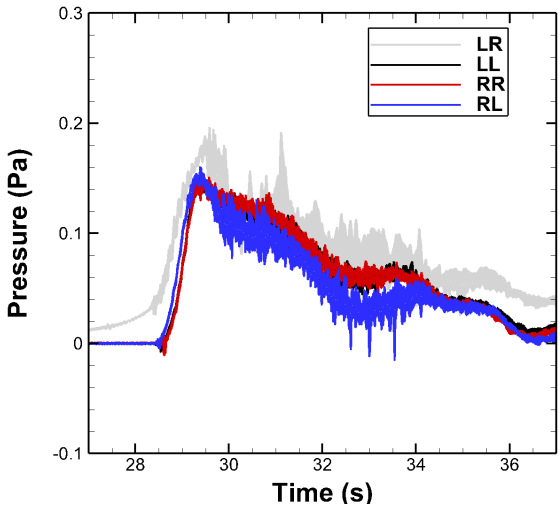

Figure 3.11: Right and Left Face Pressure Envelopes: Unbroken Wave

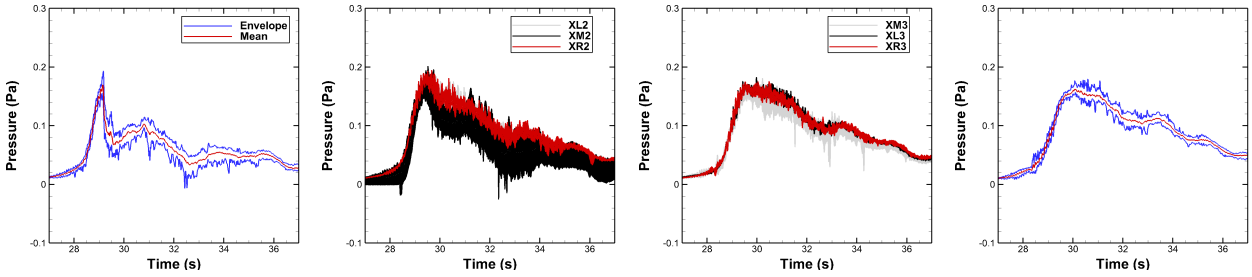

(a) XM1 (b) XM2, XL2, and XR2 (c) XM3, XL3, ans XR3 (d) XM4

Figure 3.12: Bottom Face Pressure Envelopes: Unbroken Wave

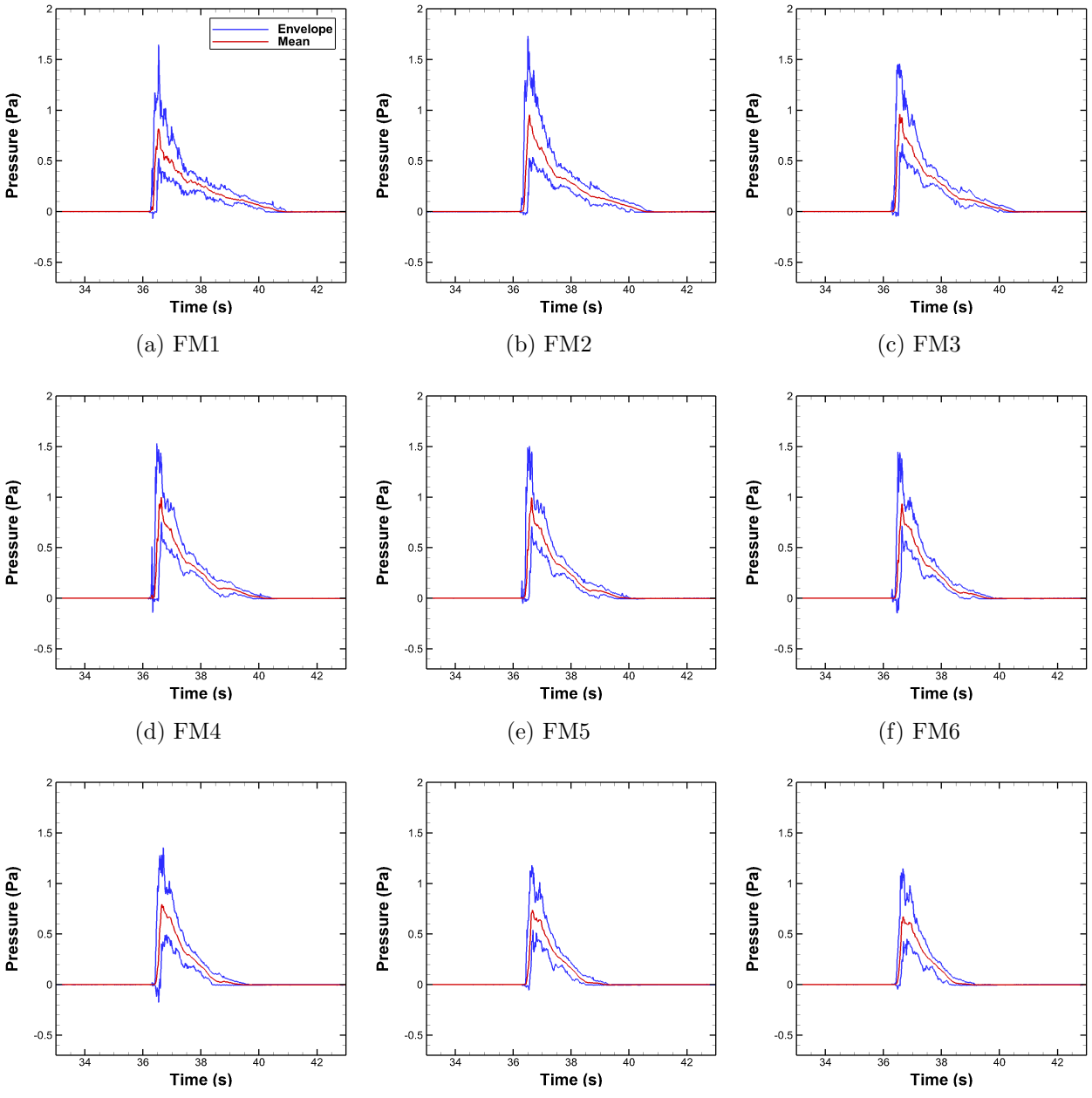

(a) FM1 (b) FM2 (c) FM3

(d) FM4 (e) FM5 (f) FM6

(g) FM7 (h) FM8 (i) FM9

Figure 3.13: Front Face Middle Pressure Envelopes: Broken Wave

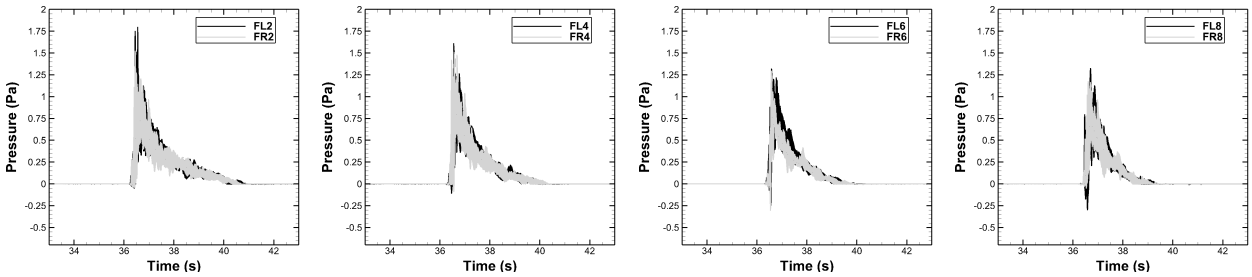

(a) FR2 and FL2 (b) FR4 and FL4 (c) FR6 and FL6 (d) FR8 and FL8

Figure 3.14: Front Face Right and Left Pressure Envelopes: Broken Wave

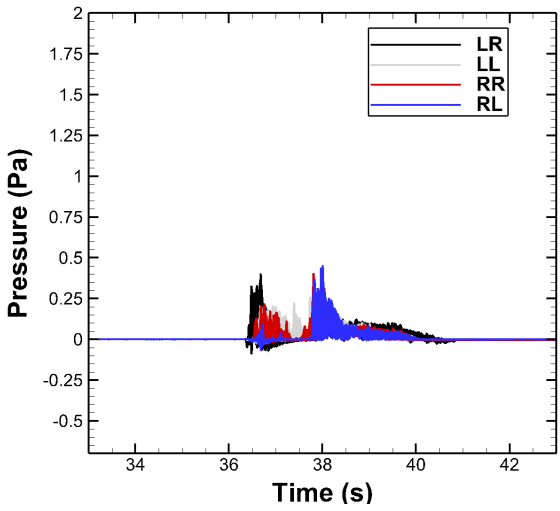

Figure 3.15: Right and Left Face Pressure Envelopes: Broken Wave

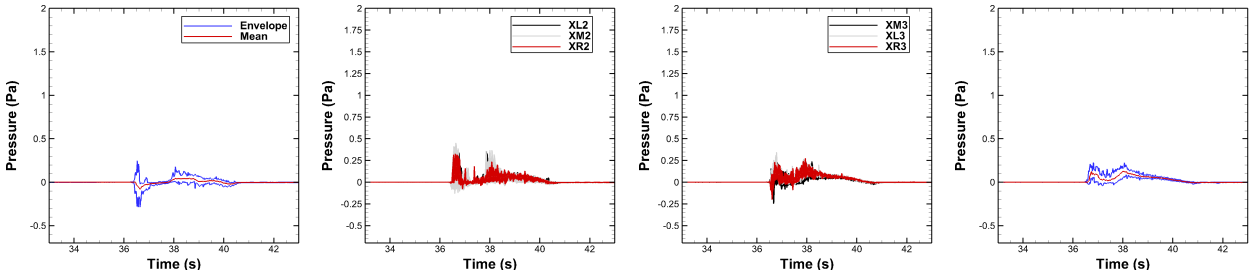

(a) XM1 (b) XM2, XL2, and XR2 (c) XM3, XL3, ans XR3 (d) XM4

Figure 3.16: Bottom Face Pressure Envelopes: Broken Wave

3.3.2 Consistency in Results

Consistent localized pressure measurements show a predictable fluid structure interaction and loading behavior. Consistent wave structure interaction is critical to understanding the behavior of the imposed load. As seen in the unbroken pressure gauge envelopes, there was no noticeable difference between the minimum, maximum and mean values for the front gauges. The statistics of the pressure gauge maximum values are presented in Table 3.3. The coefficient of variation of maximum pressure is less than 5% for 28 of the 30 maximum reported unbroken pressures.

The short wave duration for the broken wave resulted in more variable data. For instance, the front pressure gauges extreme maximum value, on average, is 1.5 times greater than the extreme minimum. This is further shown in Table 3.3, where the variation of the maximum broken pressure is less than 40%.

3.4 Velocity Measurements

Only the stream-wise direction velocity is presented here as it is representative of the accuracy of the velocity data in the other directions. All other ADV time history are included in Appendix A. The ADVs were placed just above the flume floor. The velocity data collected provides information about how the two waves varied and the change in velocity at the flume floor after structural impact. As seen through the ADV time history in Figures 3.17 and 3.18, for the unbroken and broken waves respectively, the ADVs were very sensitive resulting in highly varied data. In all other intramentation, the unbroken wave data is more consistent than the broken wave. However, this trend is not continued for the ADV data as shown in Table Table 3.4. Therefore the ADV data will not be extensively discussed in this work.

3.5 Summary and Conclusions

This chapter discussed the experimental observations and highlighted the consistency of the wave propagation, as well as the pressure and load cell time histories. The similarities

Table 3.3: Statistic of Pressure Gauge Maximum Values

	Unbroken				Broken			
Gauge Name	Trials	μ (Pa)	σ (Pa)	COV %	Trials	μ (Pa)	σ (Pa)	COV %
FL2	n = 15	3511	30.27	0.9	n = 16	19530	3550	18.2
FL4	n = 15	2963	16.38	0.6	n = 16	19220	2411	12.6
FL6	n = 5	2331	20.47	0.9	n = 6	17630	2097	11.9
FL8	n = 15	1699	20.42	1.2	n = 16	15490	2075	13.4
FM1	n = 15	3466	46.27	1.3	n = 15	17110	2644	15.5
FM2	n = 30	3535	41.15	1.2	n = 31	18960	3263	17.2
FM3	n = 15	3365	33.49	1	n = 15	19020	3122	16.4
FM4	n = 15	3088	32.53	1.1	n = 15	19130	2785	14.6
FM5	n = 15	2801	33.61	1.2	n = 15	18720	3054	16.3
FM6	n = 15	2487	28.94	1.2	n = 15	17520	2822	16.1
FM7	n = 25	2039	162.4	8	n = 26	15710	2535	16.1
FM8	n = 15	1845	23.83	1.3	n = 15	15330	1990	13
FM9	n = 15	1550	30.26	2	n = 15	14330	2279	15.9
FR2	n = 15	3489	24.02	0.7	n = 16	17330	2961	17.1
FR4	n = 15	2899	13.34	0.5	n = 16	17540	3321	18.9
FR6	n = 5	2287	13.7	0.6	n = 6	16030	2824	17.6
FR8	n = 15	1673	23.78	1.4	n = 16	15130	2246	14.9
RR	n = 10	2297	26.21	1.1	n = 10	4368	1484	34
RL	n = 10	2398	43.85	1.8	n = 10	4464	1685	37.8
LR	n = 10	2881	85.37	3	n = 10	4600	1109	24.1
LL	n = 10	2293	22.09	1	n = 10	4244	1370	32.3
XM1	n = 15	2738	128.3	4.7	n = 15	2884	1028	35.7
XM2	n = 30	2738	254.9	9.3	n = 31	4744	1186	25
XM3	n = 15	2570	82.05	3.2	n = 15	3230	563.8	17.5
XM4	n = 15	2656	79.99	3	n = 15	2886	331.2	11.5
XR2	n = 5	2950	40.94	1.4	n = 5	4454	820.8	18.4
XR3	n = 5	2662	61.22	2.3	n = 5	3456	431.6	12.5
XL2	n = 5	2865	97.2	3.4	n = 6	4462	776.5	17.4
XL3	n = 5	2695	73.56	2.7	n = 6	3911	769.7	19.7
B	n = 25	2433	51.01	2.1	n = 25	1633	367.3	22.5

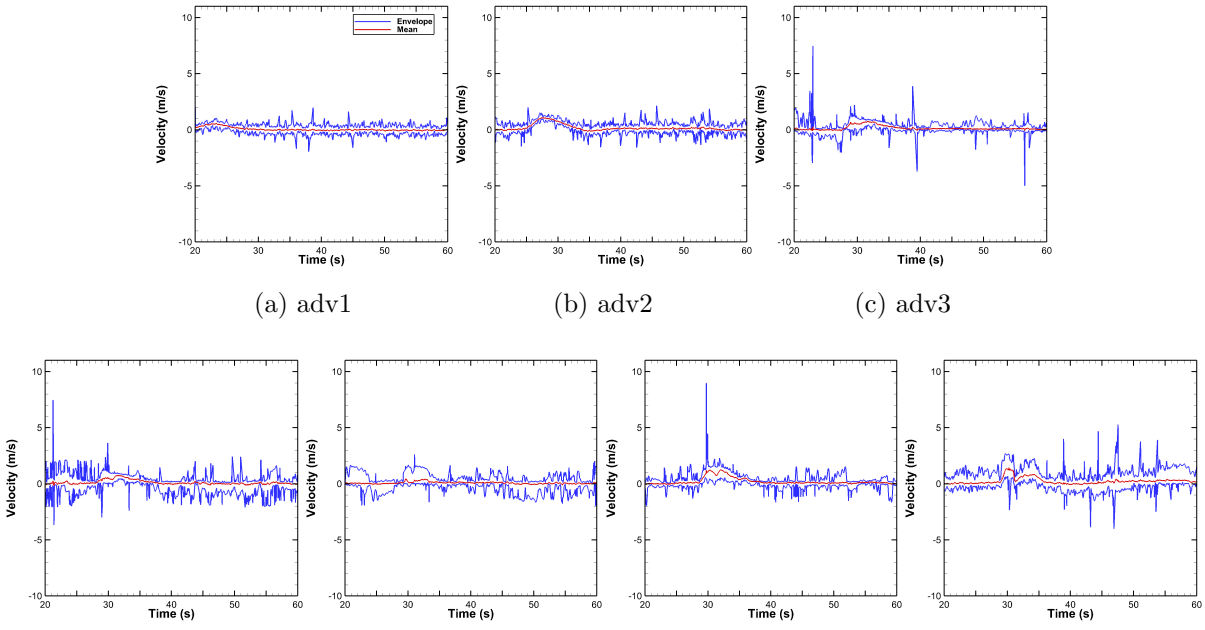

(a) adv1 (b) adv2 (c) adv3

(d) adv4 (e) adv5 (f) adv6 (g) adv7

Figure 3.17: Stream-wise Direction Velocity: Unbroken Wave

Table 3.4: Statistic of Acoustic Doppler Velocimeters Maximum Values

	Unbroken				Broken			
	Trials	μ (m/s)	σ (m/s)	COV %	Trials	μ (m/s)	σ (m/s)	COV %
adv1	n=30	2.28	6.04	265	n=31	3.89	4.31	111
adv2	n=30	1.49	0.43	28.6	n=32	4.08	2.94	72.1
adv3	n=30	2.48	3	121	n=33	8.65	17.5	202
adv4	n=30	2.75	4.54	165	n=34	3.69	2.64	71.4
adv5	n=30	1.27	0.87	68.3	n=35	3.59	0.9	25.1
adv6	n=30	1.8	1.38	76.4	n=36	4.74	8.12	171
adv7	n=30	3.13	2.34	74.7	n=37	2.58	1.26	48.7

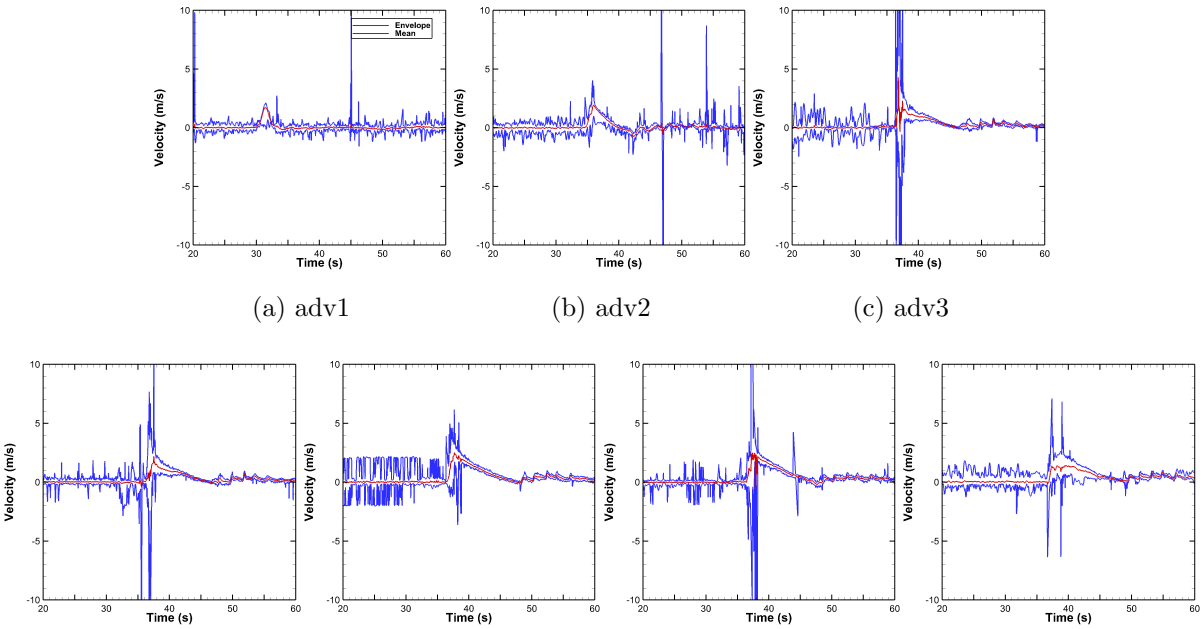

(a) adv1 (b) adv2 (c) adv3

(d) adv4 (e) adv5 (f) adv6 (g) adv7

Figure 3.18: Stream-wise Direction Velocity: Broken Wave

and differences between the two wave forms tested was illustrated through the experimental data. The distinction between the unbroken and broken wave was the point at which it became a bore in the flume. The experimental data reported similar variability when both waves are unbroken. However this was not the case after the bore formation in the broken wave. Differences in loading distribution and duration of impact can be seen through both the force and pressure data. The unbroken wave inundated the structure for around 10s and distributed the forces and pressure throughout the structure. Due to the long, slow inundation, the uplift forces of the unbroken wave were larger than the stream-wise forces. Unlike the unbroken wave, the broken wave was turbulent and impulsive. The broken wave structural impact was about 6s and the majority of the force was concentrated on the front face of the test structure and resulted in large stream-wise forces. Differences in these two waves is further seen in the consistency in the measurements. The turbulent bore generally had a greater variability in structural load cell and pressure data than the unbroken wave.

Consistency of the wave generation and propagation was shown through the wave gauges. When both waves were in the unbroken state, they reported similar variation. When the broken wave became a bore, the variability increased due to turbulence and unpredictable splashing. However, the maximum wave height varied less than 12% for all usable gauges for the broken wave while the unbroken wave reported a variation less than or equal to 7.1%. Therefore, the low variability of the wave maximum values for both waves shows wave propagation was consistent throughout the experimental tests.

The unbroken wave data was consistent, particularly for the measurements in the stream-wise direction. Load cell B, which measured the total stream-wise force, reported a coefficient of variation of 0.5% for the maximum force. The low variation in the stream-wise direction is further seen with the unbroken wave in the pressure gauges, as 16 of the 17 front face pressure gauges had a variance of less than 1.5% for the maximum pressure. Due to the transient nature of the broken wave, the variance of the measured data increased. However, similar trends seen in the unbroken wave are also seen in the broken wave data. For example, relative to the other broken load cell data, the stream-wise load cell B reported the lowest variation at 6.3%. The 17 pressure gauges on the front face had the lowest average variance for all faces at 15%, while the right face, left face, bottom face and back face average variance were 36%, 28%, 19% and 23% respectively. Therefore, both waves reported the lowest variance in data for the stream-wise direction. Repeatability in the structural reaction was shown the the load cells and pressure gauges, particularly in the stream-wise direction.

Chapter 4

ANALYSIS OF PRESSURE GAUGE DATA

This chapter presents an analysis of the test structure's front face and bottom pressure fields for the unbroken and broken wave conditions. Experimental work to date has proposed a variety of pressure distribution due to tsunami-like waves: linear [27], bi-linear [7], quadratic [30], nonlinear [22], hydrostatic [24] and uniform [14]. However, these observations have been made using on-grade structures and walls without consideration of a three-dimensional pressure field on an elevated structure. This chapter will propose the pressure distribution observed for an elevated structure subjected to an unbroken and broken wave. The pressure distributions and measured forced are also compared

The front face pressure field is of interest to gain a better understanding of the wave-structure interaction and to confirm the steam-wise the experimental load cell time history. The vertical pressures are also important, because they indicate the amount of structure uplift. Agreement of experimental pressures and forces will aid in increasing the confidence in validated numerical model results, as such models predict forces through integrated pressures.

4.1 Stream-wise Pressure Distributions

To compare the stream-wise pressure measurements to the horizontal force, the pressure field on the front face of the test structure needed to be represented accurately. The front face of the test structure had pressure gauges at 17 different locations throughout the experiment (see Figures, 2.9, 2.10, and 2.11 for gauge locations). For both wave conditions, the maximum water height exceeded the height of the highest pressure gauge. Therefore, in order to get an accurate representation of the pressure surface, the pressure field was extrapolated from the available data. Due to the consistency and accuracy of the pressure measurement data

throughout testing, as shown in Section 3.3.2, the mean value of pressure measurements at each location was used in computing the pressure field.

Linear regressions and bi-linear surface regressions were implemented using the front face pressure gauges. Eight different data fitting options were investigated. Due to the three-dimensional pressure gauge layout, two dimensional data fits were performed with and without the effects of the edge measurements. The regression without edge effects were computed using the 9 center-line pressure gauges while the regressions accounting for edge effects used all 17 gauges.

Multiple pressure distribution fits were performed to compare to the trends seen in previous experimental data. The fits were: (1) linear without edge effects, (2) linear with edge effects, (3) bi-linear surface, (4) quadratic without edge effects, (5) quadratic with edge effects, (6) bi-quadratic surface, (7) uniform, and (8) hydrostatic. All data fits, except uniform and hydrostatic, were calculated through linear regression or through bi-linear surface regressions. The uniform pressure distribution was calculated as the average pressure at each time step. Hydrostatic run-up heights were computed for all front face pressure gauges, the average of which was used to compute the effective hydrostatic pressure.

Table 4.1: Average R^2 Values During Wave Impact

	Unbroken Wave	Broken Wave
Linear Without Edge Effects	0.97	0.60
Linear With Edge Effects	0.98	0.59
Bi-Linear	0.98	0.71
Quadratic Without Edge Effects	0.98	0.61
Quadratic With Edge Effects	0.98	0.70
Bi-Quadratic	0.99	0.90
Uniform	0	0
Hydrostatic	0.94	0.26

The average coefficients of determination during wave impact for each fit are presented in Table 4.1. As seen through the results of the data fitting for the unbroken wave in Table 4.1, all of the fits calculated through linear regression had an R^2 value greater or equal to 0.97. This is because unnecessary higher order term coefficient approach zero to accurately represent the data. There is only a small increase in accuracy with the inclusion of edge effects. As the pressure on the front face of the test structure varied little in the transverse direction for the unbroken wave as seen in Figure 3.10, this is expected.

The pressure distributions at three times are presented in Figure 4.1 for the pressure data and their respective fits. The data is presented at the maximum horizontal force time interval, as well as 0.5 s before and after. One of the most notable observations from the unbroken wave was the similarity of the pressure on the front face to a hydrostatic distribution. As seen through Figure 4.1a and through the average R^2 value of 0.94, the unbroken wave exhibited hydrostatic pressure characteristics for much of the inundation. A hydrostatic pressure distribution is expected if the flow velocity is low. However, during and after maximum horizontal force, shown in Figures 4.1b and 4.1c, the pressure data does not follow a hydrostatic distribution.

Although it was not hydrostatic at maximum force, the pressure on the front face of the test structure remained linear. Through these figures and the high coefficient of determination values for all fits, it can be seen that the unbroken wave exhibited a linear pressure distribution.

The results from the broken wave regression fits are very different than the unbroken wave. From Table 4.1, the bi-surface fits were the most accurate, proceeded by the two dimensional quadratic fits and lastly the linear fits. The average R^2 values in Table 4.1 suggest that this surface was much more complex than the unbroken wave as only the bi-quadratic fit has an R^2 value ≥ 0.90.

Three broken wave time interval data and the corresponding fits are shown in Figure 4.2. The data is presents at the maximum horizontal force and 0.25s before and after. A shorter time interval is presented for the broken was due to its impulsiveness. These figures

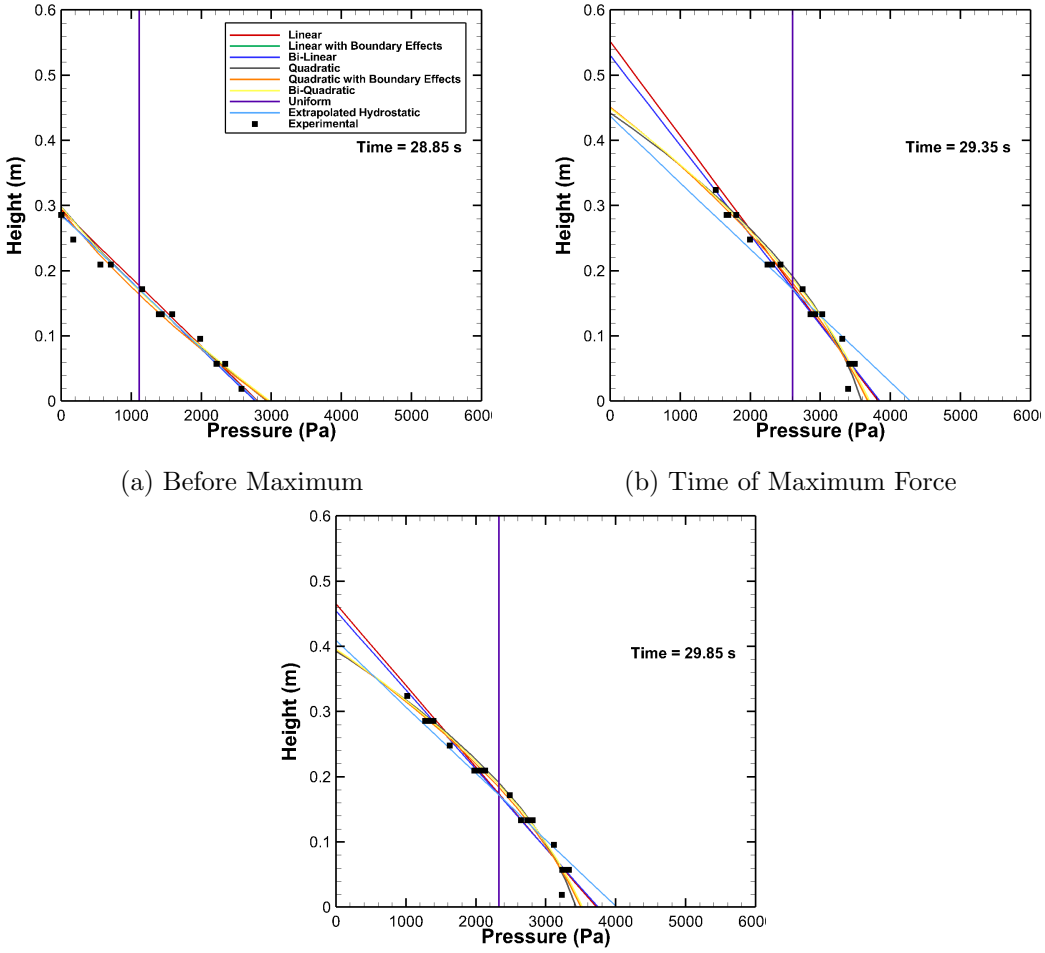

(a) Before Maximum

(b) Time of Maximum Force

(c) After Maximum

Figure 4.1: Pressure Data Polynomial Fits: Unbroken Wave

along with an R^2 of 0.90, indicate that the broken wave pressure surface assumed a quadratic shape for the much of the wave duration. The pressure distribution did initially resemble a linear shape. As the bore continues to inundate the test structure, the pressure distribution become quadratic and remained quadratic for much of the remainder of the impulsive wave.

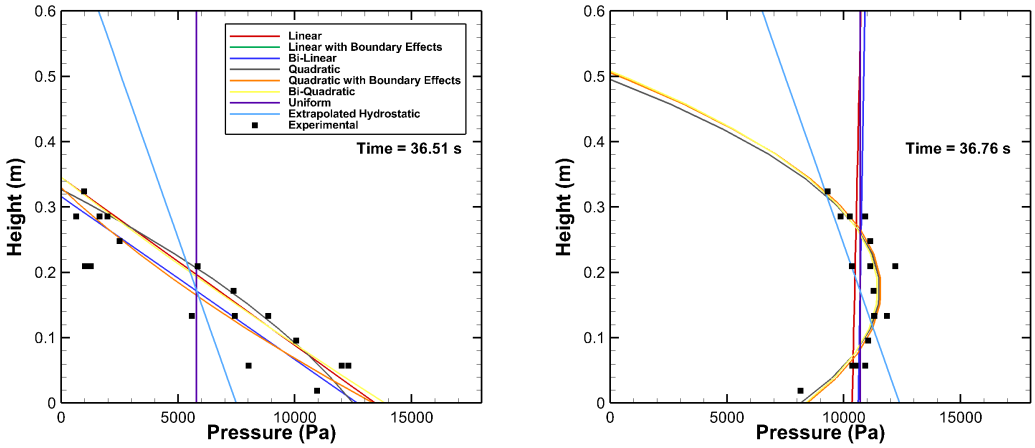

(a) Before Maximum

(b) Time of Maximum Force

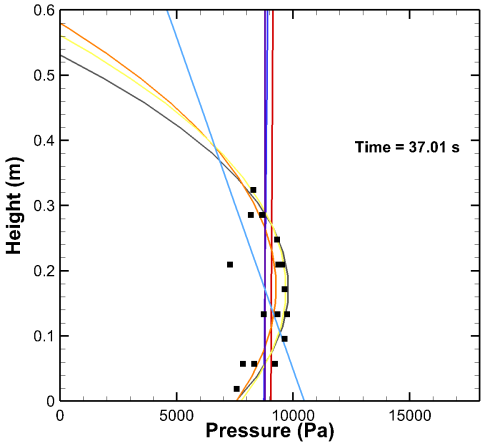

(c) After Maximum

Figure 4.2: Pressure Data Polynomial Fits: Broken Wave

4.2 Stream-wise Force Comparision

Eight pressure surfaces were extrapolated for the fits presented in the previous section. The pressure fits were integrated to compare to the experimental horizontal load cell (B) data. This load cell was attached to the test frame which was supporting the test structure. Therefore load cell B measured the total force in the stream-wise direction. A comparative total force was obtained by adding the front face resultant force to the force on the columns as recorded by XF and XB (multiplied by 6) and subtracting out the force due to pressure of the back face using the pressure measurements for gauge B and a hydrostatic assumption.

The resulting horizontal forces are shown in Figures 4.3. The unbroken force was accurately represented by all regressions while the broken force was accurately represented by the quadratic fits. Table 4.2 reports the percent difference of each pressure fit integration to the mean maximum horizontal force as recorded by the load cell B. As seen through the table and in the figure, the bi-surface linear regressions were the most accurate in representing the pressure surface for the unbroken and broken wave respectively.

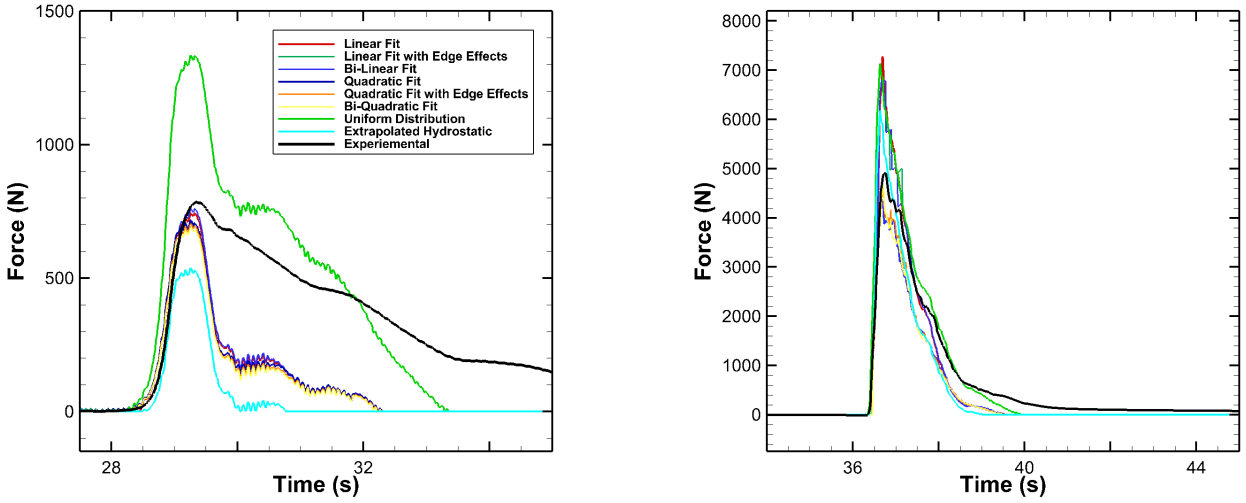

(a) Unbroken Wave

(b) Broken Wave

Figure 4.3: Stream-wise Integrated Pressure and Force Measurement Comparison

The unbroken wave bi-linear pressure surface fit maximum integrated value differed from the maximum recorded force by the load cell by 3%. The two dimensional linear regression including edge effects also had only a 3% difference from the maximum recorded horizontal force. Although the bi-quadratic fit reported the smallest R^2 values for the unbroken wave, see Table 4.1, it was the least accurate for all regression fits for predicting the maximum force. This integrated pressure surface underestimates the maximum force. Therefore the unbroken wave is best represented by a linear surface. The hydrostatic pressure distribution underestimates the unbroken wave's maximum force and the uniform pressure distribution greater over greatly over estimates the resultant force for the unbroken wave condition.

The bi-quadratic pressure integration for the broken wave condition was 5% less than the force recorded by the horizontal load cell. The only the quadratic regression fits were $\leq$ 10% of the mean maximum recorded horizontal force. All other fits overestimated the peak horizontal force by over 25%.

Table 4.2: Percent Difference Between Stream-wise Maximum Integrated Pressure and Measured Force

Assumed Pressure Distribution	Unbroken Wave	Broken Wave
Linear Without Edge Effects	5%	48%
Linear With Edge Effects	3%	38%
Bi-Linear	3%	38%
Quadratic Without Edge Effects	9%	11%
Quadratic With Edge Effects	10%	8%
Bi-Quadratic	12%	5%
Uniform	70%	45%
Hydrostatic	31%	26%

4.3 Vertical Force Comparison

To compare the vertical force and pressure measurements on the test structure, the mean of the eight bottom pressure measurements was integrated over the bottom face and compared to the vertical force measurements. The results are shown in Figure 4.4. The difference of maximum values was 15% and 56% for the unbroken and broken wave respectively. As was seen in the front face pressure distribution, the broken wave had more complex pressure distribution. If this is also true for the bottom face, the simple assumption of a uniform pressure distribution could be contributing to the large difference between the mean maximum of the pressure integration and the measured force. However, the similarities in the unbroken wave's pressure integration and measured force and agreement of time history shapes for both waves shows good agreement between the pressure and force measurements.

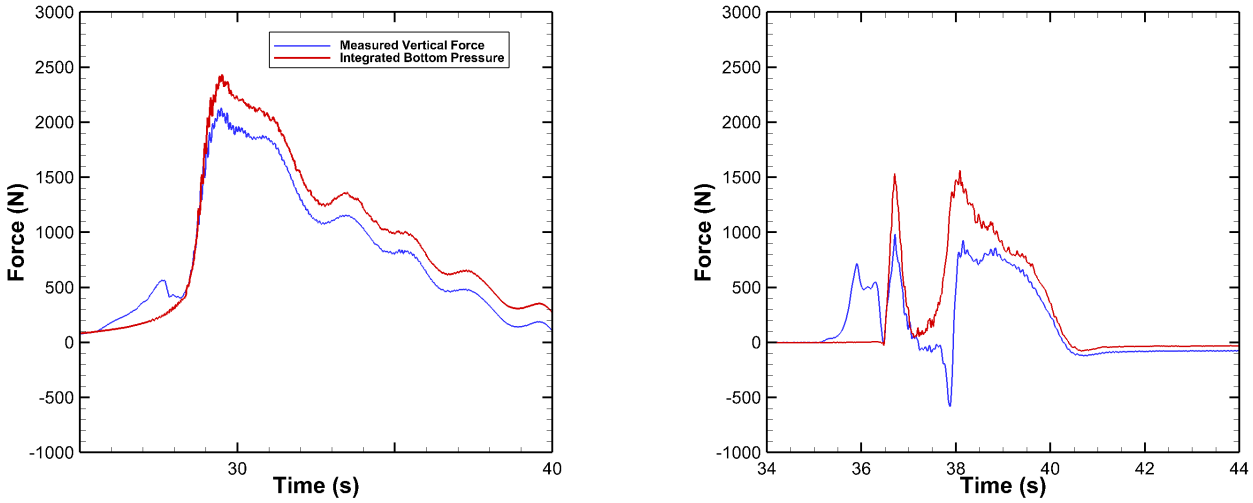

(a) Unbroken Wave

(b) Broken Wave

Figure 4.4: Vertical Force Comparison

4.4 Summary and Conclusions

This chapter presented an analysis of the front face and pressure gauges through pressure surface extraction and a corresponding extrapolated force. The unbroken wave's streamwise pressures resembled a linear distribution for wave inundation. Except during maximum horizontal force, the pressure was similar to a hydrostatic distribution. The turbulent broken wave's pressure distribution on the test structure often resembled a quadratic curve. The linear integrated pressure surfaces were in agreement with the measured force of the unbroken wave. The quadratic surface integration showed good agreement for the broken wave.

The standard experimental method of recording forces is through load cells. The standard numerical force calculation is through pressure integration on structural surfaces. A method similar to that used in numerical models, force extraction through pressures, was used on experimental data. The mean maximum force from the integrated pressures were less than or equal to 5% of the experimental load cell B. The vertical forces and pressures were also compared and showed good agreement. The agreement of the pressure integrated force with the experimental load cell shows that force calculation by way of pressure surfaces is valid in the experiment. This is an important finding in that it shows experimentally, the method of force calculations in numerical methods is valid and the same force is achieved.

Chapter 5
NUMERICAL MODEL DESCRIPTION

This chapter describes the methodology used to numerically model the Large Wave Flume at Oregon State University's O.H. Hinsdale Wave Research Laboratory in OpenFOAM. This chapter will cover an OpenFOAM overview, the numerical approach, the OpenFOAM file structure, discretization methods, the boundary conditions and application execution. The functionality of OpenFOAM is discussed in this chapter, while model specifics are discussed in Chapter 6.

5.1 OpenFOAM Overview

Open Field Operation and Manipulation (OpenFOAM) is an open source software toolbox with the functionality to solve specific problems in continuum mechanics, including computational fluid dynamics (CFD). It is comprised of C++ libraries with the capabilities to solve a wide range of CFD problems including, laminar, turbulent and multi-phase flow. The solution is reached through finite volume discretization in which the domain is subdivided in space into a finite number of contiguous control volumes.

OpenFOAM's C++ libraries are used to create executables known as applications. Its distribution includes a large number of compiled applications; however, users have the flexibility to create and modify application as long as the additions comply with the underlying methods and physics. An OpenFOAM application is comprised of two main components: a solver, and utilities. The solver solves a specific problem in computational continuum mechanics, while the utilities are involved with pre- and post-processing tasks, data manipulation or simple mathematical operations.

OpenFOAM can be downloaded online on the OpenFOAM Foundations website (`https:`

//openfoam.org/download/). OpenFOAM version 5.0 was used for this work. Slight differences in application execution might exist depending upon the system, however procedures discussed will generally be the same [11].

5.2 Numerical Approach

The OpenFOAM solver used in this work, *olaDyMFlow*, is a three-dimension dynamic mesh multiphase solver developed specifically to efficiently model fluid-structure interaction. This solver is part of the *olaFlow* package of solvers developed by Pablo Higuera. It can be downloaded from the GitHub repository (`https://github.com/phicau/olaFlow`). Based on the general OpenFOAM solver, *interFoam*, *olaDyMFlow* solves the three-dimension Reynolds Averaged Naiver-Stokes (RANS) equations for two incompressible phases by discretization of the geometry and the Volume of Fluid Method [6].

For this work, incompressible flow was assumed. The experimental velocities were lower than Mach 0.3, see Figures 3.17 and 3.18, and it was assumed that the final numerical models would produce similar velocities, therefore the water and air are assumed to be incompressible. As seen through the work of Motley et. al [19], Qin et. al [25], and Winter et. al [36], successful OpenFOAM fluid structure interaction is achieved with the use of a proper turbulence model.

5.2.1 Wave Generation

Proper wave generation is of the highest importance in numerical modeling of fluid-structure interaction. If the wave is not generated properly, the propagation will likely be flawed, leading to poor results. The generation of the numerical wave should be as close as possible to the experimental wave so that the physics are the same. To properly model the experimental program conducted in the Large Wave Flume, an OpenFOAM solver that mimics a piston wavemaker will provide the best results.

The advancements in *olaDyMFlow* are in the development of the special boundary conditions which are focused on wave generation and active wave absorption at the domain

boundaries. The special boundary condition in *olaFlow* solvers reduced the computational cost of the model by eliminating the need for buffer or damping zones typically used in numerical wave generation. *OlaFlow* can implement a wide range of wave theories and also has the functionality to mimic experimental wave generating mechanisms such as piston and flap wavemakers [6]. This work is interested in the piston wavemaker capabilities of *olaDyMFlow*.

The piston wavemaker is implemented through a solver specific boundary condition, *wavemakerMovement*. The wave is generated through a supplied piston displacement time history. The wavemaker boundary is displaced, such as a piston is in the experiment, and creates a wave. As the wavemaker boundary moves, the domain has to react to this movement. Therefore the use of dynamic mesh is necessary. The boundary movement causes a compression of cells in the direction of movement, therefore the domain points need to be updated. However, since the movement is restricted to the horizontal direction the topology of the flume mesh is preserved therefore the dynamic meshing procedures can occur relatively simply with only the concern of the horizontal point positions [5].

5.2.2 Governing Equations

The three dimensional RANS equations are implemented through the *olaFlow* solver for turbulent incompressible viscous fluids. The governing equations are the continuity equation (5.1) and momentum equation (5.2).

$$\frac{\partial U_i}{\partial x_i} = 0 \tag{5.1}$$

$$\rho\frac{\partial U_i}{\partial t} + \rho\frac{\partial}{\partial x_j}(U_i U_j) = -\frac{\partial P}{\partial x_i} + \frac{\partial}{\partial x_j}(2\mu S_{ij} - \rho\overline{u_i' u_j'}) \tag{5.2}$$

Where U_i is the average velocity in the i direction. The mass density is defined as ρ, P is the average pressure, μ is the dynamic viscosity, and S_{ij} is the mean strain rate tensor, which is defined in Equation 5.3. In turbulent flow, the field properties are expressed at the sum of the average and fluctuating component, i.e. $u_i = U_i + u_i'$, where u_i' is the fluctuating

component [21].

$$S_{ij} = \frac{1}{2}\left(\frac{\partial U_i}{\partial x_j} + \frac{\partial U_j}{\partial x_i}\right) \tag{5.3}$$

Introducing mean and fluctuating components into the governing equations, and applying the continuity equation (5.1) to the momentum equation (5.2) results in:

$$\frac{\partial U_i}{\partial t} + U_i\frac{\partial U_i}{\partial x_j} = -\frac{\partial P}{\partial x_i} + \nu\frac{\partial^2 U_i}{\partial x_j \partial x_j} - \frac{\partial \overline{u_i' u_j'}}{\partial x_j} \tag{5.4}$$

Here ν is the viscosity. Equation 5.4 has more unknowns than equaitons due to the fluctuating velocity. To close the system, the standard k-ϵ model was chosen to solve the turbulent terms [17], where k is the turbulent kinetic energy and ϵ is the rate of dissipation of the turbulent kinetic energy. These are calculated with Equations 5.5, 5.6 and 5.7.

$$k = \frac{1}{2}(u_i' u_i') \tag{5.5}$$

$$\epsilon = \frac{C_\mu^{0.75} k^{1.5}}{l_d} \tag{5.6}$$

$$\nu_t = C_\mu k^2/\epsilon \tag{5.7}$$

Here l_d is the turbulence length scale [5] and. C_μ is a model constant which has a value of 0.09 for the standard k-ϵ model [23].

5.2.3 Volume of Fluid Method

A multiphase CFD model consists of two or more immiscible fluids, such as air and water in a flume. The immiscible fluids are separated by a clearly defined interface or free surface. At domain discretization of a multiphase model, the fluid, or percentage of fluid, in each cell is specified. This specification is the volume fraction, α. For this work, the domain consists of water and air, 1 representing water and 0 representing air. The interface between the fluids ranges from 0 to 1. Using this volume of fluid approach, the fluid in the domain can be represented as one fluid with modified properties for calculation purposed. The properties

are a weighted average of the fluid comprising each cell corresponding to the cells α value. For example, Equation 5.8 represents the fluid density in the cell. Where $\tilde{\rho}$ and $\hat{\rho}$ are the fluid densities of water and air respectively. Fluid properties of water used in this work were $\tilde{\rho}$ = 1,000 kg/m^3, $\tilde{\nu} = 1.0 \times 10^{-6}$ m^2/s and for air, $\hat{\rho}$ = 1.22 kg/m^3, $\hat{\nu} = 1.48 \times 10^{-5}$ m^2/s. The movement of the fluid in the domain is calculated with the transport equations. The water and air volumes are solved separately using Equation 5.9 for water and Equation 5.10 for air [9].

$$\rho = \tilde{\rho}\alpha + \hat{\rho}(1-\alpha) \tag{5.8}$$

$$\frac{\partial \alpha}{\partial t} + \frac{\partial(\tilde{U}_i \alpha)}{\partial x_i} = 0 \tag{5.9}$$

$$\frac{\partial (1-\alpha)}{\partial t} + \frac{\partial(\hat{U}_i (1-\alpha))}{\partial x_i} = 0 \tag{5.10}$$

5.3 OpenFOAM File Structure

The typical set up of OpenFOAM's multiphase solver consists of a case directory containing the subdirectories *constant*, and *system*, and the initial time directory, *0*. At runtime, additional time directories and a *postProcessing* directory are created. The general *olaDyMFlow*'s file structure is shown in Figure 5.1. The three initial directories set up the numerical model by defining the solver, domain, boundary condition, initial conditions and fluid properties to solve the moment equation (Equations 5.4).

The directory *<case dir >/system* contains the solver and its settings. Required files are *controlDict*, *fvSchemes* and *fvSolution*. In OpenFOAM, a dictionary is determined by the specification Dict on the file name. A dictionary is a list of keyword definitions that are used by the solver or utility. The dictionary *controlDict* contains keywords that determine the simulation such as solver specification, write controls and output requests. The numerical

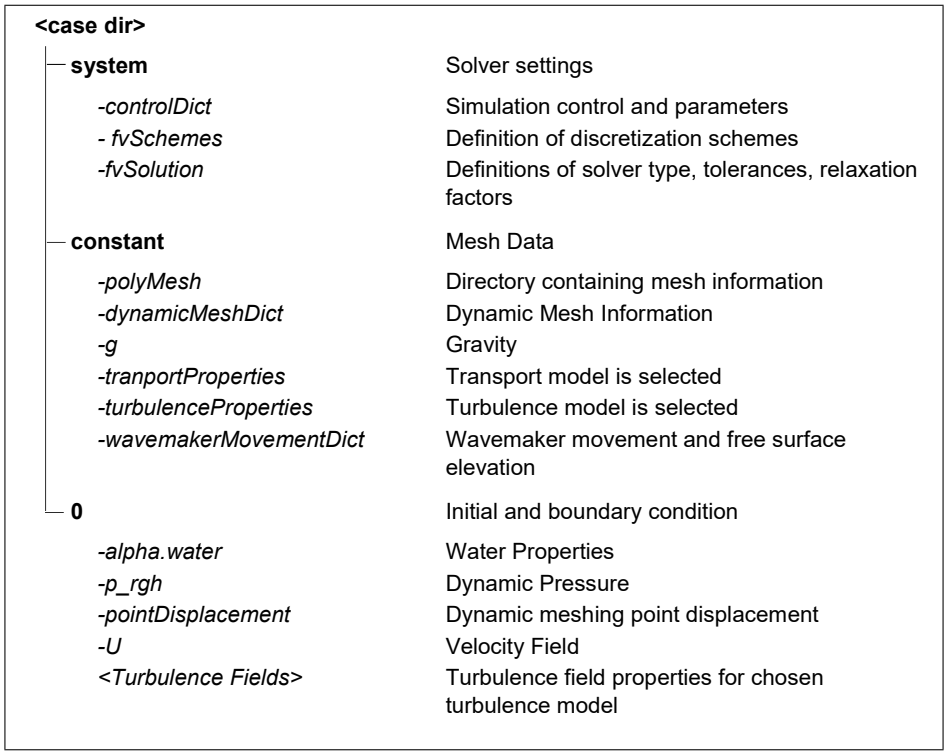

Figure 5.1: OlaDyMFlow File Structure

schemes of the simulation are defined in the *fvSchemes* file and the solution and algorithm are controlled in the *fvSolutions* file.

The analysis domain and properties are defined in $<$*case dir*$>$/ *constant*. As the directory name suggests, information contained remains constant through the analysis. For example the gravitational constant and properties of air and water are in this directory. Information pertaining to the mesh and its connectivity are also stored in the subdirectory *polyMesh*. As previously mentioned, *olaDyMFlow* is a dynamic mesh solver, therefore throughout the analysis the mesh changes. For *olaDyMFlow*, this is determined through *wavemakerMovement* boundary. The movement of this boundary is governed by *waveMakerMovementDict* which contains a time series providing the displacements of the wave maker. Specifics on the movement of the dynamic mesh are contained within *dynamicMeshDict*. For this work a uniform mesh diffusivity was used.

With the solver specified, and the domain defined, the internal fields and boundary conditions complete the simulation set up. At runtime, an OpenFOAM solver writes all relevant information in a time step directory. The next time step is completed from the previous time step. Therefore to begin the analysis an initial time step, 0, containing initial conditions is needed. The subdirectory *<case dir >/0* contains all quantities for fields required to solve the RANS equaitons such as α, ρ_{gh}, U, and parameters that are time step dependent such as the mesh movement in the case. The displacement of the dynamic mesh is determined though the information in *pointDisplacement*.

The run-time output includes the time directories storing all relevant information to continue the analysis to the next time step. Additional information can be requested as output through utilities. This data will be stored in the *<case dir >/postProcessing*. This directory is only created if the output is requested by the user [11].

5.4 Dicretization

The numerical domain of an OpenFOAM model is defined by a discrete mesh and boundary conditions. For example, the Large Wave Flume at Oregon State's O.H. Hinsdale Wave Research Laboratory was modeled in OpenFOAM and the flume walls and test structure were defined through the mesh domain and boundary conditions. The quality of the mesh highly influences the accuracy and convergence of the model. Complex regions in domains require detailed attention and refinement. Two utilities in OpenFOAM, *blockMesh* and *snappyHexMesh*, are commonly used to create and refine the domain mesh. The files and dictionaries were not included in Figure 5.1, due to the extensive resources online concering meshing in OpenFOAM.

In general, a background mesh is first created. It can be considered the initial mesh that will be refined to represent the exact geometry of the model. The complex geometries will be chiseled or molded out of this initial mesh. A background mesh consists of noncomplex shapes populated with hexahedral cells. The *blockMesh* utility allows the creation of simple hexahedral cell meshes and therefore is a popular choice to create background meshes. Using

blockMesh, the domain is divided into one or more three-dimensional, hexahedral blocks. The blocks are defined as a set of 8 vertices followed by the number of cells and cell grading in each direction. Next, the boundary regions of the background mesh are defined. The mesh boundary is comprised of distinct surfaces called patches. Boundary regions are defined as named items that consist of one or more patches. A boundary definition contains the type of boundary and the external patches included. Two common boundary types are *patch* and *wall*.

Meshing a fairly regular object is straightforward and the mesh detailing is easily defined by the user. However, meshing becomes complex with irregular objects and is too tedious for a user to define. *SnappyHexMesh*, an OpenFOAM utility, uses geometries provided in Stereolithography (STL) format to refine a background mesh around.

Before the implementation of snappyHexMesh, the STL files stored in *<case dir >/ constant/ triSurface* need to be created into a preliminary basic mesh through the execution of the OpenFOAM utility *surfaceFeatureExtract*.

There are three stages to *snappyHexMesh*: castellated mesh step, snapping step and layer addition step. The parameters for running this utility are stored in *<case dir >/ system/ snappyHexMeshDict*. The first step is to add the object into the background mesh through *castelatedMesh*. The background mesh is then refined around the edges of the extracted object. With the edge mesh surrounded by the background mesh, cells are split around the edges and refined according to parameters set in the *snappyHexMeshDict*. After surface refinement, cells are removed either inside the added object or outside. In the snapping step, the mesh snaps to the objects irregular surface. The last step, *addLayers* adds more hexahedral cell layers to reduce the number of irregular cells around the object specifically for the use of boundary layer modeling [11].

For the volume of fluid method, the value of α needs to be specified over the internal domain. Through execution of the *setFields*, after the domain mesh is complete, α is defined over the domain as specified by *setFieldsDict* [11]. More information about the *setField* utility can be found on the Open Foam Foundation website.

5.5 Boundary Conditions

The numerical domain of an OpenFOAM model is defined by the mesh and the boundary conditions. The interaction of the fluid in the domain with the boundaries defines the analysis. As mentioned in Section 5.3, the initial time directory contains field initial and boundary conditions.

Some turbulence models are only valid in the area where the turbulence is fully developed and not near domain boundaries. Due to this, additional boundary conditions need to be applied when a turbulence model is used.

Specific boundary types, as defined at mesh generation, allow certain boundary condition to be applied with ease. Therefore, the *wall* boundary type was developed to apply wall functions easily in OpenFOAM and to accurately model the turbulence flow. Wall functions apply near-wall boundary conditions for the momentum and turbulence transport equations to accurately model the turbulence in the domain.

For the sake of brevity, the boundary condition used in the work are listed below. Their specific application are discussed in Chapters 6.

- *fixedFluxPressure*: defines the mass flow through the boundary face to zero. For example, restricts the outflow of fluid through domain boundaries.

- *fixedValue*: constrains the field to a fixed value at the boundary. For example, the velocity of the fluid on a flume wall has a fixed value of 0.

- *totalPressure*: the pressure at the boundary is a total pressure condition. For example, in an open channel, the open patches would have a boundary condition of total pressure.

- *pressureInletOutletVelocity*: this boundary condition specifies that at the boundary the velocity outflow is calculated from the pressure out flow through the boundary.

- *movingWallVelocity*: velocity condition for moving wall boundaries.

- *kqRWallFucntion*: wall function for k in turbulent flow, initial conditions calculated from Equation 5.5

- *epsilionWallFunction*: wall function for ϵ turbulent flow, initial conditions calculated from Equation 5.6

- *wavemakerMovement*: boundary condition specific to *olaDyMFOAM*. This point displacement boundary condition requires displacement time histories. The boundaries connected need to be able to displace in the direction of movement. All other boundaries need to remain fixed.

- *fixedNormalSlip*: allows for movement of the boundary along a specified normal. For example, boundaries attached to the *wavemakerMovement* boundary [11].

5.6 Application Execution and Post-Processing

The advantage to running OpenFOAM on a cluster, such as the University of Washington's high-performance computing, storage, and network infrastructure, Hyak, is the ability to decrease computation time by running the model on multiple processors. OpenFOAM is able to do this by domain decomposition. The geometry in decomposed or split into pieces and allocated to multiple processors. The decomposition is accomplished through the *decomposePar* utility.

The default OpenFOAM output includes time directories that contain all the necessary information to continue to the the next time step. Function objects request additional output from the OpenFOAM model. For example, the function object *probe*, writes specified data at a given location, such as the pressure at a certain location. The function object output is stored in the *postProcessing* directory. By modeling the Large Wave Flume in OpenFOAM using the functionality described in this chapter the experimental results presented in Chapter 3 will be validated.

Chapter 6

NUMERICAL VALIDATION AND RESULTS

A numerical validation was completed to compliment the experimental tests conducted in Large Wave Flume at Oregon State University's O.H. Hinsdale Wave Research Laboratory. Several numerical simulations were performed. A validated numerical model will increase confidence in any future parametric studies as well as further the understanding of the experimental results. The agreement of experimental pressure surface integration with force measurements as shown in Chapter 4, illustrated the validity of extrapolating pressure surfaces for force measurements in experimental tests. As this is the method used by most numerical models, the validation of both the pressure and force measurements will further illustrate the credibility of numerical model predictions.

The simulation results are presented in this chapter. The proceeding section will show the correlation between the experimental measurements and numerical predictions through the agreement of free surface elevation, pressure measurements and force measurements. As the velocity measurements were not extensively discussed in this work, their numerical results are included in Appendix B.

6.1 Numerical Model Overview

The numerical conditions presented here were developed to replicate the experimental test set up as presented in Chapter 2. A three dimensional numerical domain was developed employing OpenFOAM's *blockMesh* utility. The dimensions of the numerical domain extended from the piston's initial position to the end of the Large Wave Flume. The numerical model was built so that its coordinate system would resemble the coordinate system used in the experimental set up. The coordinate system, corresponds with the flume's length ($\pm x$),

height ($\pm y$), and width ($\pm x$). The computational domain was established to reproduce the main aspects and conditions of the of the physical model. The test frame, the 12 attached columns and the sloped slab at the end of the Large Wave Flume were excluded. The test structure was added to the computational domain through OpenFOAM's *snappyHexMesh* utility. The computational domain and boundaries are presented in Figure 6.1. The background mesh consisted of $3,558,862$ hexahederal cells, with 941, 61 and 62 cells in the x, y and z direction respectively. After the the addition the test structure geometry and the execution of *snappyHexMesh*, the final domain consisted of $5,308,824$ cells.

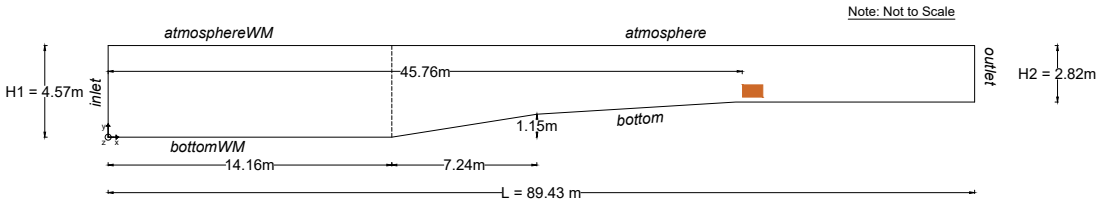

Figure 6.1: Flume Numerical Schematic

The domain consisted of 8 boundaries. The positive and negative y direction boundaries are not shown in Figure 6.1. The boundaries in the positive and negative x directions were the inlet and outlet, respectively. Boundaries *bottomWM* and *bottom* were for the negative y and *atmosphereWM* and *atmosphere* for the positive y. The boundaries *right* and *rightWM* and *left* and *leftWM* for the positive and negative z respectively. There were two boundaries for each y and z direction due to the dynamic mesh of the domain.

Through the use of the OpenFOAM solver, *olaDyMFlow*, the piston wave maker generation was numerically simulated through the solver's *wavemakerMovement* boundary condition. This boundary condition simulated the experimental piston wavemaker. The piston wave maker simulation required the inlet boundary to displace in the x direction, as a piston would, compressing the mesh in the rest of the domain. To preserve the geometry of the sloped portion of the model, the dynamic meshing was concentrated in the initial part of the flume, hence the addition of bottomWM, atmosphereWM, rightWM and leftWM boundaries.

The wavemaker displacements used in numerical simulations are shown in Figure 6.2.

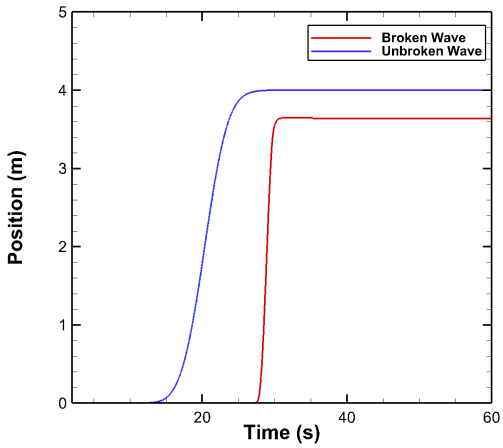

Figure 6.2: OpenFOAM Wave Inputs Wave Maker Movement

The boundary conditions used are provided Table 6.1. The application of initial fluid conditions was accomplished by specifying them at the domain's boundaries. Then, during mesh generation, they were applied throughout the domain. For both the unbroken and broken wave numerical models discussed in this chapter, the values of the volume fraction ($alpha.water$), non-hydrostatic pressure ($p_{\rho gh}$), velocity (U), turbulent kinetic energy (k),and rate of dissipation of turbulent kinetic energy (ϵ) required initial fluid conditions. The water level in the domain is specified through $alpha.water$ and is set to 1 below initial water level and zero every where else. The fluid properties of U and $p_{\rho gh}$ were set to zero along all boundaries. The turbulence properties of k and ϵ were calculated according to equations 5.5 and 5.6 using the average fluctuating velocity from experimental tests. The average velocity fluctuating velocity from both wave conditions was 0.031 m/s. The turbulent length scale, need to calculate ϵ was estimated to be 5% of the flume height for the broken wave 20% of the flume width for the broken wave [23]. Therefore, k was calculated to be 0.0014 and ϵ, 4×10^{-5} and 1.2×10^{-5} for the unbroken and broken waves, respectively.

All numerical models were executed in parallel using 64 processors. The computational run time was approximately 12 hours. Post-processing included using OpenFOAM's function

objects to record free surface elevation, pressure and force. The results showed overall good model predictions which will be discussed in the proceeding sections.

Table 6.1: Boundary Conditions

Boundary	alphawater	ϵ	κ	$p_{\rho gh}$	U	pointDisplacement
inlet	zeroGradient	epsilon-WallFunction	kqRWall-Function	fixedFlux-Pressure	movingWall-Velocity	wavemaker-Movement
outlet	zeroGradient	epsilon-WallFunction	kqRWall-Function	fixedFlux-Pressure	fixedValue	fixedValue
bottomWM	zeroGradient	epsilon-WallFunction	kqRWall-Function	fixedFlux-Pressure	fixedValue	fixedNormalSlip
bottom	zeroGradient	epsilon-WallFunction	kqRWall-Function	fixedFlux-Pressure	fixedValue	fixedValue
atmophereWM	inletOutlet	zeroGradient	zeroGradient	totalPressure	pressureInlet-OutletVelocity	fixedNormalSlip
atmophere	inletOutlet	zeroGradient	zeroGradient	totalPressure	pressureInlet-OutletVelocity	fixedValue
leftWM	zeroGradient	epsilon-WallFunction	kqRWall-Function	fixedFlux-Pressure	fixedValue	fixedNormalSlip
left	zeroGradient	epsilon-WallFunction	kqRWall-Function	fixedFlux-Pressure	fixedValue	fixedValue
rightWM	zeroGradient	epsilon-WallFunction	kqRWall-Function	fixedFlux-Pressure	fixedValue	fixedNormalSlip
right	zeroGradient	epsilon-WallFunction	kqRWall-Function	fixedFlux-Pressure	fixedValue	fixedValue

6.2 Wave Generation Validation

Validation of the wave gauges ensured that the numerical wave is taking the same form as the experimental wave. Without reproduction of similar wave forms numerically, the results would not be comparable. A comparison of the experimental and numerical waves as they inundate the test structure are shown in Figures 6.3 and 6.4 respectively. These pictures illustrate the similarities of the wave forms in the flume. The unbroken wave inundates as a smooth wave for both cases. The broken bore created a large splash on impact as shown.

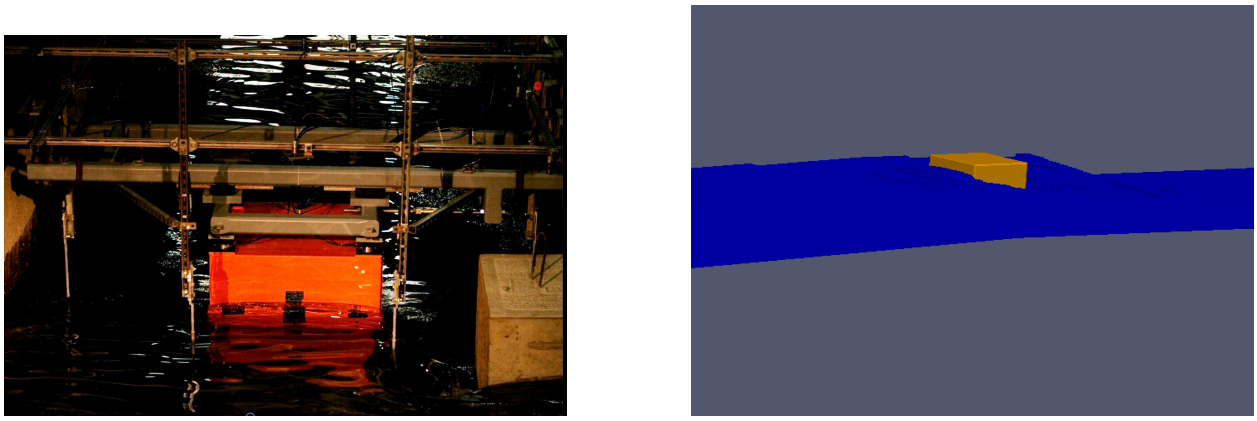

(a) Experimental Photo

(b) Numerical Photo

Figure 6.3: Experimental and Numerical Wave Comparison: Unbroken Wave

6.2.1 Free Surface Validation

The free surface elevation was measured in the numerical model at the corresponding experimental test wave gauge locations. These locations are shown in Table 2.1. The water height was measured using the OpenFOAM function object *interfaceHeight*. This function object reports the vertical distance to the interface above the specified location. The output data is similar to the data collected by the wave gauges.

The results and comparisons with experimental data for the unbroken and broken wave free surface elevations are shown in Figure 6.5 and 6.6 respectively. The differences of the

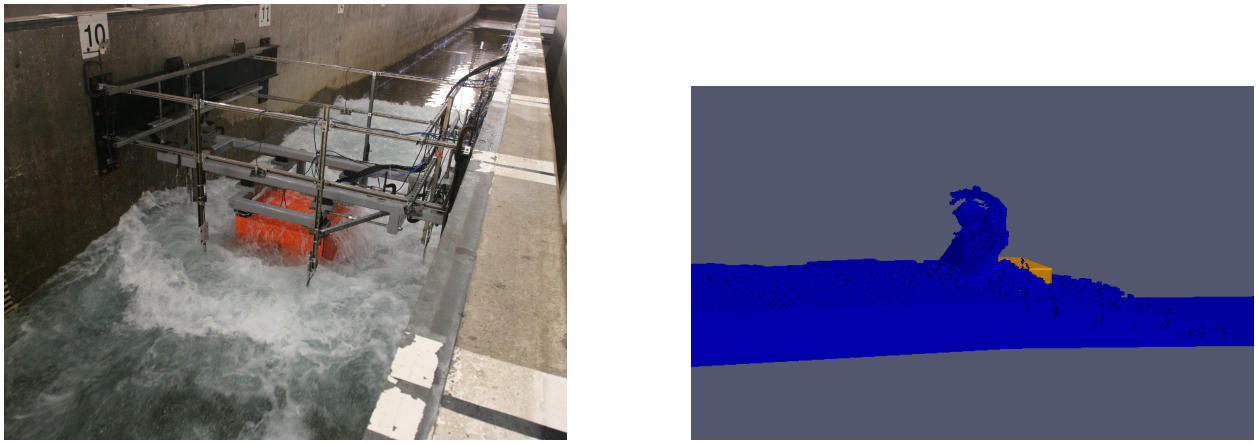

(a) Experimental Photo

(b) Numerical Photo

Figure 6.4: Experimental and Numerical Wave Comparison: Unbroken Wave

unbroken wave height at uswg3, uswg4, uswg5 and uswg6 could be due to the absence of the test structure and attached columns. The numerical model showed good agreement with the experimental data; even after the wave had passed over the location, the model showed similar results for residual water height fluctuation as shown in 6.6a. Therefore, the OpenFOAM solver *olaDyMFlow*, was able to replicate the wave generation seen in the experiment.

6.3 Test Structure Results Validation

In this section, the numerical predictions of experimental pressure and force measurements on the test structure are presented. An experimental program and an accompanying validated numerical model increases confidence in observations and results gathered from the test and model. The experimental envelope time histories are in grey while the numerical predictions are in black for the figures presented in this section.

The OpenFOAM solver used in this work, *olaDyMFlow* reaches a solution through the RANS equations and the Volume of Fluid Method. Therefore when coupled with a turbulence model, the results of the domain are in terms of non-hydrostatic pressure, velocity, volume

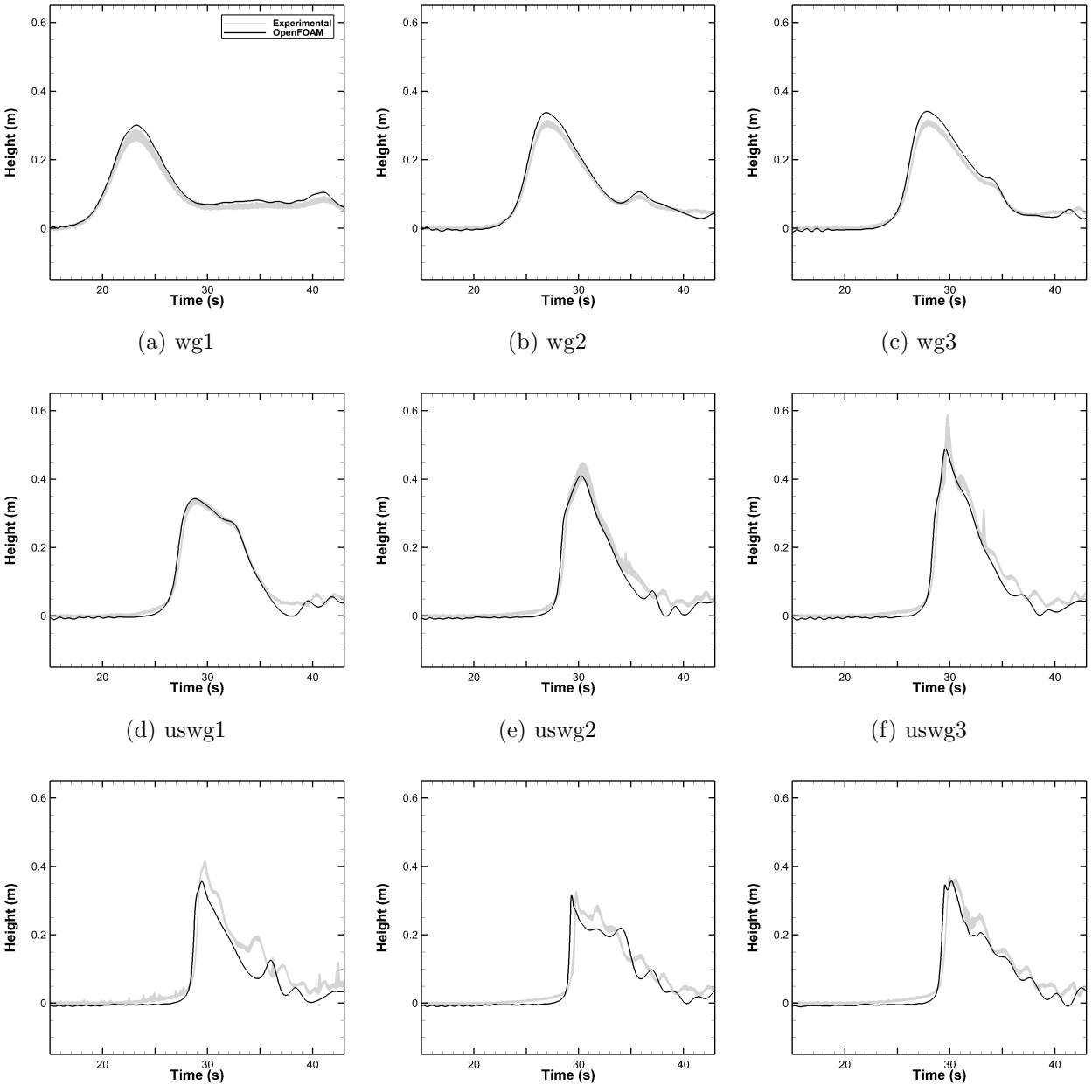

(a) wg1 (b) wg2 (c) wg3

(d) uswg1 (e) uswg2 (f) uswg3

(g) uswg4 (h) uswg5 (i) uswg6

Figure 6.5: Free Surface Elevation Numerical Agreement:Unbroken Wave

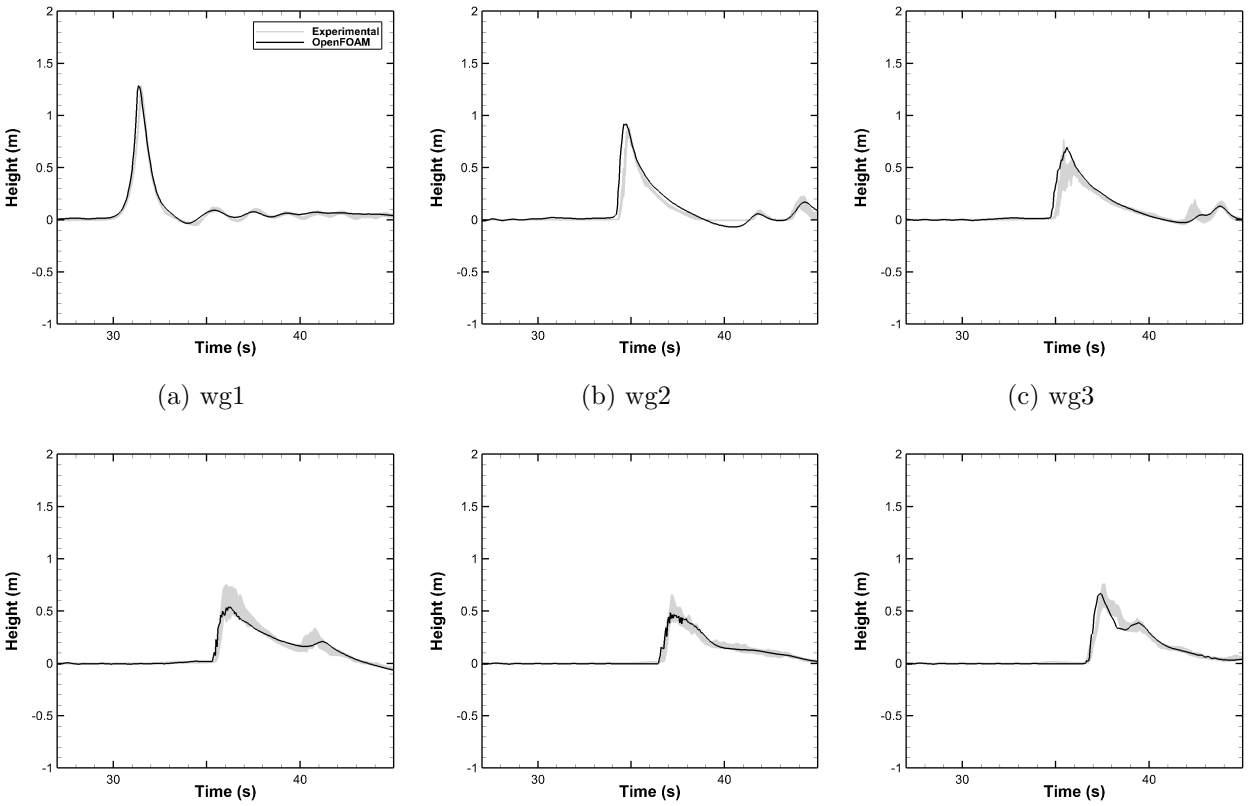

(a) wg1 (b) wg2 (c) wg3

(d) uswg1 (e) uswg5 (f) uswg6

Figure 6.6: Free Surface Elevation Numerical Agreement: Broken Wave

fraction and turbulence properties. Other requested output quantities are calculated through the time step outputs. For example, the free surface elevation is determined by the volume fraction interface, where α is typically equal to 0.5 and the force on a surface is determined through the pressure.

Numerical model validation is often achieved through force comparison. However structural properties and experimental set up can highly influence structural force distribution. Numerical validation by way of pressure measurement is an obvious and preferred solution to this problem.

To illustrate the credibility of model validation through pressure measurements, first the method of force calculation was shown to be valid for the experiment through the agreement of experimental pressure measurement and experimental forces. The proceeding section will show the agreement of numerical and experimental pressure and forces illustrating the capabilities of experimental models to be validated accurately through pressure measurement. In doing this it provide numerical models a robust method of model validation while increasing confidence in numerical results.

6.3.1 Pressure Time Histories

The front 17 pressure gauge comparisons are presented here. The pressure gauge locations are shown in Figures 2.9, 2.10, and 2.11. The pressure measurements for the other faces of the test structure are included in Appendix B.

The unbroken numerical prediction comparisons are shown in Figures 6.7 and 6.8. Although the numerical pressures overpredicted the experimental results for some of the gauge locations, generally the results show good agreement for all pressure measurements. There is agreement in pressure history shape and occurrence of maximum pressure. The non-zero initial pressure reading of gauge location FM1 was due to the proximity of the pressure reading to the still water. The initial water depth for the unbroken wave was at the bottom of the test structure. This is was also seen in the pressure measurements on the bottom face of the box in Appendix B.

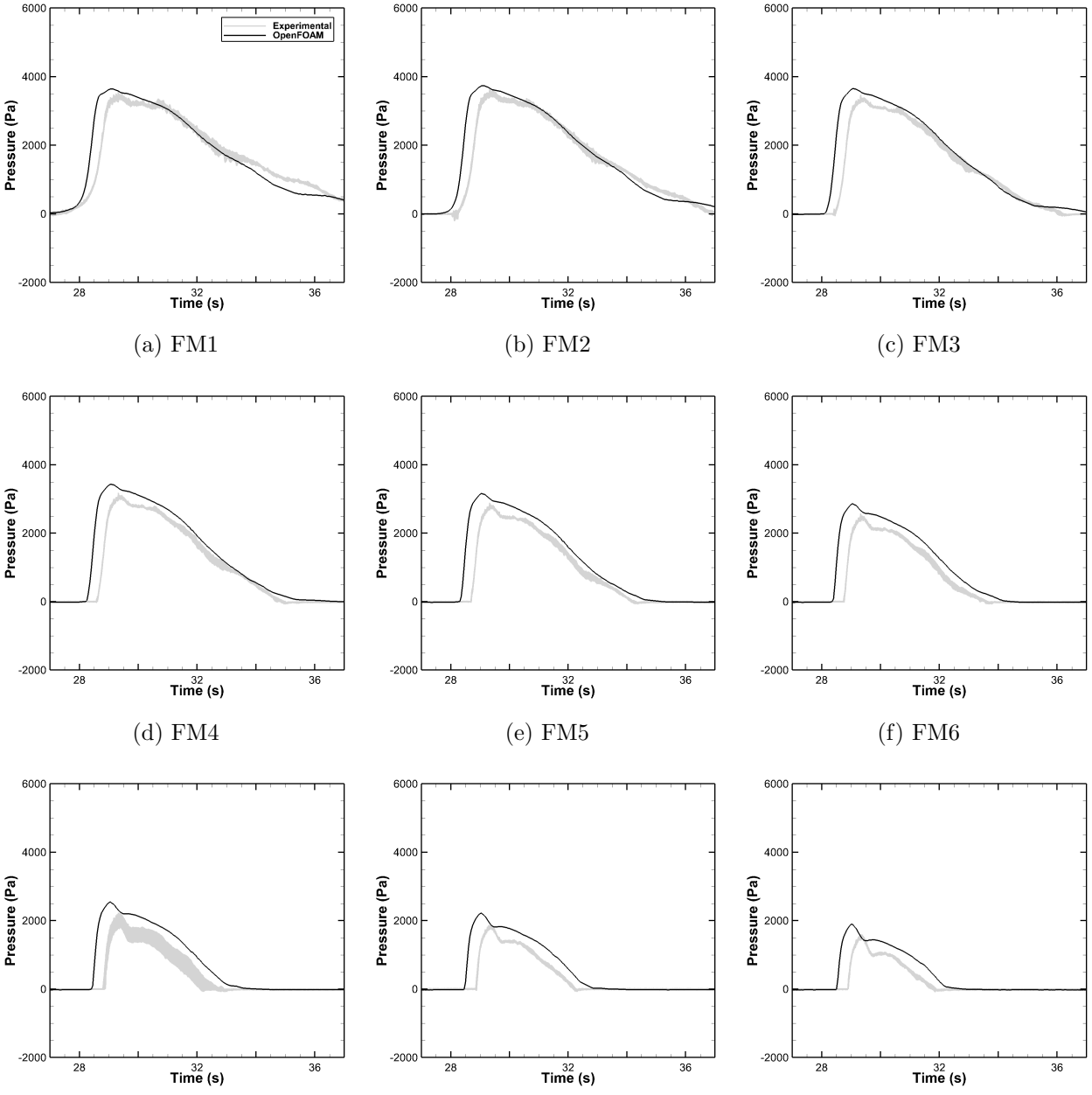

(a) FM1 (b) FM2 (c) FM3

(d) FM4 (e) FM5 (f) FM6

(g) FM7 (h) FM8 (i) FM9

Figure 6.7: Front Face Middle Pressure Time History Comparison: Unbroken Wave

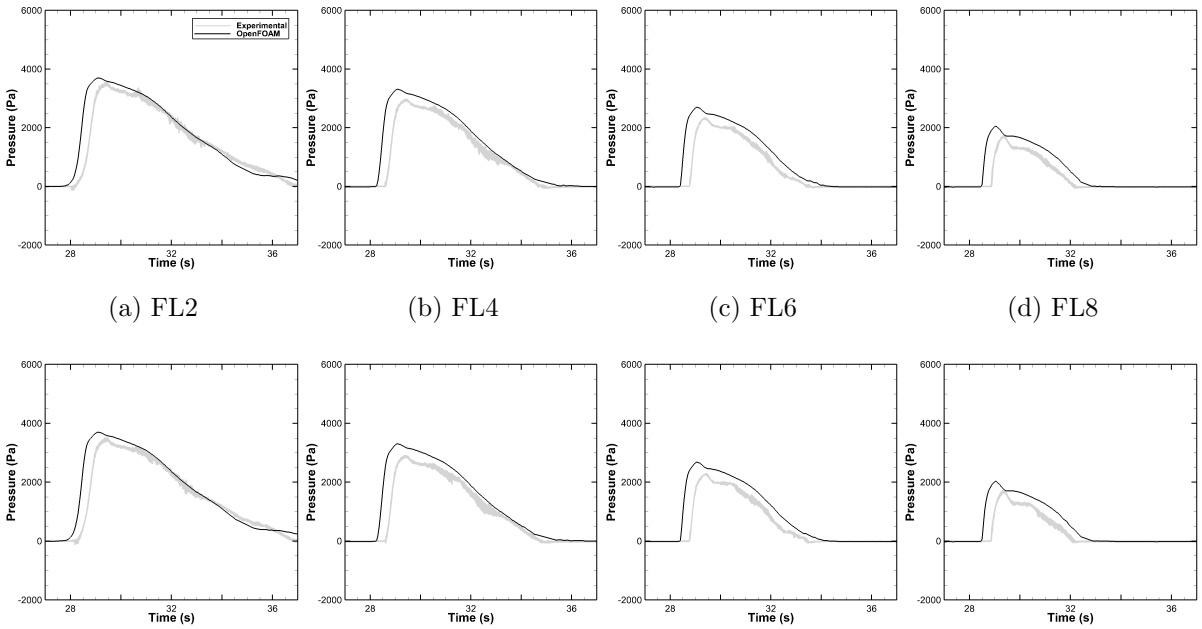

(a) FL2 (b) FL4 (c) FL6 (d) FL8

(e) FR2 (f) FR4 (g) FR6 (h) FR8

Figure 6.8: Front Face Side Pressure Time History Comparison: Unbroken Wave

The numerical prediction comparisons are shown in Figures 6.9 and 6.10 for the broken wave. The numerical predictions show good agreement for the arrival of the wave, duration of wave impact, the impulsive peak pressure, and the shape of the time history. The premature peaks seen in pressure time histories for FM1, FM2 and FM3 are most likely due to the proximity of these gauges locations to the still water. This peaks are from the wave approaching the structure. These peaks are also seen in gauges at similar elevations. The pressure gauge time histories illustrate the agreement between the numerical and experimental models and that the numerical model can produce similar results at the local level.

6.3.2 Force Measurements

The comparison of the stream-wise forces are shown in Figure 6.11. The stream-wise forces from the numerical models were compared with the back face threaded load cell (B). The numerical predictions show good agreement with the experimental results, even though the

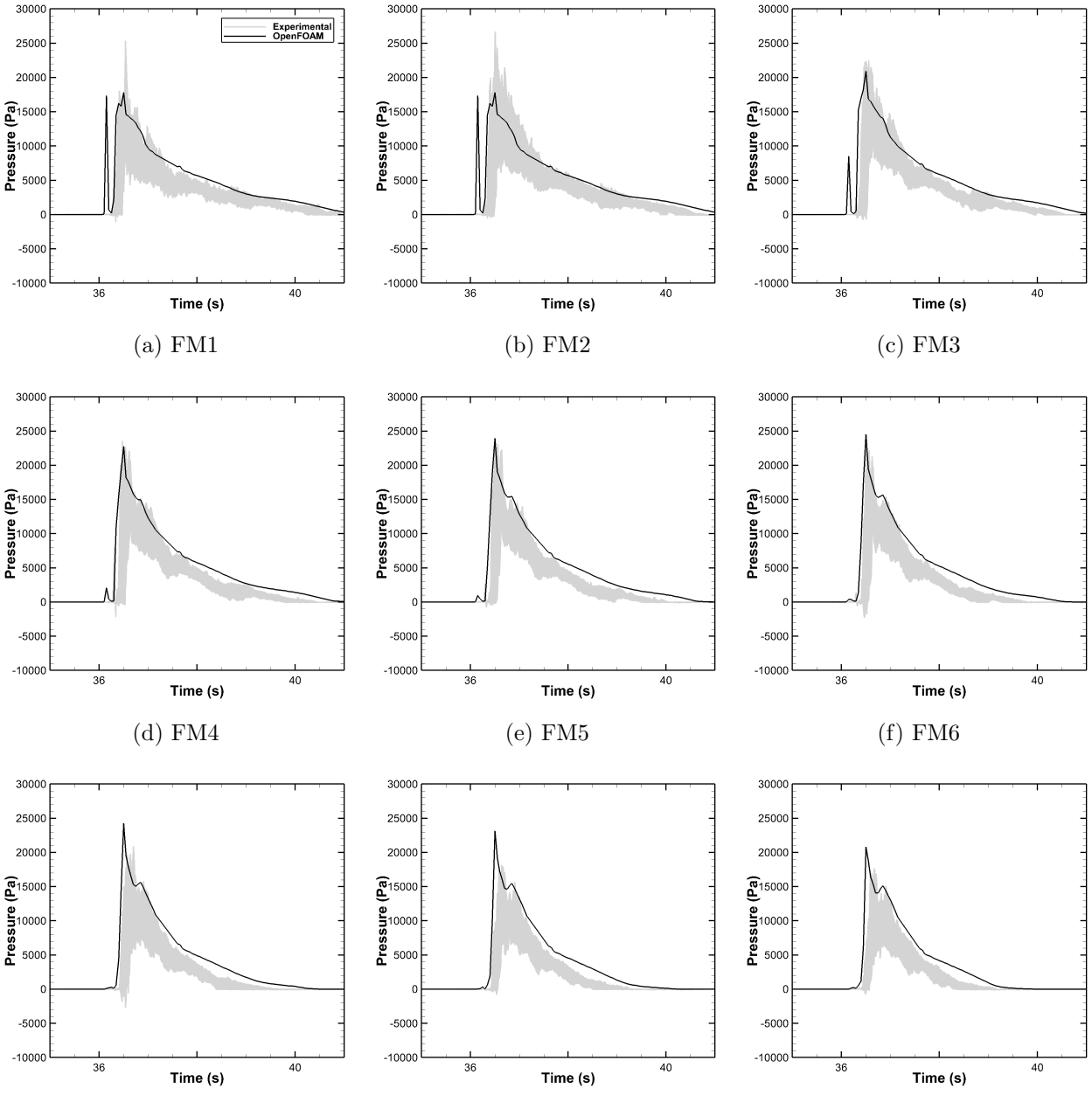

(a) FM1 (b) FM2 (c) FM3

(d) FM4 (e) FM5 (f) FM6

(g) FM7 (h) FM8 (i) FM9

Figure 6.9: Front Face Middle Pressure Time History Comparison: Broken Wave

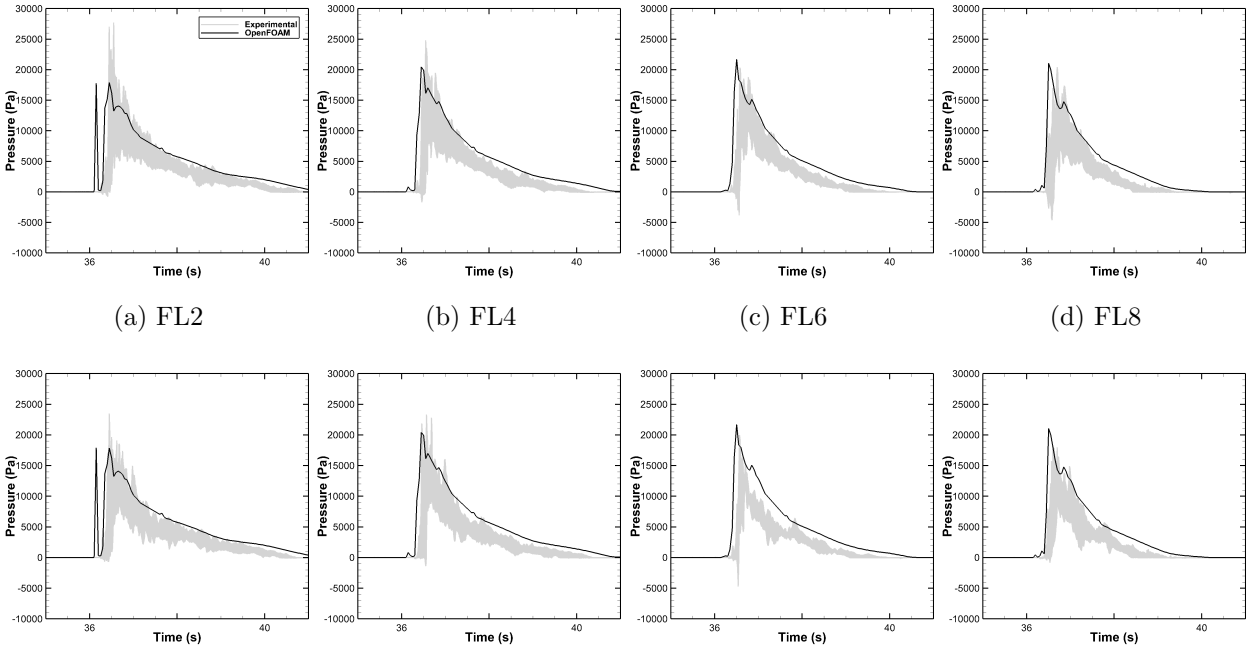

(a) FL2 (b) FL4 (c) FL6 (d) FL8

(e) FR2 (f) FR4 (g) FR6 (h) FR8

Figure 6.10: Front Face Side Pressure Time History Comparison: Broken Wave

numerical model overpredicts the forces. This over predictions could be due to the absence of the test structure as well as the assumption of a completely rigid structure. The unbroken wave force comparison shows an early arrival of the numerical wave. However this is also seen in the experimental pressure surface extrapolated forces (Figure **??**), as the front face of the test structure is the first impacted component.

As seen in these figures, the predicted numerical horizontal forces are in good agreement with the horizontal experimental forces. The numerical and extrapolated pressure distributions agree with the recorded reaction forces. Therefore force calculations by means of pressure extrapolation is valid for both the numerical and experimental data presented in this work.

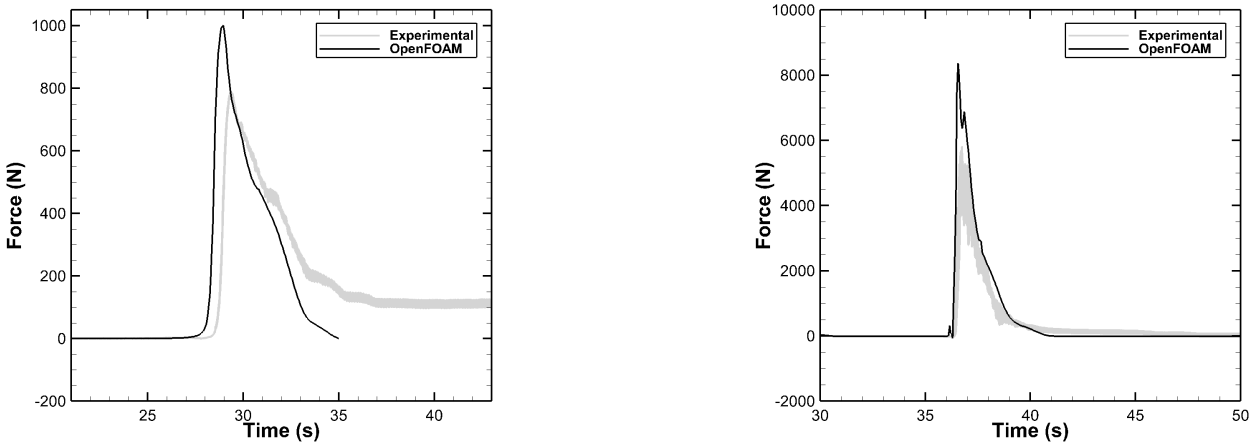

(a) Unbroken

(b) Broken

Figure 6.11: Stream-wise Force

6.4 Summary and Conclusion

A numerical validation was completed for the experimental test program conduced in the Large Wave Flume. The numerical prediction of wave height, pressures and forces were compared to experimental results. Through the use the the OpenFOAM solver *olaDyMFlow*, the wave was properly generated as shown through the wave height. The fluid properties were

adequately modeled through the use of the standard k-ϵ model. The numerical prediction of pressure and force measurement results showed good agreement with experimental values.

Numerical forces in the CFD model are calculated through pressure extrapolation. This work has shown that this method of force extraction is valid and comparable to experimental results through the agreement of experimental pressure surfaces and numerical pressure surfaces. The similarities of the experimental and numerical tests are further shown through the agreement in wave generation, as seen through the wave height time histories, and agreement in the wave structure interaction as seen through the pressure and force measurements.

Numerical models are highly dependent upon validation, and this is primarily done by force comparisons. As resultant forces are highly influenced by other experimental factors, numerical validation by way of pressure measurements can be a robust method of numerical model validation. Numerical pressure measurement validation has been shown in this work by first illustrating the method of force calculation in numerical models is valid in experimental tests. Then agreement of the numerical and experimental results in both pressure and forces illustrates the accuracy of numerical simulations. The importance of this finding should not be understated. There is a general reluctance at times to accept numerically predicted results as compared to experimentally predicted results. As computational power increases, modelers are better able to predict the physical response to a variety of problems. By extrapolating the results presented here to general problems, an increased confidence in numerical results can be expected.

Chapter 7

CONCLUSION

7.1 Summary

The recent tsunamis in the Pacific Ocean have caused enormous amounts of damage throughout affected regions. At risk coastal communities may not have accessible means of tsunami evacuation. Elevated structures are a practical solution for tsunami vertical evacuation refuge structures. Previous experimental work has focused on tsunami forces for on grade structures without consideration of a three-dimensional pressure field. Previous numerical model validation has been primarily achieved by comparing predicted forces; however, the manner in which these forces are predicted typically differs. In experiments, it is common to measure forces using individual load cells, while in many numerical models forces are predicted by integrating pressures across the faces of the structure. This work presents a comparison and validation of three-dimensional pressure distributions on an elevated structure with corresponding load time histories through both experimental and numerical results.

A large-scale experimental program was conducted at Oregon State University's O.H. Hinsdale Wave Research Laboratory. An elevated test structure was subjected to unbroken and broken tsunami-like waves generated by a piston type wavemaker. The experimental program implemented a three-dimensional pressure instrumentation layout not seen in similar experimental tests to date.

Throughout the experiment, the wave height and velocity were recorded as well as pressures and forces on the test structure. All measurements showed consistency and repeatable throughout the experiment. The similarities and differences were highlighted here. For example, when both waves were in the unbroken state, the results from wave height measurements had similar variations.

The test structure results illustrated the difference in the unbroken and broken wave conditions, particularly in the duration and distribution of the pressure and force measurements. The unbroken wave inundated the test structure for nearly twice the time as the broken wave. The pressures induced by the unbroken wave were comparable for similar elevations for all faces of the test structure. On the other hand, pressure measurements from the broken wave showed a concentration of pressure on the front face of the test structure. The pressure and force measurements of the broken wave illustrated the impulsive and turbulent nature of such a wave. The force measurements also illustrated the difference in the two waves as the unbroken wave caused large uplift forces on the test structure while the impulsive broken bore resulted in large stream-wise forces. Both waves showed minimal contribution of horizontal load from the attached columns.

Pressure measurements were gathered in the three-dimensional layout on the front face of the test structure. The consistency of experimental pressure measurement allowed the extrapolations of imposed pressure surfaces. Eight different fits were calculated for each wave case. Then each fit was integrated across the face of the test structure to obtain and resultant horizontal force for the front face. Through comparison of these forces with the experimental horizontal load cell and the resultant fits, it was clear that the unbroken wave pressure distribution was linear throughout inundation while the unbroken wave was best represented by a quadratic surface. The unbroken pressure surface resembled a hydrostatic pressure distribution for much of wave impact.

The three dimensional pressure surfaces were used to validate the experimental load cell. The resultant force showed excellent agreement. The extrapolated force maximum values were within 5% of the mean maximum experimental value for both wave conditions. The force-pressure surface comparison was conducted to illustrate that force calculation by means of pressure surfaces is valid for experimental results. There is some reluctance to accept numerical results as they are calculated in this manner. Through showing experimentally that this method of force prediction is achievable it should therefore increase the confidence in numerical results.

To further increase confidence in numerical results, a corresponding numerical analysis was performed for the experimental tests. A numerical domain modeled after the experimental test was simulated through the use of the computational fluid dynamics software package OpenFOAM. In order to simulate a piston wave maker, as used in the experiment, the three-dimensional dynamic mesh multiphase OpenFOAM solver *olaDyMFlow* was implemented. A solution was reached through geometry discretization, the Reynolds Averaged Naiver Stokes equations and the Volume of Fluid Method. Incompressible turbulent flow was assumed. The standard k-ϵ closure model was used for turbulence modeling. The numerical predictions for the wave height, load cell and pressure gauges showed good agreement with the experimental data. The over prediction of numerical forces could be due to the absence of the experimental support structure or the rigid body assumption. However, numerical pressures and forces have similar shapes and duration.

The experimental pressure surface extrapolation was in agreement with the experimental load cell. This shows that force calculation by way for pressure surfaces is valid in experimentation. The numerical model was validated through the resultant pressure gauges and stream-wise force time histories. The agreement of experimental and numerical pressures and forces proves that the numerical forces, although extrapolated from pressures calculated by the RANS equations, are similar to the measured forces measured by experimental methods.

In summary, computational fluid dynamics modeling is highly dependent upon validation by mean of experimental results. This is done by force comparison due to the state of the current experimental results. It has been proven in this work that the method by which numerical models calculate their results is valid in an experimental setting, and that model validation is achievable through pressure measurements. This work hopes to encourage the collaboration of future experimental and numerical work so that experimental instrumentation considers ease of numerical model validation.

7.2 Future Work

This thesis presents trends in the three-dimensional pressure distribution on elevated structures as well as observations concerning the unbroken and broken waves and numerical and experimental validation of pressure distributions. However, future numerical and experimental research will improve the understanding of the three-dimensional pressure distributions and accurate numerical simulations of tsunami waves.

Concerning the pressure distributions, parametric studies varying the angle at which the tsunami wave impacts the structure could be beneficial. Additionally, variation of still water depth will improve the understanding of the dependence of the trends in pressure distribution to the flow parameters. As seen through previous experimental work, a variety of pressure distributions were observed for tsunami waves ([7] [27] [14] [24]). This work presented pressure distribution trends concerning two consistently generated tsunami waves. Variation of the structural angle and of the water height will aid in understanding of whether other observed pressure distributions are valid for elevated structures.

As the current research has not focused on elevated structures, there are many experimental configurations that would improve the understanding of the tsunami induced forces and pressures. Experimental and accompanying numerical parametric studies concerning the modification to tsunami forces and pressures will benefit structural tsunami force estimation. For example, during the experimental test program discussed here, the effects of macro-scale roughness to the same wave conditions on an elevated structure were investigated.

Highly instrumented experimental procedures are expensive and can be unfeasible. With the advancement in computational power in the recent decades, numerical modeling of complex phenomenon, such as tsunamis, is becoming more and more practical. The validation of the experimental and numerical resultant forces presented in this work further illustrates the similarities between the experimental and numerical resultant forces. Therefore future work consisting of complex parametric studies are feasible and recommended.

BIBLIOGRAPHY

[1] Federal Emergency Management Agency. The national flood insurance program: Definitions. `https://www.fema.gov/national-flood-insurance-program/definitions`. [Online; accessed Feburary-2017].

[2] Mohamman Shafiqual Alam. Personal Communication.

[3] Francesco Aristodemo, Giuseppe Tripepi, Domenico Davide Meringolo, and Paolo Veltri. Solitary wave-induced forces on horizontal circular cylinders: Laboratory experiments and sph simulations. *Coastal Engineering*, 129:17 – 35, 2017.

[4] ASCE. *7-16 Minimum Design Loads and Associated Criteria for Building and Other Structures*, 2017.

[5] Pablo Higuera Caubilla. *Applicaiton of Computational Fluid Dynamics to Wave Action on Structures*. PhD thesis, University of Cantabria, January 2015.

[6] Pablo Higuera Caubilla. olaflow. `https://github.com/phicau/olaFlow`, 2017.

[7] Chaiyuth Chinnarasri, Nuttawut Thanasisathit, Anat Ruangrassamee, Sutat Weesakul, and Panitan Lukkunaprasit. The impact of tsunami-induced bores on buildings. *Proceedings of the Institution of Civil Engineers - Maritime Engineering*, 166(1):14–24, 2013.

[8] Marie E. Cowart and William J. Serrow. Population aging in urban centers of the pacific rim: Implications for planners. *Berkeley Planning Journal*, 1998.

[9] Santiago Mrquez Damin. Description and utilization of interfoam multiphase solver. `http://infofich.unl.edu.ar/upload/3be0e16065026527477b4b948c4caa7523c8ea52.pdf/`, 2016. [Online; accessed Feburary-2017].

[10] Federal Emergency Management Agency. *Guidelines for Design of Structures for Vertical Evacuation from Tsunamis*, fema p-646 edition, April 2012.

[11] The OpenFOAM Foundation. The OpenFOAM user guide. `https://openfoam.org/`, 2017. [Online; accessed Feburary-2017].

[12] Ahmed Ghobarah, Murat Saatcioglu, and Ioan Nistor. The impact of the 26 december 2004 earthquake and tsunami on structures and infrastructure. *Engineering Structures*, 28:312–326, 01 2006.

[13] Leslie C Gordon. Preparing for tsunami hazards on washingtons pacific coast. `https://www.usgs.gov/news/preparing-tsunami-hazards-washington-s-pacific-coast`, 2017.

[14] M. A. Hamzah, Hajime Mase, and Tomotsuka Takayama. Simulation and experiment of hydrodynamic pressure on a tsunami barrier. *Coastal Engineering*, 2000.

[15] Shih-Chun Hsiao and Ting-Chieh Lin. Tsunami-like solitary waves impinging and overtopping an impermeable seawall: Experiment and rans modeling. *Coastal Engineering*, 57(1):1 – 18, 2010.

[16] Changbo Jiang, Xiaojian Liu, Yu Yao, Bin Deng, and Jie Chen. Numerical investigation of tsunami-like solitary wave interaction with a seawall. *Journal of Earthquake and Tsunami*, 11(01):1740006, 2017.

[17] W.P Jones and B.E Launder. The prediction of laminarization with a two-equation model of turbulence. *International Journal of Heat and Mass Transfer*, 15(2):301 – 314, 1972.

[18] Naoto Kihara, Yasuo Niida, Daisuke Takabatake, Hideki Kaida, Atsushi Shibayama, and Yoshinori Miyagawa. Large-scale experiments on tsunami-induced pressure on a vertical tide wall. *Coastal Engineering*, 99:46 – 63, 2015.

[19] Michael R. Motley, Hin Kei Wong, Xinsheng Qin, Andrew O. Winter, and Marc O. Eberhard. Tsunami-induced forces on skewed bridges. *Journal of Waterway, Port, Coastal, and Ocean Engineering*, 142(3), 2016.

[20] Pacific Northwest Seismic Network. Cascadia subduction zone. `https://pnsn.org/outreach/earthquakesources/csz/`. [Online; accessed Feburary-2017].

[21] Cuong Nguyen. Turbulence modeling. `http://www.mit.edu/~cuongng/Site/Publication_files/TurbulenceModeling_04NOV05.pdf`, November 2005. [Online; accessed Feburary-2017].

[22] Younes Nouri, Ioan Nistor, Dan Palermo, and Andrew Cornett. Experimental investigation of tsunami impact on free standing structures. *Coastal Engineering Journal*, 52(1):43–70, 2010.

[23] CFD Online. Turbulence length scale. `https://www.cfd-online.com/Wiki/Turbulence_length_scale`. [Online; accessed Feburary-2017].

[24] Dan Palermo, Ioan Nistor, Taofiq Al-Faesly, and Andrew Cornett. Impact of tsunami forces on structures: The university of ottawa experience, 2012.

[25] Xinsheng Qin, Michael R. Motley, Randall J. LeVequeb, Frank I. Gonzalezc, and Kaspar Mueller. A comparison of a two-dimensional depth averaged flow model and a three-dimensional rans model for predicting tsunami inundation and fluid forces. Manuscript submitted for publication, 2018.

[26] Xinsheng Qin, Michael R. Motley, and Nasser Marafi. Three-dimensional modeling of tsunami forces on coastal communities. Manuscript submitted for publication, 2017.

[27] Robertson IN, Paczkowski KK, Riggs HR, Mohamed AA. Tsunami Bore Forces on Walls. Tsunami bore forces on walls. In *Offshore Technology; Polar and Arctic Sciences and Technology*. ASME.

[28] Samieh Sarjamee, Ioan Nistor, and Abdolmajid Mohammadian. Numerical investigation of the influence of extreme hydrodynamic forces on the geometry of structures using openfoam. *Natural Hazards*, 87(1), 2017.

[29] Betsy Seiffert, Masoud Hayatdavoodi, and R. Cengiz Ertekin. Experiments and computations of solitary-wave forces on a coastal-bridge deck. part i: Flat plate. *Coastal Engineering*, 88:194 – 209, 2014.

[30] Seyedreza Shafiei, Bruce W. Melville, and Asaad Y. Shamseldin. Experimental investigation of tsunami bore impact force and pressure on a square prism. *Coastal Engineering*, 110:1 – 16, 2016.

[31] Anawat Suppasri, Nobuo Shuto, Fumihiko Imamura, Shunichi Koshimura, Erick Mas, and Ahmet Cevdet Yalciner. Lessons learned from the 2011 great east japan tsunami: Performance of tsunami countermeasures, coastal buildings, and tsunami evacuation in japan. *Pure and Applied Geophysics*, 170(6):993–1018, Jun 2013.

[32] United States Geological Survey. Cascadia subduction zone. `https://earthquake.usgs.gov/data/crust/cascadia.php`. [Online; accessed Feburary-2017].

[33] United States Geological Survey. Tsunami-ready office buildings. `https://www.usgs.gov/media/images/tsunami-ready-office-buildings`. [Online; accessed Feburary-2017].

[34] Tori Tomiczek, Amy Wyman, Hyoungsu Park, and Daniel T. Cox. Application and modification of godas formulae to estimate horizontal and vertical forces on elevated coastal structures. part 1: Nonbreaking waves. Manuscript submitted for publication, 2017.

[35] Andrew O. Winter. Personal Communication.

[36] Andrew O. Winter, Michael R. Motley, and Marc O. Eberhard. Tsunami-like wave loading of individual bridge components. *Journal of Bridge Engineering*, 23(2), 2018.

Appendix A

EXPERIMENTAL RESULTS

A.1 Wave Gauges

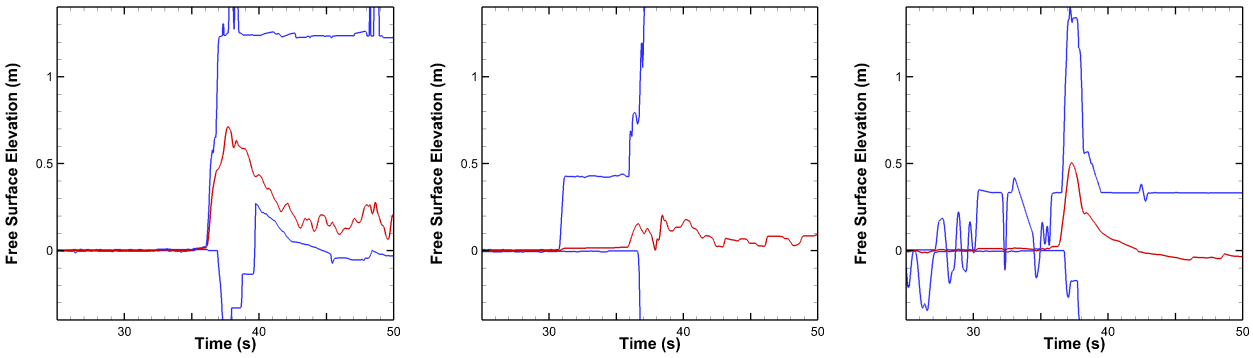

(a) uswg2 (b) uswg3 (c) uswg4

Figure A.1: Wave Height Comparisons: Broken Wave

A.2 Acoustic Doppler Velocimeters

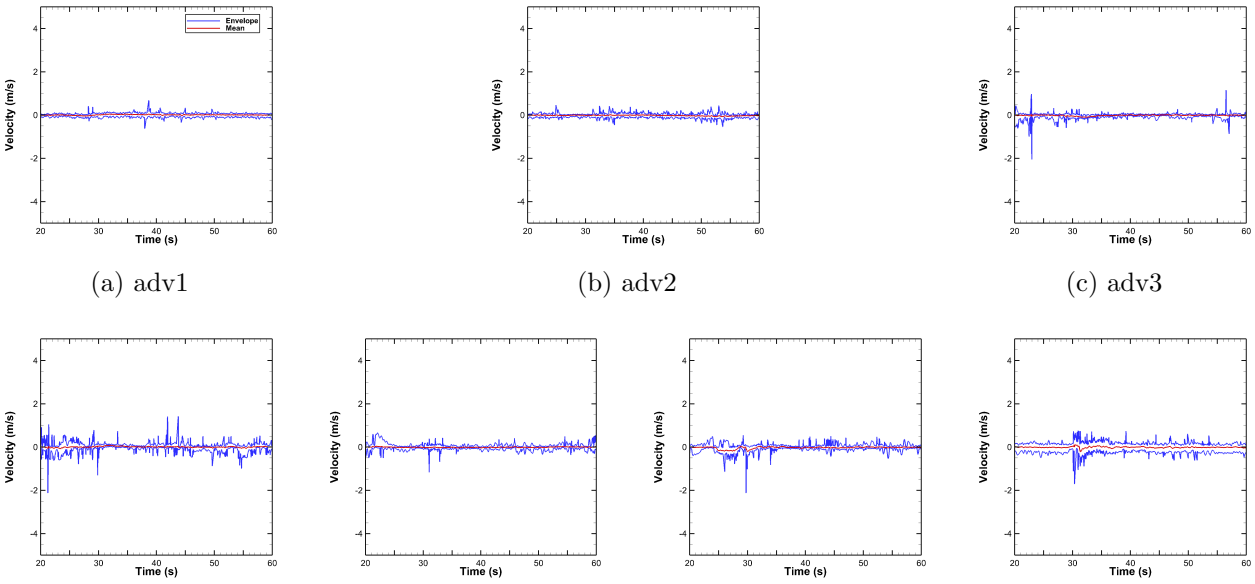

(a) adv1 (b) adv2 (c) adv3

(d) adv4 (e) adv5 (f) adv6 (g) adv7

Figure A.2: Transverse Direction Velocity: Unbroken Wave

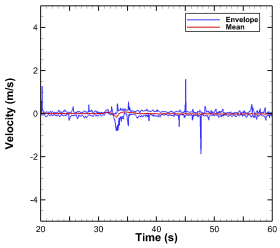

(a) adv1

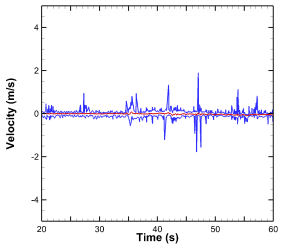

(b) adv2

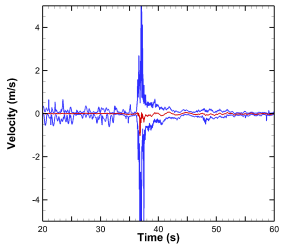

(c) adv3

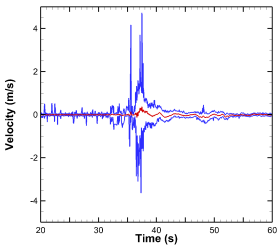

(d) adv4

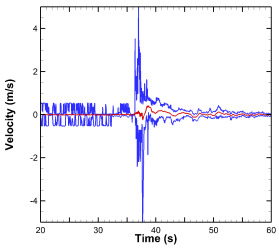

(e) adv5

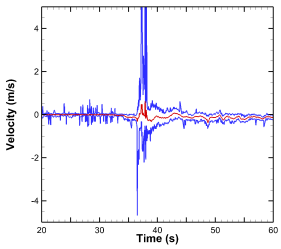

(f) adv6

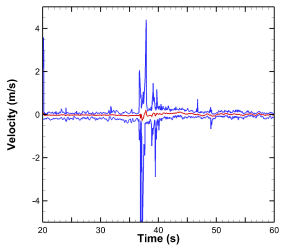

(g) adv7

Figure A.3: Transverse Direction Velocity: Broken Wave

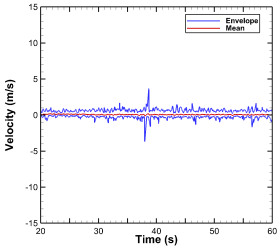

(a) adv1

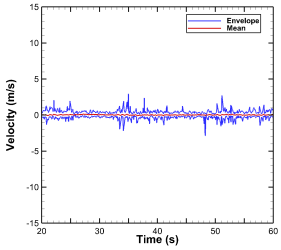

(b) adv2

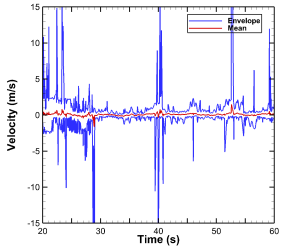

(c) adv3

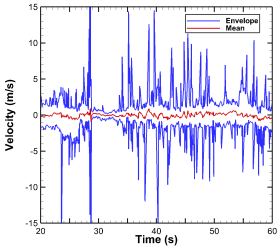

(d) adv4

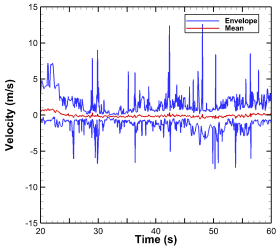

(e) adv5

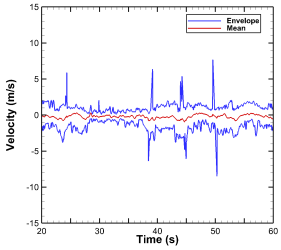

(f) adv6

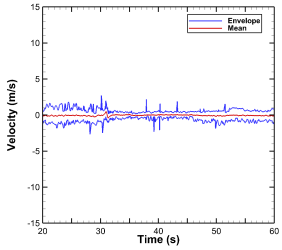

(g) adv7

Figure A.4: Vertical Direction Velocity: Unbroken Wave

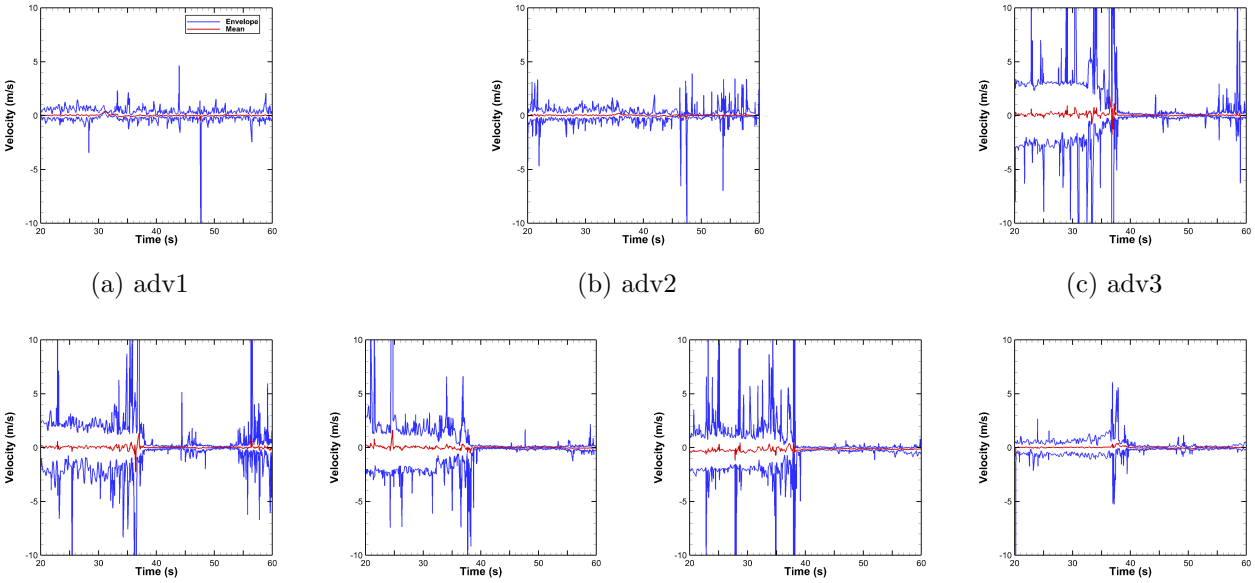

(a) adv1 (b) adv2 (c) adv3

(d) adv4 (e) adv5 (f) adv6 (g) adv7

Figure A.5: Vertical Direction Velocity: Broken Wave

Appendix B

NUMERICAL RESULTS

B.1 Wave Gauges

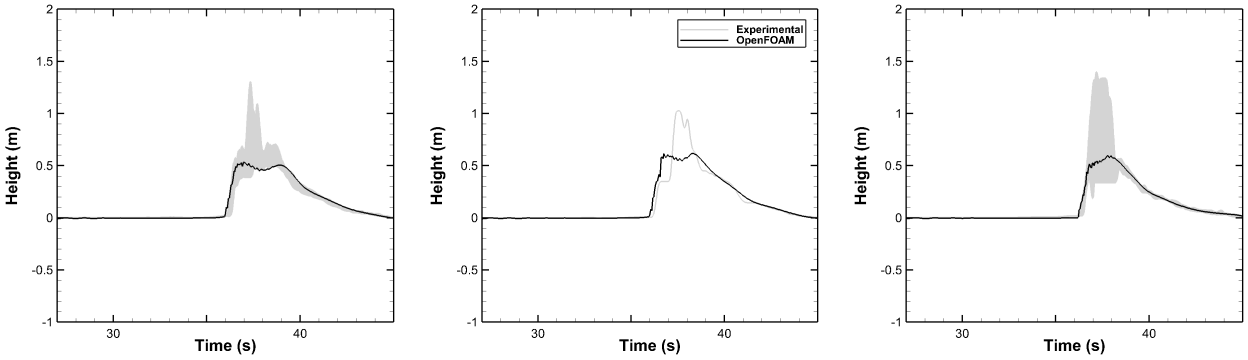

(a) uswg2 (b) uswg3 (c) uswg4

Figure B.1: Wave Height Comparisons: Broken Wave

B.2 Pressure Gauges

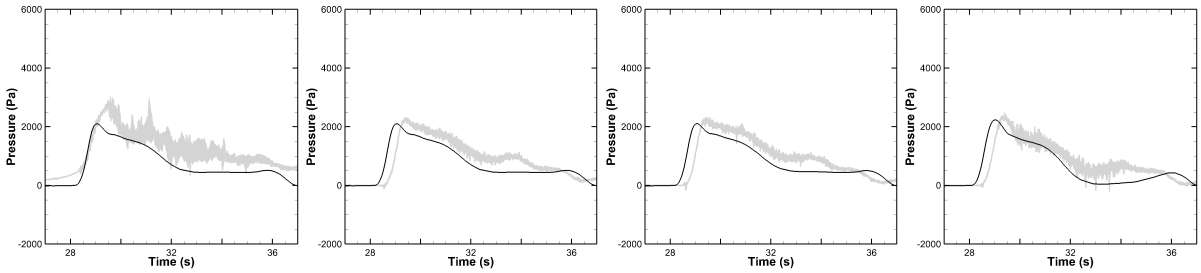

(a) LR (b) LL (c) RR (d) RL

Figure B.2: Side Pressure History Comparison: Unbroken Wave

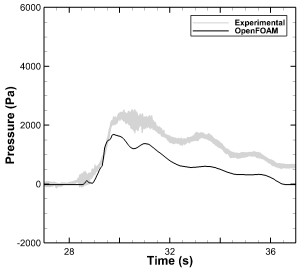

(a) B

Figure B.3: Back Pressure History Comparison: Unbroken Wave

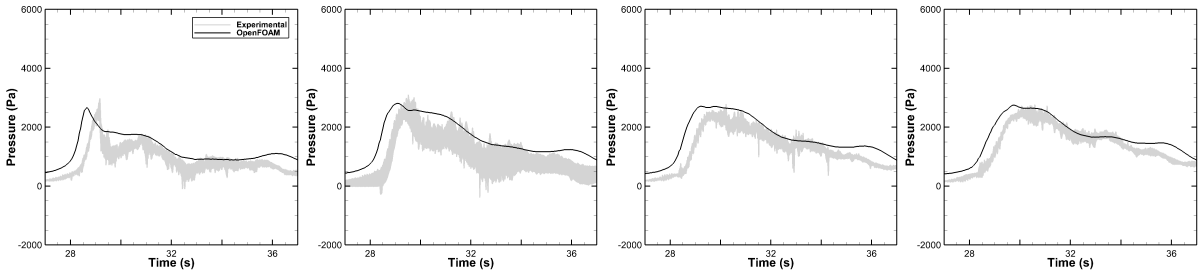

(a) XM1 (b) XM2 (c) XM3 (d) XM4

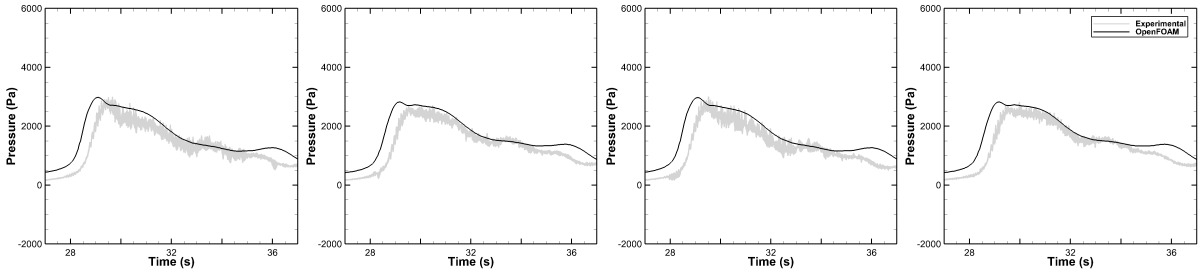

(e) XR2 (f) XR3 (g) XL2 (h) XL3

Figure B.4: Bottom Face Pressure History Comparison:Unbroken Wave

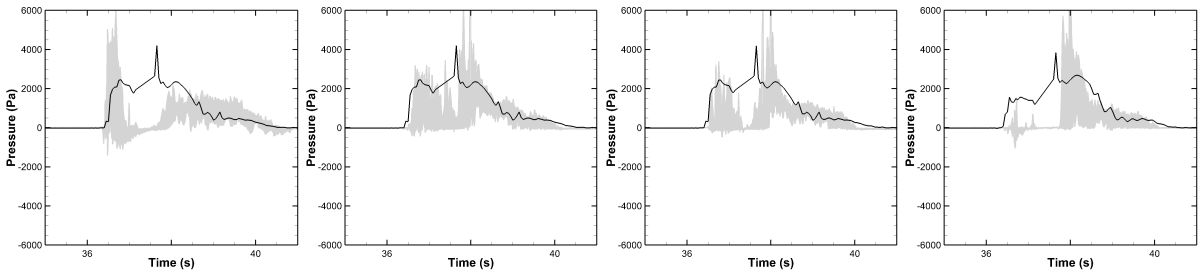

(a) LR (b) LL (c) RR (d) RL

Figure B.5: Side Pressure Gauges Comparison: Broken Wave

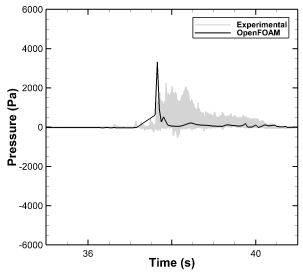

(a) B

Figure B.6: Back Pressure History Comparison: Broken Wave

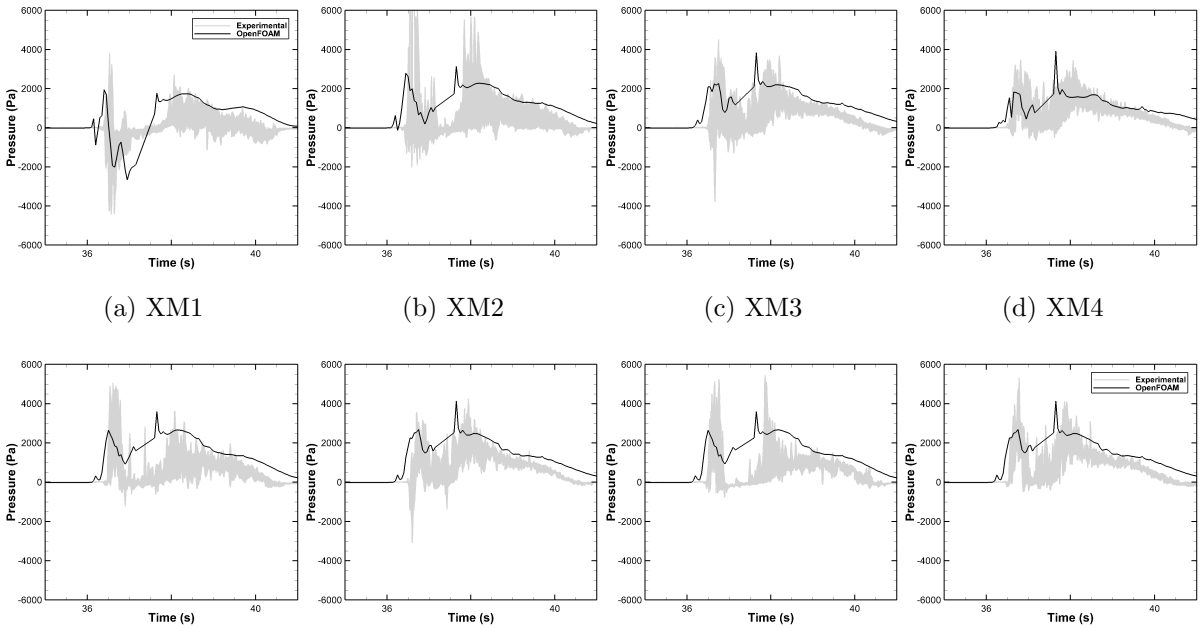

(a) XM1 (b) XM2 (c) XM3 (d) XM4

(e) XR2 (f) XR3 (g) XL2 (h) XL3

Figure B.7: Bottom Face Pressure Time History Comparison:Broken Wave

B.3 Velocity Measurements

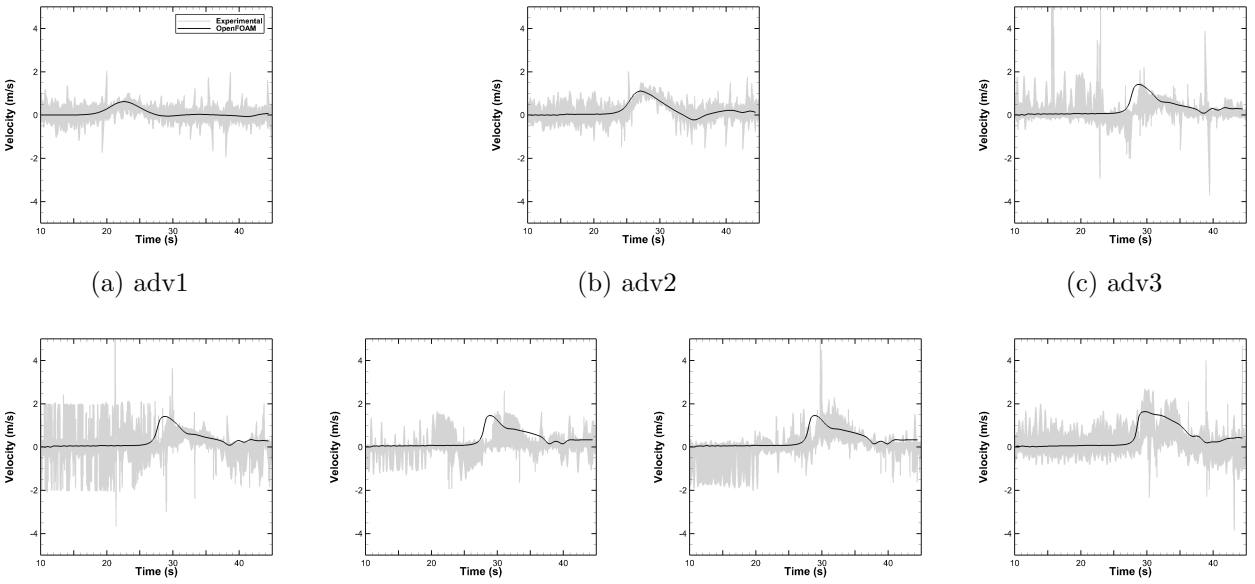

(a) adv1 (b) adv2 (c) adv3

(d) adv4 (e) adv5 (f) adv6 (g) adv7

Figure B.8: Stream-wise Velocity Comparison: Unbroken Wave

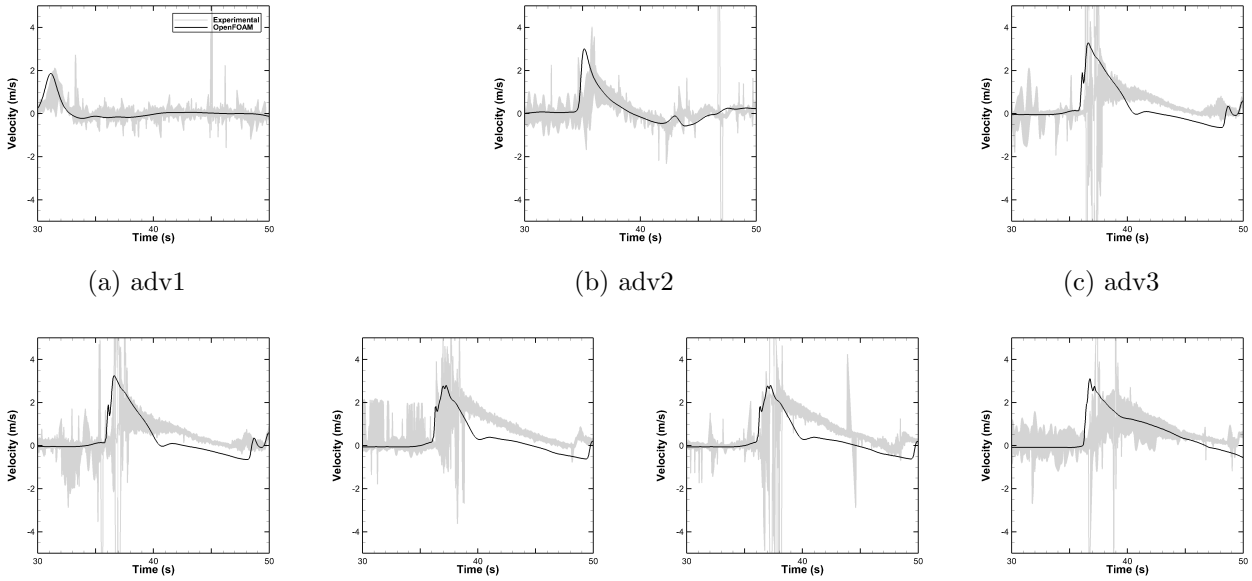

(a) adv1 (b) adv2 (c) adv3

(d) adv4 (e) adv5 (f) adv6 (g) adv7

Figure B.9: Stream-wise Velocity Comparison: Broken Wave

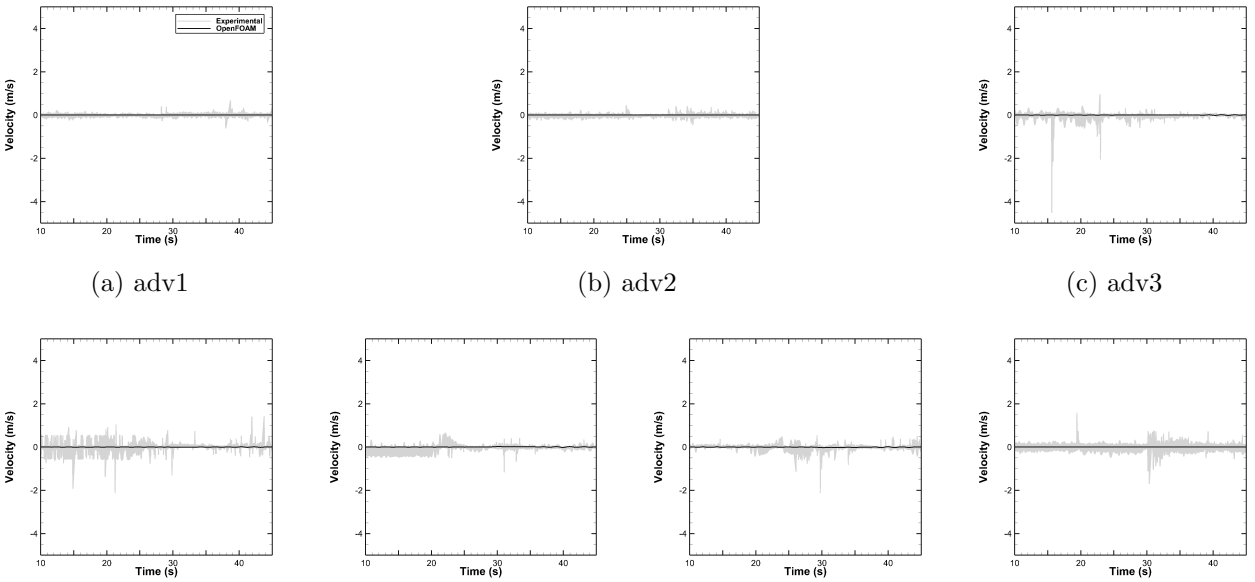

(a) adv1 (b) adv2 (c) adv3

(d) adv4 (e) adv5 (f) adv6 (g) adv7

Figure B.10: Transverse Velocity Comparison: Unbroken Wave

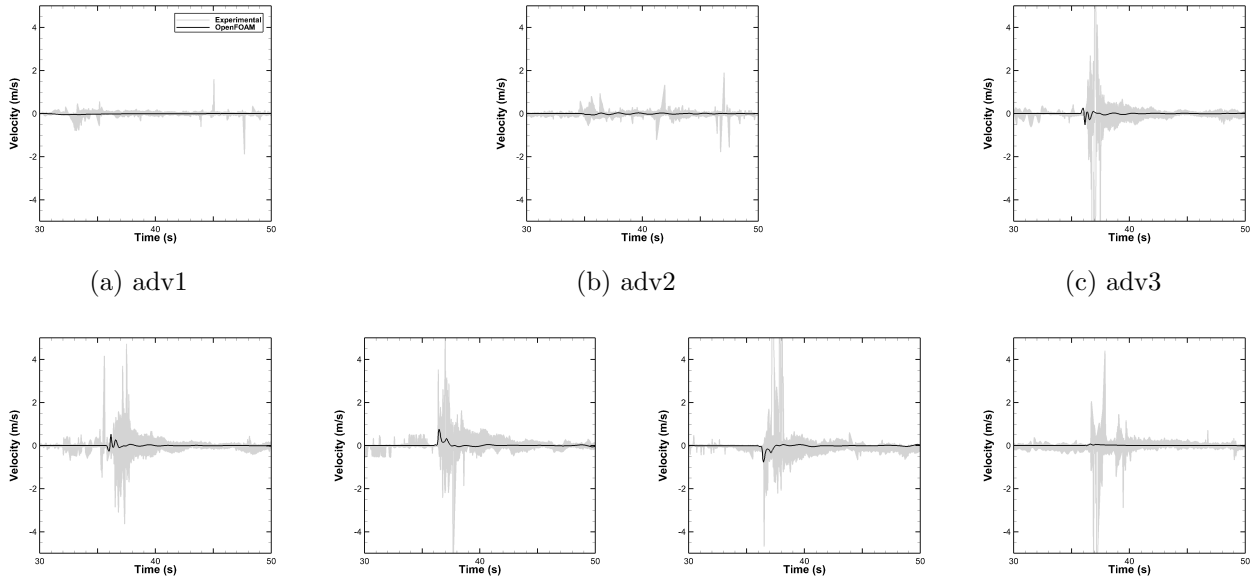

(a) adv1 (b) adv2 (c) adv3

(d) adv4 (e) adv5 (f) adv6 (g) adv7

Figure B.11: Transverse Velocity Comparison: Broken Wave

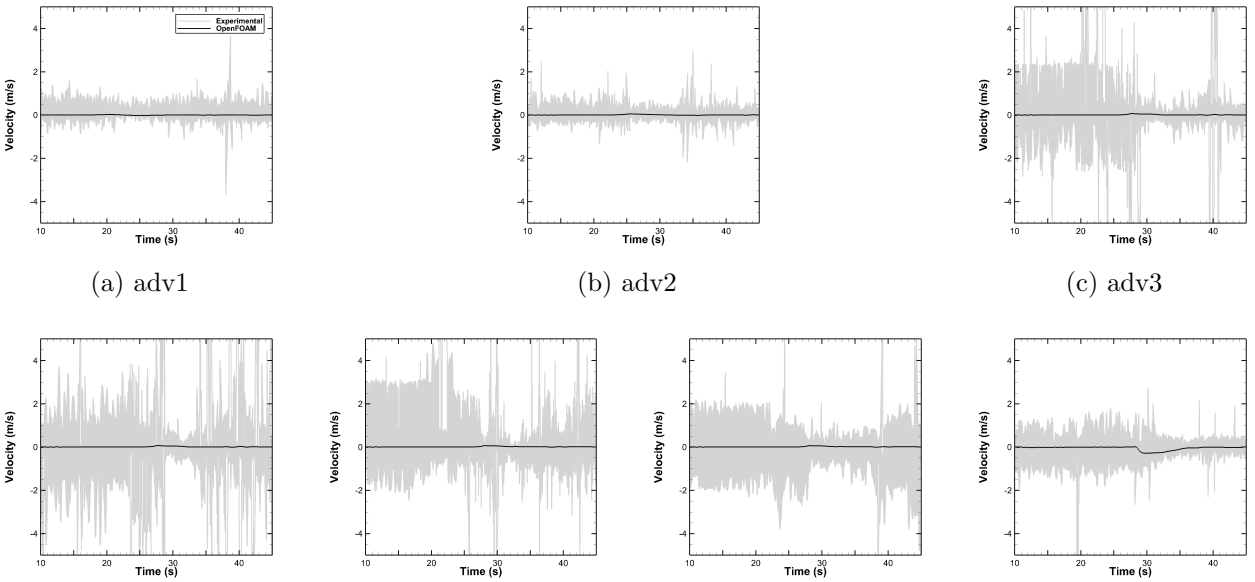

(a) adv1 (b) adv2 (c) adv3

(d) adv4 (e) adv5 (f) adv6 (g) adv7

Figure B.12: Vertical Velocity Comparison: Unbroken Wave

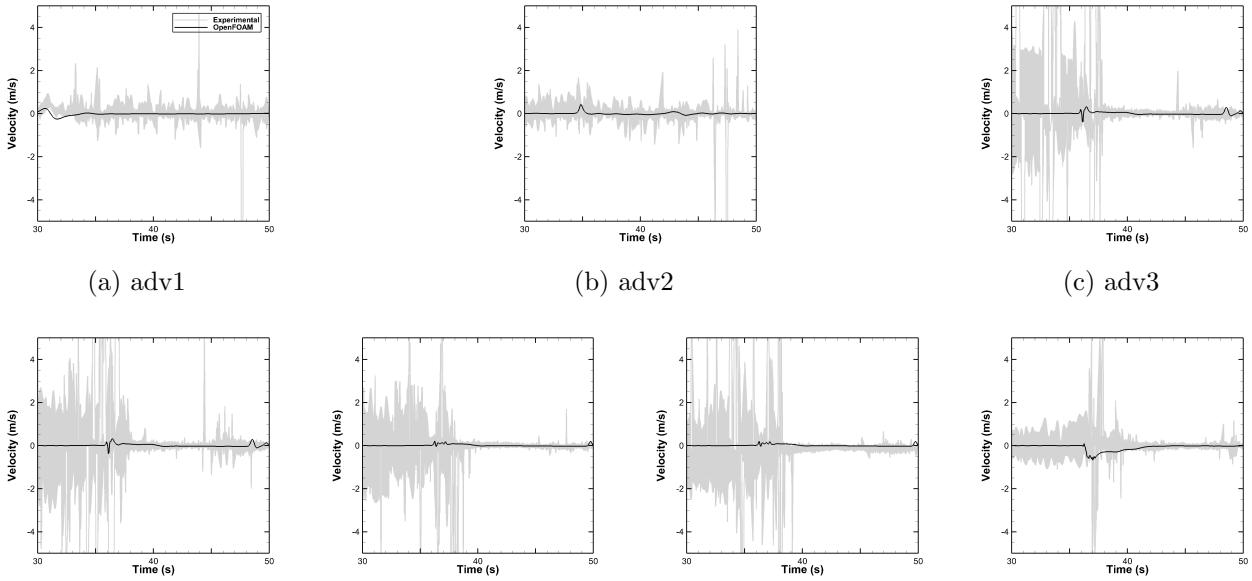

(a) adv1 (b) adv2 (c) adv3

(d) adv4 (e) adv5 (f) adv6 (g) adv7

Figure B.13: Vertical Velocity Comparison: Broken Wave